Views of an Ocean World: The Signatures of Internal and External Processes on the Surface of Europa

Thesis by
Samantha K. Trumbo

In Partial Fulfillment of the Requirements for the
Degree of
Doctor of Philosophy in Planetary Science

CALIFORNIA INSTITUTE OF TECHNOLOGY
Pasadena, California

2021
Defended November 16, 2020

Samantha K. Trumbo
ORCID: 0000-0002-0767-8901

In loving memory of Skipper, who was there for me from my first telescope at age ten through my first year at Caltech. You are forever my best friend.

ACKNOWLEDGEMENTS

I would first like to thank my parents, Bruce and Sheryl Trumbo, for their endless love and support and for all of their hard work and dedication in prioritizing my education. From my digging up "fossils" in the backyard to my suddenly announcing the totally practical choice to major in astronomy, they have always supported and encouraged my love of science. To this day, some of the toughest questions I get about my work come from Dad, who has always taught me to question why things work the way they do. I would also like to thank my grandparents, Donald and Barbara Trumbo, who contributed so much to my education and who helped make my eventual path to Caltech possible. I often attribute my fascination with space to a 4th-grade trip to AstroCamp, but part of that blame falls on Grandpa, whose own interest in astronomy and whose campfire stories of working at Kitt Peak rubbed off on me as a child. Thank you to James, my little brother, who has stuck by me through everything and always lent a thoughtful ear during tough decisions or times of stress. Thank you to the rest of my family as well, for always being there and always caring, and in particular to my Aunt Jan and Uncle Joel for their wisdom and advice, for feeding my caffeine addiction, and for facilitating remarkable travels that provided much needed breaks throughout this journey.

Thank you to my advisor, Mike Brown, whose support and guidance have truly shaped me as a scientist. I have learned so much from him—from observing, to proposal writing, to scientific speaking. For all of these things I am enormously grateful, but I especially want to thank him for his encouragement of independent and critical thinking, which has continually pushed me to grow. Thank you to my collaborators, Kevin Hand, Bryan Butler, and Katherine de Kleer, for their research and professional guidance. I would also like to thank the other members of my committee, Bethany Ehlmann, Dave Stevenson, and Geoff Blake for their insightful advice on this thesis and on my future, as well Andy Ingersoll and Tricia Ewald for their research advising during my first-year proposition. Tricia's computer knowledge has also spared me much frustration, and our conversations and catch-ups always brightened my day. Thank you as well to all who have passed through Mike's group, including Elizabeth Bailey, Ian Wong, Patrick Fischer, Katherine de Kleer, and James Keane, who have each provided stimulating discussions and sage advice. Thanks to my amazing officemates for making graduate school fun and again to Elizabeth Bailey for our countless Peet's walks.

I would also like to extend a special thanks to everyone in the Planetary Science office—Ruth Loisel, Margaret Carlos, Irma Black, Loreta Young, and Ulrika Terrones—who provide invaluable support to the entire department.

Finally, I would like to thank my partner, Eric Sawyer, for his unwavering support and encouragement, our two cats, Sulu and Mochi, for their endlessly uplifting antics, and the rest of the family felines—Isis, Copernicus, Daisy, Misty, and Skipper—for always knowing what to say.

ABSTRACT

Beneath a comparatively thin ice shell, Europa harbors a global, salty, liquid-water ocean in contact with a rocky seafloor, making it an exciting target for exploring habitability in the Solar System. The potential habitability of Europa's ocean depends on its composition, which may be reflected in that of Europa's geologically young, fractured surface. However, two intertwined uncertainties are the degree to which the ocean and the surface are in contact, and the degree to which surface materials truly represent oceanic signatures. The latter is complicated by the fact that Europa's surface is continuously altered by sulfur plasma and particle irradiation due to its location within Jupiter's magnetosphere. In this thesis, I utilize a variety of multi-spectral, Earth-based observations of Europa to explore the balance and interplay of internal and external processes in shaping its surface.

Chapters II and III focus on using visible-wavelength spectroscopy from the Hubble Space Telescope (HST) to understand the chemistry of Europa's surface salts. In Chapter II, I present the detection of irradiated sodium chloride (NaCl) and show that its distribution correlates with geologically disrupted chaos terrain, suggesting an ocean source. In Chapter III, I investigate multiple spectral features across Europa's sulfur-bombarded trailing hemisphere. In comparing their geographies with the distributions of large-scale geology, magnetospheric particle bombardment, and surface color, I identify some features as reflective of purely exogenous sulfur radiolysis products and others as indicative of radiolysis products formed from a mixture of endogenous material and magnetospheric sulfur.

Chapters IV and V further consider the effects of radiolytic processing through the analysis of infrared spectra obtained with Keck NIRSPEC. In Chapter IV, I report a previously unseen spectral feature at 3.78 μm in disk-integrated spectra of the trailing hemisphere. Using Hapke spectral modeling, I demonstrate that it represents an unidentified radiolytic product of potential relevance to understanding the alteration of endogenic material. Chapter V considers a radiolytic species thought to be independent of endogenic material—hydrogen peroxide (H_2O_2), a species relevant to the oxidation state and habitability of the ocean in the case of mutual exchange through the ice shell. Contrary to laboratory expectations, I observe the largest H_2O_2 absorptions within salty, low-latitude chaos terrain. I hypothesize that this distribution may reflect decreased hydrogen peroxide destruction due to electron scavenging by CO_2 within these same regions, which would suggest an internal

carbon source.

Finally, Chapters VI and VII present preliminary studies of Europa's thermal emission using four images obtained with the Atacama Large Millimeter Array (ALMA) and a global thermophysical model developed to simulate Europa's expected thermal emission. In Chapter VI, I combine a single ALMA image with an observation from the *Galileo* Photopolarimeter Radiometer (PPR) to show that a thermal anomaly seen by the PPR and associated with two potential plume detections is better explained by a locally high thermal inertia than by geologic heating. Chapter VII considers all four ALMA images. While much of the large-scale thermal structure can be readily attributed to albedo variation, modeling of the images reveals a number of localized anomalies, which may indicate variations in geothermal heat flow, thermal inertia, or millimeter emissivity. In the absence of the additional observations needed to distinguish between such possibilities, I construct hypothetical maps presenting the ranges of possible thermal inertia and emissivity values.

PUBLISHED CONTENT AND CONTRIBUTIONS

Trumbo, S. K., M. E. Brown, and K. P. Hand (2020). "Endogenic and exogenic contributions to visible-wavelength spectra of Europa's trailing hemisphere". *The Astronomical Journal* 160.6, p. 282. DOI: 10.3847/1538-3881/abc34c.
S. K. T. conceived of the project, performed the analysis, interpreted the results, and wrote the manuscript. This work was adapted to constitute Chapter III.

Trumbo, S. K., M. E. Brown, and K. P. Hand (2019a). "H_2O_2 within Chaos Terrain on Europa's Leading Hemisphere". *The Astronomical Journal* 158.3, p. 127. DOI: 10.3847/1538-3881/ab380c.
S. K. T. helped conceive of the project and observations, performed the data reduction and analysis, interpreted the results, and wrote the manuscript. This work was adapted to constitute Chapter V.

Trumbo, S. K., M. E. Brown, and K. P. Hand (2019b). "Sodium chloride on the surface of Europa". *Science Advances* 5.6. DOI: 10.1126/sciadv.aaw7123.
S. K. T. influenced the direction of the project, performed the analysis, interpreted the results, and wrote the manuscript. This work was adapted to constitute Chapter II.

Trumbo, S. K., M. E. Brown, and K. P. Hand (2018). "ALMA Thermal Observations of Europa". *The Astronomical Journal* 156.4, p. 161. DOI: 10.3847/1538-3881/aada87.
S. K. T. influenced the direction of the project, wrote the thermal model, performed the modeling and fitting, interpreted the results, and wrote the manuscript. This work was adapted to constitute Chapter VII.

Trumbo, S. K., M. E. Brown, and B. J. Butler (2017a). "ALMA Thermal Observations of a Proposed Plume Source Region on Europa". *The Astronomical Journal* 154.4, p. 148. DOI: 10.3847/1538-3881/aa8769.
S. K. T. helped conceive of the goal of the project, wrote the thermal model, performed the thermal modeling work, interpreted the results, and wrote the manuscript. This work was adapted to constitute Chapter VI.

Trumbo, S. K. et al. (2017b). "A new spectral feature on the trailing hemisphere of Europa at 3.78 microns". *The Astronomical Journal* 153.6, p. 250. DOI: 10.3847/1538-3881/aa6d80.
S. K. T. contributed to the direction of the project, performed the data reduction and analysis, and wrote the manuscript. This work was adapted to constitute Chapter IV.

TABLE OF CONTENTS

LIST OF ILLUSTRATIONS

Number *Page*

LIST OF TABLES

Chapter 1

INTRODUCTION

Discovered by Galileo Galilei in 1610, Europa played a part in ushering in a new era in astronomy. In his *Siderius Nuncius* (Galilei, 1610), Galileo recorded the changing positions of Europa and the other "Medician planets" relative to Jupiter and argued that they must be in orbit around it. His observations of Io, Europa, Ganymede, and Callisto—now collectively referred to as the Galilean satellites—presented the first example of heavenly bodies orbiting one another, providing support for the Copernican heliocentric view of the Solar System. Now, more than 400 years later, we have begun to understand Europa and the Galilean system in remarkable detail, appreciating these satellites as fascinating places in their own right. In 1979, the *Voyager* spacecrafts revealed details of Europa's surface for the first time, returning images of an icy surface crosscut by dark fractures and featuring very few craters, which some interpreted as evidence for liquid water and resurfacing (Squyres et al., 1983). Two decades later, the *Galileo* mission to the Jovian system revealed the signatures of an induced magnetic field at Europa (Kivelson et al., 2000), providing strong evidence for a conductive layer beneath the surface, most likely in the form of a salty, liquid-water ocean. In fact, Europa, the smallest of the Galilean moons, may harbor the largest body of liquid water in the Solar System—an ocean ~100 km in depth that sits above a silicate seafloor (Anderson et al., 1998; Schubert et al., 2009). This water-rock connection may have facilitated rich aqueous geochemistry over Europa's history (Zolotov and Kargel, 2009), potentially producing an environment hospitable to life (Hand et al., 2009). As a result, Europa has been catapulted from a wandering point of light in the night sky to a prime target for exploration in the Solar System, and constraining the chemistry of its ocean has become a primary goal of Europa science.

Locked beneath a kilometers-thick ice shell, Europa's ocean cannot currently be studied directly. However, *Voyager* and *Galileo* images have shown us that Europa's young surface is pervaded by tectonic fractures, dilational bands, and highly disrupted "chaos" terrain indicative of recent geologic activity and potential material exchange through the ice shell (Kattenhorn and Hurford, 2009; Prockter and Patterson, 2009; Doggett et al., 2009). The surface chemistry of Europa may thus provide a window to its internal composition, but the degree to which the ocean

and the surface are in contact is highly uncertain. The interpretation of surface materials as oceanic signatures is further complicated by the fact that Europa orbits within Jupiter's magnetosphere, which results in the constant alteration of its surface composition by sulfur implantation, particle irradiation, and consequent radiolyic processing (e.g. Paranicas et al., 2001; Paranicas, 2002; Paranicas et al., 2009). Io, which orbits interior to Europa, is the most volcanically active body in the Solar System, and its volcanoes are a constant source of electrons, sulfur, and other ions that become entrained within Jupiter's rapidly rotating magnetic field. As Europa is tidally locked to Jupiter, and as Jupiter's rotational period is much shorter than Europa's orbital period, most of these particles and nearly all of the Iogenic sulfur preferentially impact Europa's trailing hemisphere. The very most energetic electrons, which move counter to Jupiter's rotational direction, are an important exception that bombard Europa's leading hemisphere. Thus, the entire surface of Europa is irradiated and externally processed to some degree, resulting in a complex tapestry of internally and externally derived species that can obscure potential connections to the ocean. Even more complexity arises when one considers the potential flux of such radiolytic products into the subsurface ocean via mutual exchange through the ice shell.

Through a variety of astronomical observations of Europa, this thesis seeks to advance our understanding of two key factors in inferring the ocean composition from the surface composition: the balance of endogenous and exogenous processes in shaping the surface chemistry and the extent and locations of modern geologic activity.

1.1 Unraveling Europa's Surface Salt Chemistry

The *Galileo* Near Infrared Mapping Spectrometer (NIMS) revealed that, while the leading hemisphere of Europa is comparatively ice-rich, the trailing hemisphere is characterized by the presence of hydrated, non-ice material exhibiting some association with geologic features. This non-ice component was initially interpreted to reflect hydrated magnesium sulfate salts from the internal ocean (McCord et al., 1998; McCord et al., 1999), which was consistent with the prediction that aqueous differentiation of chondritic material and long-term leaching from a chondritic seafloor would result in an ocean dominated by sodium and magnesium sulfates (Kargel, 1991; Fanale et al., 2001). However, this interpretation was soon questioned. Further investigation of the NIMS data argued that sulfuric acid hydrate ($H_2SO_4 \cdot nH_2O$), an expected product of the trailing hemisphere's radiolytic sulfur

chemistry, may provide a more likely explanation (Carlson et al., 1999a; Carlson et al., 2002; Carlson et al., 2005). This hypothesis readily explained the predominance of hydrate on the trailing hemisphere—an asymmetry not easily attributable to endogenic sources—but seemed in conflict with the observed hydrate enhancements within geologic lineaments. At the spectral resolution of NIMS, both hypotheses were equally consistent with the spectra themselves and, as a result, the debate between sulfate salts and sulfuric acid continued for more than a decade.

Later analyses invoked mixtures of sulfuric acid hydrate and sulfate salts to explain the NIMS data, with sulfuric acid hydrate dominating the sulfur-bombarded trailing hemisphere and hydrated sulfate salts dominating disrupted terrain elsewhere (Dalton, 2007; Dalton et al., 2012; Dalton et al., 2013). Although the applicability of the leaching experiments performed by Fanale et al. (2001) had since been questioned (McKinnon and Zolensky, 2003), these post-*Galileo* investigations still primarily considered sulfates as the native salt candidates. This historical dominance of the sulfate-salt hypothesis was partly facilitated by the low spectral resolution of NIMS data, at which hydrated sulfates provided satisfactory fits to the observed spectra. However, at sufficiently high spectral resolution, most of the sulfate salts considered have comparatively narrow, distinct absorptions in addition to the broad hydration bands seen by NIMS (e.g. Dalton et al., 2005).

Recent ground-based observations have provided spectra of Europa's surface at much higher spectral resolution, and have begun to challenge the traditional view. Using the OSIRIS spectrograph at the W. M. Keck Observatory, Brown and Hand (2013) detected a new spectral feature consistent with epsomite ($MgSO_4 \cdot 7H_2O$), but showed that its distribution reflects that of a radiolytic product, rather than an endogenous substance. The feature appears constrained to the sulfur-bombarded trailing hemisphere and spatially correlated with the radiolytically produced sulfuric acid hydrate, which was also needed to fit their spectra. Fischer et al. (2015) used the same dataset to demonstrate that the leading hemisphere chaos regions are spectroscopically distinct from both the spectrally icy portions of the leading hemisphere and the sulfur-bombarded trailing hemisphere, suggesting an endogenous composition separate from the chemistry of sulfur radiolysis. In contrast with the sulfate hypothesis of the *Galileo* era, the leading hemisphere chaos spectra lack any of the sulfate absorptions, including those of epsomite, that should be visible at the OSIRIS spectral resolution. In fact, they lack any diagnostic spectral features, other than those of water ice. However, their geographic association with chaos suggests

a salty composition. Based on the ground-based observations, Brown and Hand (2013) and Fischer et al. (2015) hypothesized that perhaps the truly endogenous salts are chlorides, which are featureless across the near-infrared wavelengths, and that these chlorides then convert to sulfates via the sulfur radiolytic chemistry of the trailing hemisphere.

Chapters II and III of this thesis address this chloride hypothesis by using visible-wavelength spectroscopy from the Hubble Space Telescope (HST) to disentangle the endogenic and exogenic influences on Europa's salt chemistry. In Chapter II, I discuss the discovery of an absorption feature indicative of irradiated sodium chloride (NaCl) on the leading hemisphere, constituting the first unambiguous detection of an endogenous surface species and providing support to the chloride hypothesis of Brown and Hand (2013) and Fischer et al. (2015). In Chapter III, I focus on the trailing hemisphere and deciphering potential evidence for the incorporation of endogenous material into the radiolytic sulfur cycle.

1.2 Radiolytic Species of Potential Importance to the Interior

The continual radiolytic processing of Europa's surface by energetic particles within Jupiter's magnetosphere drives much of the known surface chemistry. In addition to the sulfuric acid hydrate discussed in the previous section, sulfur radiolysis on the trailing hemisphere leads to the likely production of sulfur allotropes implicated in visible spectra (Spencer et al., 1995; Carlson et al., 2009, see Chapter III) and sulfur dioxide (SO_2) evident in the UV (Lane et al., 1981; Noll et al., 1995). As described in the previous section, such radiolytic cycling may also incorporate pre-existing endogenic material, making the study of radiolytic products relevant to determining the native surface chemistry. Furthermore, in the case of mutual exchange through the ice shell, radiolytic products may influence the ocean chemistry, even if they do not originate in the interior. This idea is particularly important for the potential habitability of Europa's subsurface ocean, because, though water-rock cycling at the seafloor could act a source of reductants to the internal ocean, a corresponding source of oxidants would be required for the existence of life (Chyba, 2000; Hand et al., 2009). On Europa, these would have to come from the radiolysis of its surface water ice, which creates an oxidizing surface featuring molecular oxygen (O_2) (Spencer et al., 1995; Johnson and Quickenden, 1997) and hydrogen peroxide (H_2O_2) (Carlson et al., 1999b).

In Chapters IV and V, I use near-infrared observations from the W. M. Keck Ob-

servatory to explore two radiolytic species of potential relevance to the internal chemistry. In Chapter IV, I investigate a new spectral feature on Europa's trailing hemisphere and demonstrate that it reflects a previously undetected radiolytic product that may tie-in with the chloride-to-sulfate hypothesis of the previous section. Chapter V maps the spatial distribution of H_2O_2, an oxidant of importance for Europa's habitability. Contrary to laboratory expectations, I find the most H_2O_2 within salty, geologically resurfaced terrain. I hypothesize that such terrain may contain abundant CO_2, a species known to increase H_2O_2 yields in the lab (Moore and Hudson, 2000), which would suggest an interior source for Europa's carbon.

1.3 Europa's Thermal Emission as a Probe of Surface Processes

The young surface age and abundant geology of Europa suggest a history of activity that continued at least until the geologically recent past. If Europa remains active today, then closer study of internally derived materials may be possible at sites of ongoing or recent exchange. Indeed, recent observations from both HST and Keck and re-analysis of Galileo magnetic and Plasma Wave Spectrometer data have hinted that Europa may actively be venting plumes of water vapor into space (Roth et al., 2014b; Sparks et al., 2016; Sparks et al., 2017; Paganini et al., 2020; Jia et al., 2018). However, these detections have been sporadic, tenuous, and difficult to validate (Roth et al., 2014a; Sparks et al., 2019). Spatially resolved thermal measurements can constitute a robust alternative approach to identifying active locations, by revealing temperature signatures of warm subsurface material delivered to or near the cold surface ice. Indeed, active hotspots are associated with both the plumes of Enceladus (Spencer et al., 2006) and the volcanoes of Io (Spencer et al., 1990). Furthermore, surface temperature measurements can provide an additional window on the influence of exogenous processes, by probing the effects of particle irradiation, sputtering, micrometeorite bombardment, and diurnal sublimation cycling on surface texture and composition, which relate to the surface thermophysical properties.

Chapters VI and VII present analyses of Europa's thermal emission using four images obtained with the Atacama Large Millimeter Array (ALMA) and a global thermophysical model I develop to simulate Europa's expected brightness temperatures. These ALMA images comprise the first spatially resolved thermal dataset with complete coverage of Europa's surface. In Chapter VI, I combine a single ALMA observation with a nighttime image of the same region from the the *Galileo* Photopolarimeter Radiometer (PPR) to investigate a thermal anomaly seen by the

PPR and associated with two proposed plume detections. I show that this anomaly likely reflects a locally high thermal inertia, rather than active geologic heating. Chapter VII considers the entire ALMA dataset simultaneously. By employing my thermal model to simulate Europa's emission according to its best-fit thermophysical properties, I reveal a number of localized anomalies. I then construct spatial maps of the ranges of thermal inertia and millimeter emissivity values that can explain the anomalies and discuss comparisons with Europa's geographic and compositional units.

References

Anderson, J. D. et al. (1998). "Europa's differentiated internal structure: Inferences from four Galileo encounters". *Science* 281.5385, pp. 2019–2022.

Brown, M. E. and K. P. Hand (2013). "Salts and Radiation Products on the Surface of Europa". *The Astronomical Journal* 145.4, p. 110.

Carlson, R. W., R. E. Johnson, and M. S. Anderson (1999a). "Sulfuric Acid on Europa and the Radiolytic Sulfur Cycle". *Science* 286.5437, pp. 97–99.

Carlson, R. W. et al. (1999b). "Hydrogen Peroxide on the Surface of Europa". *Science* 283.5410, pp. 2062–2064.

Carlson, R. W. et al. (2002). "Sulfuric Acid Production on Europa: The Radiolysis of Sulfur in Water Ice". *Icarus* 157.2, pp. 456–463.

Carlson, R. W. et al. (2005). "Distribution of hydrate on Europa: Further evidence for sulfuric acid hydrate". *Icarus* 177.2, pp. 461–471.

Carlson, R. W. et al. (2009). "Europa". Ed. by R. T. Pappalardo, W. B. McKinnon, and K. Khurana. Tucson, AZ: The University of Arizona Press. Chap. Europa's Surface Composition, pp. 283–328.

Chyba, C. F. (2000). "Energy for microbial life on Europa". *Nature* 403.6768, pp. 381–382.

Dalton, J. B. (2007). "Linear mixture modeling of Europa's non-ice material based on cryogenic laboratory spectroscopy". *Geophysical Research Letters* 34.21, p. L21205.

Dalton, J. B., J. H. Shirley, and L. W. Kamp (2012). "Europa's icy bright plains and dark linea: Exogenic and endogenic contributions to composition and surface properties". *Journal of Geophysical Research: Planets* 117.E3.

Dalton, J. B. et al. (2005). "Spectral comparison of heavily hydrated salts with disrupted terrains on Europa". *Icarus* 177.2, pp. 472–490.

Dalton, J. B. et al. (2013). "Exogenic controls on sulfuric acid hydrate production at the surface of Europa". *Planetary and Space Science* 77, pp. 45–63.

Doggett, T. et al. (2009). "Europa". Ed. by R. T. Pappalardo, W. B. McKinnon, and K. Khurana. Tucson, AZ: University of Arizona Press. Chap. Geologic Stratigraphy and Evolution of Europa's surface, pp. 137–160.

Fanale, F. P. et al. (2001). "An experimental estimate of Europa's "ocean" composition independent of Galileo orbital remote sensing". *Journal of Geophysical Research: Planets* 106.E7, pp. 14595–14600.

Fischer, P. D., M. E. Brown, and K. P. Hand (2015). "Spatially Resolved Spectroscopy of Europa: The Distinct Spectrum of Large-Scale Chaos". *The Astronomical Journal* 150.5, p. 164.

Galilei, G. (1610). "Siderius Nuncius". Translated by Carlos, E. S., *A Source Book on Astronomy* (1929). Ed. by H Shapley and Howarth. New York, NY: McGraw-Hill.

Hand, K. P. et al. (2009). "Europa". Ed. by R. T. Pappalardo, W. B. McKinnon, and K. Khurana. Tucson, AZ: The University of Arizona Press. Chap. Astrobiology and the Potential for Life on Europa, pp. 589–630.

Jia, X. et al. (2018). "Evidence of a plume on Europa from Galileo magnetic and plasma wave signatures". *Nature Astronomy* 2.6, pp. 459–464.

Johnson, R. E. and T. I. Quickenden (1997). "Photolysis and radiolysis of water ice on outer solar system bodies". *Journal of Geophysical Research: Planets* 102.E5, pp. 10985–10996.

Kargel, J. S. (1991). "Brine volcanism and the interior structures of asteroids and icy satellites". *Icarus* 94.2, pp. 368–390.

Kattenhorn, S. A. and T. Hurford (2009). "Europa". Ed. by R. T. Pappalardo, W. B. McKinnon, and K. Khurana. Tucson, AZ: The University of Arizona Press. Chap. Tectonics of Europa, pp. 199–236.

Kivelson, M. G. et al. (2000). "Galileo magnetometer measurements: A stronger case for a subsurface ocean at Europa". *Science* 289.5483, pp. 1340–1343.

Lane, A. L, R. M. Nelson, and D. L Matson (1981). "Evidence for sulphur implantation in Europa's UV absorption band". *Nature* 292, pp. 38–39.

McCord, T. B. et al. (1998). "Salts on Europa's Surface Detected by Galileo's Near Infrared Mapping Spectrometer". *Science* 280.5367, pp. 1242–1245.

McCord, T. B. et al. (1999). "Hydrated salt minerals on Europa's surface from the Galileo near-infrared mapping spectrometer (NIMS) investigation". *Journal of Geophysical Research: Planets* 104.E5, pp. 11827–11851.

McKinnon, W. B. and M. E. Zolensky (2003). "Sulfate content of Europa's ocean and shell: Evolutionary considerations and some geological and astrobiological implications". *Astrobiology* 3.4, pp. 879–897.

Moore, M. H. and R. L. Hudson (2000). "IR Detection of H_2O_2 at 80 K in Ion-Irradiated Laboratory Ices Relevant to Europa". *Icarus* 145.1, pp. 282–288.

Noll, K. S., H. A. Weaver, and A. M. Gonnella (1995). "The albedo spectrum of Europa from 2200 Å to 3300 Å". *Journal of Geophysical Research: Planets* 100.E9, pp. 19057–19059.

Paganini, L. et al. (2020). "A measurement of water vapour amid a largely quiescent environment on Europa". *Nature Astronomy* 4.3, pp. 266–272.

Paranicas, C. (2002). "The ion environment near Europa and its role in surface energetics". *Geophysical Research Letters* 29.5.

Paranicas, C., R. W. Carlson, and R. E. Johnson (2001). "Electron bombardment of Europa". *Geophysical Research Letters* 28.4, pp. 673–676.

Paranicas, C. et al. (2009). "Europa". Ed. by R. T. Pappalardo, W. B. McKinnon, and K. Khurana. Tucson, AZ: The University of Arizona Press. Chap. Europa's Radiation Environment and its Effects on the Surface, pp. 529–544.

Prockter, L. M. and G. W. Patterson (2009). "Europa". Ed. by R. T. Pappalardo, W. B. McKinnon, and K. Khurana. Tucson, AZ: The University of Arizona Press. Chap. Morphology and Evolution of Europa's Ridges and Bands, pp. 237–258.

Roth, L. et al. (Oct. 2014a). "Orbital apocenter is not a sufficient condition for HST/STIS detection of Europa's water vapor aurora". *PNAS* 111.48, E5123–E5132.

Roth, L. et al. (Jan. 2014b). "Transient water vapor at Europa's south pole". *Science* 343.6167, pp. 171–174.

Schubert, G., F. Sohl, and H. Hussmann (2009). "Interior of Europa". *Europa*. Ed. by R. T. Pappalardo, W. B. McKinnon, and K. Khurana. The University of Arizona Press. Chap. Interior of Europa, pp. 353–367.

Sparks, W. B. et al. (2019). "A search for water vapor plumes on Europa using SOFIA". *The Astrophysical Journal Letters* 871.1, p. L5.

Sparks, W. B. et al. (2016). "Probing for evidence of plumes on Europa with HST/STIS". *The Astrophysical Journal* 829.2, p. 121.

Sparks, W. B. et al. (2017). "Active Cryovolcanism on Europa?" *The Astrophysical Journal* 839.2, p. L18.

Spencer, J. R., W. M. Calvin, and M. J. Person (1995). "Charge-coupled device spectra of the Galilean satellites: Molecular oxygen on Ganymede". *Journal of Geophysical Research: Planets* 100.E9, pp. 19049–19056.

Spencer, J. R. et al. (1990). "Discovery of hotspots on Io using disk-resolved infrared imaging". *Nature* 348.6302, pp. 618–621.

Spencer, J. R. et al. (2006). "Cassini encounters Enceladus: Background and the discovery of a south polar hot spot". *Science* 311.5766, pp. 1401–1405.

Squyres, S. W. et al. (1983). "H_2O_2 within Chaos Terrain on Europa's Leading Hemisphere". *Nature* 5897.301, pp. 225–226.

Zolotov, M. Y. and J. S. Kargel (2009). “On the Chemical Composition of Europa’s Icy Shell, Ocean, and Underlying Rocks”. *Europa*. Ed. by R. T. Pappalardo, W. B. McKinnon, and K. Khurana. The University of Arizona Press. Chap. On the Chemical Composition of Europa’s Icy Shell, Ocean, and Underlying Rocks, pp. 431–457.

Chapter 2

SODIUM CHLORIDE ON THE SURFACE OF EUROPA

Trumbo, S. K., M. E. Brown, and K. P. Hand (2019). "Sodium chloride on the surface of Europa". *Science Advances* 5.6. DOI: 10.1126/sciadv.aaw7123.

ABSTRACT

The potential habitability of Europa's subsurface ocean depends on its chemical composition, which may be reflected in that of Europa's geologically young surface. Investigations using Galileo Near Infrared Mapping Spectrometer data led to the prevailing view that Europa's endogenous units are rich in sulfate salts. However, recent ground-based infrared observations have suggested that, while regions experiencing sulfur radiolysis may contain sulfate salts, Europa's more pristine endogenous material may reflect a chloride-dominated composition. Chlorides possess no identifying spectral features at infrared wavelengths, but develop distinct visible-wavelength absorptions under irradiation, like that experienced on the surface of Europa. Using spectra obtained with the Hubble Space Telescope, we present the detection of a 450 nm absorption indicative of irradiated sodium chloride on the surface. The feature correlates with geologically disrupted chaos terrain, suggesting an interior source. The presence of endogenous sodium chloride on the surface of Europa has significant implications for our understanding of its subsurface chemistry.

2.1 Introduction

Beneath its icy crust, Europa hosts a salty, liquid-water ocean in contact with a rocky seafloor (Anderson et al., 1998; Kivelson et al., 2000; Zimmer et al., 2000), making it an exciting place to explore habitability in the Solar System. However, the ocean's potential to support life relies heavily on its composition and chemical energy budget (Hand et al., 2009; Chyba and Hand, 2001), which remain largely unconstrained. Currently, our best window to understanding Europa's ocean chemistry is to study the composition of its geologically young and active surface. Prevailing interpretation of spectra from the Galileo Near Infrared Mapping Spectrometer (NIMS) suggests a surface dominated by three chemical terrains: water ice, sulfuric acid hydrate, and an additional non-ice material, which, since the time of the Galileo mission, has been interpreted as endogenous sulfate salts from the interior ocean (McCord et al., 1998; Dalton, 2007; Dalton et al., 2012; Dalton et al., 2013). However, while the likely presence of sulfuric acid hydrate is predicted as a result of radiolytic chemistry occurring on the heavily irradiated and sulfur-bombarded trailing hemisphere (Carlson et al., 1999; Carlson et al., 2002; Carlson et al., 2005), the composition of non-ice material elsewhere is not well constrained by the NIMS data. In fact, the enduring concept of a native composition rich in sulfate salts is largely facilitated by the low spectral resolution of NIMS, at which distinct sulfate absorptions are unresolved (e.g., Dalton et al. (2005)).

Recent ground-based infrared observations, with ~40 times higher spectral resolution than NIMS, have revealed an absorption feature consistent with magnesium sulfate (Brown and Hand, 2013). However, this feature is constrained to the sulfur-bombarded trailing hemisphere and spatially coincident with the proposed sulfuric acid hydrate, suggesting a radiolytic, rather than endogenous, origin. Furthermore, the same observations have shown no evidence of sulfate absorptions in regions interpreted to contain endogenous material that has been sheltered from sulfur radiolysis (Fischer et al., 2015). In fact, they revealed that the leading hemisphere chaos regions are spectroscopically distinct, indicating a composition different from both the spectrally icy high latitudes of the leading hemisphere and the exogenously altered terrain of the trailing hemisphere (Fischer et al., 2015). As chaos terrain is geologically young, extensively disrupted, and potentially indicative of locations of subsurface upwelling or melt-through (e.g., (Collins and Nimmo, 2009; O'Brien et al., 2002; Sotin et al., 2002)), and as the leading hemisphere chaos regions are shielded from the sulfur implantation of the trailing hemisphere, the composition of these regions may best represent that of Europa's endogenous material. How-

Table 2.1: HST STIS G430L/G750L observations of Europa.

Date (UT)	Time (Start/End)	Sub-observer Longitude	Sub-observer Latitude	Angular Size of Europa (arcsec)
2017 May 23	00:20/01:41	224	-3.06	0.91
2017 Jun 29	08:19/08:55	47	-2.91	0.82
2017 Aug 1	04:43/05:20	133	-2.91	0.75
2017 Aug 6	12:27/13:47	314	-2.92	0.74

ever, their spectra are categorically smooth at higher spectral resolution, lacking any identifiable infrared spectral features other than those of water ice. Nevertheless, the unique geology and 1.5 – 4 μm spectra (Fischer et al., 2015; Fischer et al., 2017) of leading hemisphere chaos terrain suggest a salty composition. Chloride salts provide a potential explanation (Fischer et al., 2015), as they are among the few salts that are spectrally smooth at infrared wavelengths. For the same reason, however, they cannot be confirmed by currently available data.

Though spectrally bland in the infrared, alkali chlorides develop distinct spectral features at visible wavelengths under particle irradiation. The bombarding particles lead to the growth of "color centers" by creating anion vacancies in the crystal structures, which trap free electrons and cause compositionally diagnostic absorptions (e.g., Seitz (1946), Schneider and Bailey (1969), and Schwartz et al. (2008)). In fact, laboratory experiments have demonstrated that color centers can form in sodium chloride (NaCl) and NaCl brine evaporites under Europa-like surface conditions (Hand and Carlson, 2015b; Poston et al., 2017), producing colors in laboratory samples that appear visually similar to those captured in Galileo images of Europa's surface (e.g., Geissler et al. (1998)). Spectrally, these colors largely result from two distinct absorptions caused by two types of color centers—a strong F-center absorption near 460 nm due to individual electrons trapped within single Cl- vacancies, and a weaker M- (or F2-) center absorption near 720 nm due to binary aggregates of F-centers. To investigate the hypothesis that Europa's endogenous units contain chloride salts, we used the Hubble Space Telescope (HST) to search for signatures of these color centers on the surface.

2.2 Results and Discussion

Using the Space Telescope Imaging Spectrograph (STIS), we observed Europa across four HST visits (Table 2.1), obtaining the first spatially resolved spectral dataset of the entire surface at wavelengths of 300 – 1000 nm. We observe a

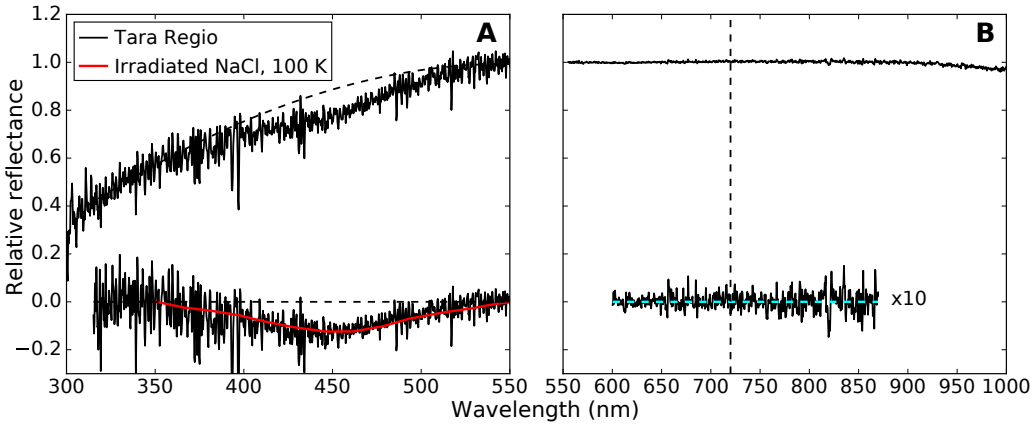

Figure 2.1: HST/STIS spectra showing a distinct 450 nm spectral feature, consistent with an NaCl F-center absorption, and a clear lack of a 720 nm NaCl M-center absorption. (A) A single spectrum from within Tara Regio, which exhibits a particularly strong 450 nm absorption. The dashed line is a third-order polynomial continuum fit. The continuum-removed feature is included underneath the spectrum. Overlain in red is a continuum-removed laboratory spectrum of irradiated NaCl at 100 K, taken from Figure 2 of (Poston et al., 2017). This spectrum corresponds to an NaCl F-center absorption that has evolved in the absence of unrealistic laboratory radiation fluxes. The laboratory F-center absorption has been scaled to match the depth of the observed feature. (B) A high signal-to-noise spectrum produced by averaging all spectra from locations exhibiting a 450 nm feature, weighted by the strength of that feature in each location. The weighted average is divided by the average of all spectra from locations in which the 450 nm feature is absent and rescaled to approximate the known Europa continuum. A continuum-removed version is shown underneath the spectrum, where the vertical dashed line indicates the anticipated band center at 720 nm.

broad absorption near 450 nm (Figure 2.1a), which corresponds well to the F-center absorption of irradiated NaCl (Hand and Carlson, 2015b; Poston et al., 2017). This feature is located exclusively on the leading hemisphere and correlates with chaos terrain (Figure 2.2). The deepest absorptions fall within the large-scale chaos region Tara Regio, presumably contributing to its distinct yellow color in Galileo images of Europa. Clear absorptions are also associated with eastern Powys Regio, lenticulated terrain northwest of Tara Regio, and, to a much lesser extent, somewhat older terrains of the leading hemisphere. This marked correlation with geologically young chaos regions suggests an interior source. Chlorides emplaced onto the surface in these locations would be subjected to irradiation by high-energy (greater than ~20 MeV) electrons, which, in contrast to the majority of the impinging sulfur ions and lower-energy electrons (e.g., (Dalton et al., 2013; Paranicas et al., 2001)),

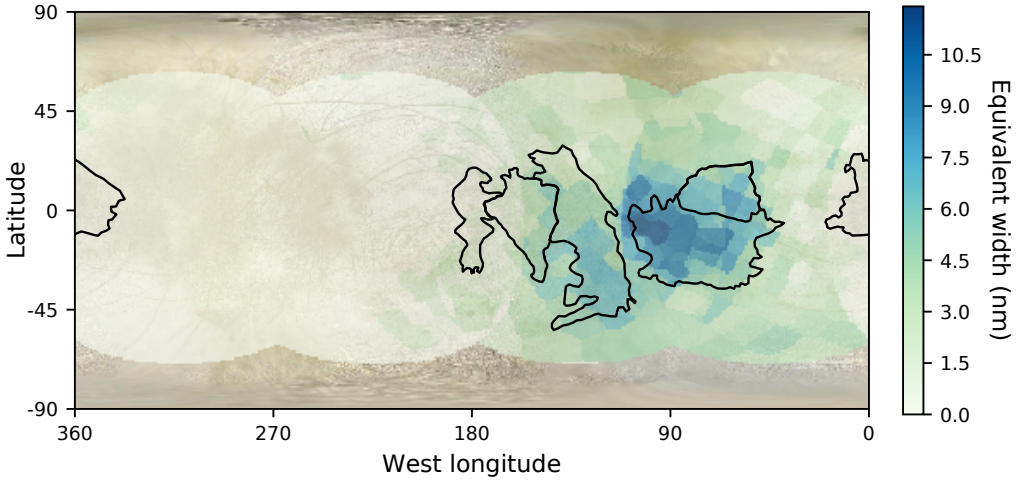

Figure 2.2: A map of the strength of the 450 nm absorption. The observed feature maps solely to the leading hemisphere. Black outlines correspond to large-scale chaos regions, mapped approximately from Doggett et al. (2009). The largest absorptions fall within the chaos region Tara Regio (~85" W), with additional concentration in eastern Powys Regio (~125" W). This distribution is separate from the geography of sulfur radiolysis and suggests a subsurface source, consistent with the chloride hypothesis for Europa's endogenous material. The spatial resolution of the mapped data is ~150 km at the sub-observer point. Background image credit: NASA/JPL/Björn Jónsson/Steve Albers.

primarily impact the leading hemisphere (Nordheim et al., 2018), thereby providing the necessary energy for color center formation. As Tara Regio is the most irradiated leading-hemisphere chaos region (Nordheim et al., 2018), the observed distribution of the potential NaCl F-center feature is consistent with a chloride-rich composition for the endogenous material identified in infrared spectra of all leading-hemisphere chaos terrain (Fischer et al., 2015; Fischer et al., 2017).

Unlike the laboratory spectra, our data show no evidence for an NaCl M-center absorption near 720 nm (Figure 2.1b, Fig 2.3). By averaging all of the spectra from locations that exhibit the 450 nm absorption, weighted by the strength of the feature in each location, we conservatively rule out a band strength greater than 0.5%. This lack of an M-center absorption is perhaps unsurprising, as the laboratory experiments in which the M-center was observed (Hand and Carlson, 2015b; Poston et al., 2017) used radiation fluxes $10^4 - 10^5$ times the true flux experienced on Europa. While such high fluxes can accurately simulate many aspects of Europa's radiation chemistry and can achieve doses equivalent to hundreds of years on the surface in hours to days of real time, they inaccurately reflect kinetic effects controlling the formation and

decay of color centers. Single-vacancy F-centers appeared immediately under such conditions, but binary M-centers took the rough equivalent of 1 year on Europa to form (Poston et al., 2017). Yet, when the radiation was halted, both F- and M-centers decayed significantly on timescales of hours (Poston et al., 2017). Indeed some NaCl irradiation experiments, performed under different conditions, have observed only F-center production (Fanale et al., 1974; Nash and Fanale, 1977). This behavior suggests that M-centers would likely never form under the low radiation flux at Europa, reflecting competition between their slow growth and the contributions of decay processes, such as photobleaching (e.g., Mador et al. (1954) and Georgiou and Pollock (1989)), which can influence the relative abundance of NaCl color centers. Finally, this behavior may also explain the band center of the observed 450 nm feature. After the laboratory radiation was halted, the F-center absorption shifted to shorter wavelengths as it decayed (Poston et al., 2017). Thus, as the radiation experienced at Europa is negligible relative to the fluxes applied in the lab, we may expect F-center absorptions on Europa to appear shortward of 460 nm. Indeed, the F-center absorption of irradiated NaCl that was allowed to evolve at 100 K without further irradiation (Poston et al., 2017) corresponds remarkably well to our observed feature (Figure 2.1a), though it is worth noting that this laboratory spectrum corresponds to irradiated anhydrous NaCl crystals in the absence of water ice (Poston et al., 2017). One might instead expect that the low temperatures and icy environment of Europa's surface result in hydrohalite ($NaCl \cdot 2H_2O$), for which color center formation has not been studied in the same way. However, laboratory evidence for the rapid dehydration of hydrohalite under Europa-like conditions (Thomas et al., 2017) and the formation of F- and M-centers at the same band positions in NaCl brine evaporites (Hand and Carlson, 2015b) support the applicability of experiments involving anhydrous NaCl.

NaCl provides an elegant explanation for the observed 450 nm feature, its geographic distribution, and prior infrared spectra interpreted to reflect endogenous material (Fischer et al., 2015; Fischer et al., 2017). However, alternative candidates warrant discussion. In fact, the 450 nm feature was weakly visible in disk-integrated spectra of Europa's leading hemisphere taken in the 1990s, but was attributed to sulfur-bearing species, despite poor fits (Spencer et al., 1995). Our dataset, however, shows that the feature is concentrated in chaos and separate from the geography of sulfur radiolysis, necessitating a separate explanation. Instead, we examine the spectra of several other irradiated salts (Figure 2.4), including magnesium chloride, potassium chloride, and multiple sulfate and carbonate species (Hand and Carlson,

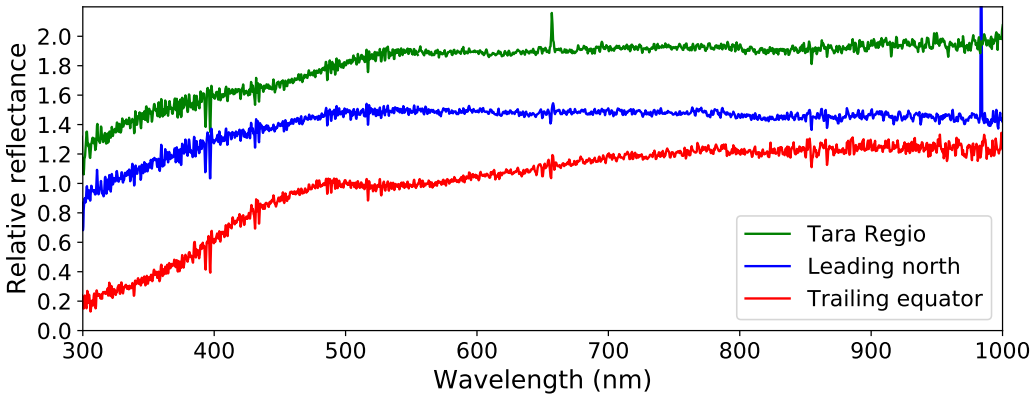

Figure 2.3: Representative HST/STIS spectra of the three chemical terrains on the surface of Europa. In green is a single spectrum from the leading hemisphere chaos region Tara Regio, which contains a clear 450 nm absorption consistent with irradiated NaCl. In contrast, representative spectra from the spectrally icy northern mid-latitudes of the leading hemisphere (31” N, 43” W) (blue) and from near the apex of the trailing hemisphere (2” N, 273” W) (red) do not display this feature. Beyond ~600 nm, all three spectra are quite similar and appear to lack any strong absorptions, though some artifacts of the defringing process remain, particularly beyond ~800 nm. The spectra are scaled to unity at 550 nm. The blue and green spectra are offset vertically by 0.5 and 0.9 units, respectively. Significant slit losses and the broad point spread function of STIS made determination of the continuum shape difficult for the G750L data (~550 – 1000 nm). We correct for this by scaling the spectra at these wavelengths by the functional relationship between the average of our HST G750L spectra of the leading hemisphere and the known continuum of the leading hemisphere over the same wavelength range (Spencer et al., 1995; McFadden et al., 1980). The G430L portions of the spectra (~300 – 550 nm) have been smoothed to match the signal-to-noise of the longer wavelengths.

2015b; Nash and Fanale, 1977; Hibbitts et al., 2019; Hand and Carlson, 2015a). Of these spectra, only NaCl is consistent with our observed feature.

The presence of NaCl on Europa has important implications for our understanding of the internal chemistry and its geochemical evolution through time. Whereas aqueous differentiation of chondritic material and long-term leaching from a chondritic seafloor can result in a system rich in sulfates (Kargel, 1991; Fanale et al., 2001), more extensive hydrothermal circulation, as on Earth, may lead to an NaCl-rich ocean (Kargel, 2000). Indeed, the plume chemistry of Enceladus, which is perhaps the best analog to Europa, suggests an NaCl-dominated ocean (Waite et al., 2006) and a hydrothermally active seafloor (Waite et al., 2017). However, the compositional relationship between Europa’s ocean and its endogenous material is unknown, and

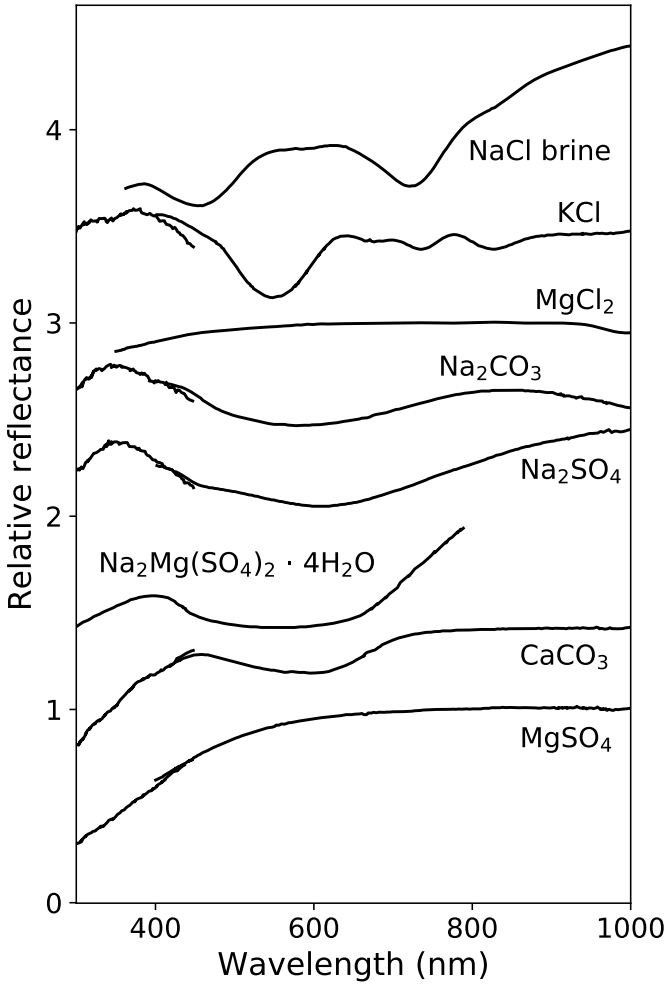

Figure 2.4: Laboratory spectra of select irradiated salts. Here, we reproduce a selection of irradiated salt spectra that can be examined for the presence of a 450 nm absorption. With the exception of the NaCl brine taken from Hand and Carlson (2015b), all of the spectra shown were taken at room temperature. The bloedite spectrum ($Na_2Mg(SO_4)_2 \cdot 4H_2O$) is from Nash and Fanale (1977), the $MgCl_2$ spectrum is from Hand and Carlson (2015a), and the remaining salt spectra are from Hibbitts et al. (2019). Of all of the spectra, only NaCl can explain the observed 450 nm absorption on Europa, and most have strong absorptions elsewhere that we do not observe in our HST data. All spectra are normalized to unity at 750 nm, and each spectrum is offset vertically by 0.4 units from the one below it.

the surface may simply represent the end result of a compositional stratification within the ice shell (e.g., Zolotov and Shock (2001)). Regardless of whether the observed NaCl directly relates to the ocean composition, its presence warrants a re-evaluation of our understanding of the geochemistry of Europa.

2.3 Materials and Methods

We observed Europa with HST/STIS across four visits, the dates, times, and geometries of which are given in Table 2.1. During each visit, we stepped the 52" x 0.1" slit across the full disk of Europa in both the G430L and G750L first-order spectroscopy modes (R~500). Together, these settings provided spectra spanning wavelengths of ~300 – 1000 nm. We acquired spectra at each slit position over 9-second (G750L) or 10-second (G430L) integration times. Flux- and wavelength-calibrated spectral data products were then delivered after standard reduction via the STIS calibration pipeline (calstis). We reprocess the G750L data using the same pipeline, but include the calstis defringing procedures to remove substantial fringes from the longest-wavelength data. We obtain individual spectra by extracting single rows of the 2D spectral images, corresponding to the 0.05" pixel-scale (~150 km diffraction-limited spatial resolution at 450 nm wavelengths). We then divide the ASTM E-490 solar reference spectrum (ASTM, 2000) into the extracted spectra, in order to convert each to reflectance and search for absorption features.

To isolate the 450 nm absorption, we perform continuum fitting and removal on each extracted spectrum. We then calculate absorption band strengths across the surface. For most spectra, we fit a third-order polynomial between 310 and 550 nm, excluding the region corresponding to the F-center absorption (350 – 530 nm). Small variations on these parameters are made when necessary to achieve a satisfactory continuum fit. We then divide each spectrum by its continuum fit and integrate the residual absorption to calculate the equivalent width (i.e. the width of a 100% absorption with the same integrated area). We choose to use a third-order polynomial for the fitting because it better matches the continuum shape, particularly for the transition between the trailing and leading hemispheres. However, mapping using second-order continua produces qualitatively identical results. In mapping the calculated band strengths, we average the values in overlapping regions. We leave out data very near the limb of Europa, as the spectra are poorer quality and make quantifying weak absorptions difficult.

We attempt to place limits on the absence of a 720 nm M-center absorption in our data. To achieve a high signal-to-noise spectrum that represents material interpreted to contain NaCl, we average all spectra from locations where we observe a 450 nm absorption, weighted by the strength of the feature in each location. However, while the noise in this resulting average is reduced, residual solar lines persist due to the somewhat lower spectral resolution of the solar reference spectrum (ASTM,

2000). In addition, residual artifacts of the defringing process remain. To remove these effects and achieve the highest possible quality spectrum, we then divide by the average of all spectra from regions where the 450 nm feature is absent. Finally, for illustration purposes, we scale the resultant spectrum to approximate the known continuum level of Europa's leading hemisphere using ground-based data over the same wavelength range (Spencer et al., 1995; McFadden et al., 1980). The result is shown in Figure 1B. To place a conservative upper limit on the presence of a 720 nm absorption, we fit a third-order polynomial continuum between 600 and 870 nm, excluding the range anticipated for the M-center absorption (640 – 830 nm). We then remove this continuum and display the result beneath the spectrum in Figure 1B. We estimate an upper limit of a 0.5% band strength based on qualitative uncertainties in the continuum shape.

References

Anderson, J. D. et al. (1998). "Europa's differentiated internal structure: Inferences from four Galileo encounters". *Science* 281.5385, pp. 2019–2022.

ASTM (2000). "2000 ASTM Standard Extraterrestrial Spectrum Reference E-490-00." *Natl. Renew. Energy Lab*, pp. 155–159.

Brown, M. E. and K. P. Hand (2013). "Salts and Radiation Products on the Surface of Europa". *The Astronomical Journal* 145.4, p. 110.

Carlson, R. W., R. E. Johnson, and M. S. Anderson (1999). "Sulfuric Acid on Europa and the Radiolytic Sulfur Cycle". *Science* 286.5437, pp. 97–99.

Carlson, R. W. et al. (2002). "Sulfuric Acid Production on Europa: The Radiolysis of Sulfur in Water Ice". *Icarus* 157.2, pp. 456–463.

Carlson, R. W. et al. (2005). "Distribution of hydrate on Europa: Further evidence for sulfuric acid hydrate". *Icarus* 177.2, pp. 461–471.

Chyba, C. F. and K. P. Hand (2001). "Life without photosynthesis". *Science* 292.5524, pp. 2026–2027.

Collins, G. and F. Nimmo (2009). "Europa". Ed. by R. T. Pappalardo, W. B. McKinnon, and K. Khurana. Tucson, AZ: The University of Arizona Press. Chap. Chaotic Terrain on Europa, pp. 259–282.

Dalton, J. B. (2007). "Linear mixture modeling of Europa's non-ice material based on cryogenic laboratory spectroscopy". *Geophysical Research Letters* 34.21, p. L21205.

Dalton, J. B., J. H. Shirley, and L. W. Kamp (2012). "Europa's icy bright plains and dark linea: Exogenic and endogenic contributions to composition and surface properties". *Journal of Geophysical Research: Planets* 117.E3.

Dalton, J. B. et al. (2005). "Spectral comparison of heavily hydrated salts with disrupted terrains on Europa". *Icarus* 177.2, pp. 472–490.

Dalton, J. B. et al. (2013). "Exogenic controls on sulfuric acid hydrate production at the surface of Europa". *Planetary and Space Science* 77, pp. 45–63.

Doggett, T. et al. (2009). "Europa". Ed. by R. T. Pappalardo, W. B. McKinnon, and K. Khurana. Tucson, AZ: University of Arizona Press. Chap. Geologic Stratigraphy and Evolution of Europa's surface, pp. 137–160.

Fanale, F. P., T. V. Johnson, and D. L. Matson (1974). "Io: A surface evaporite deposit?" *Science* 186.4167, pp. 922–925.

Fanale, F. P. et al. (2001). "An experimental estimate of Europa's "ocean" composition independent of Galileo orbital remote sensing". *Journal of Geophysical Research: Planets* 106.E7, pp. 14595–14600.

Fischer, P. D., M. E. Brown, and K. P. Hand (2015). "Spatially Resolved Spectroscopy of Europa: The Distinct Spectrum of Large-Scale Chaos". *The Astronomical Journal* 150.5, p. 164.

Fischer, P. D. et al. (2017). "Spatially-resolved spectroscopy of Europa's large-scale compositional units at 3-4 microns with Keck NIRSPEC". *The Astronomical Journal* 153.1, p. 13.

Geissler, P. E. et al. (1998). "Evolution of lineaments on Europa: Clues from Galileo multispectral imaging observations". *Icarus* 135.1, pp. 107–126.

Georgiou, E. and C. R Pollock (1989). "Formation of N centers in Pure NaCl". *Physical Review B* 40.9, p. 6321.

Hand, K. P. and R. W. Carlson (2015a). *AAS/Division for Planetary Sciences Meeting Abstracts 47*, p. 405.06.

Hand, K. P. and R. W. Carlson (2015b). "Europa's surface color suggests an ocean rich with sodium chloride". *Geophysical Research Letters* 42.9, pp. 3174–3178.

Hand, K. P. et al. (2009). "Europa". Ed. by R. T. Pappalardo, W. B. McKinnon, and K. Khurana. Tucson, AZ: The University of Arizona Press. Chap. Astrobiology and the Potential for Life on Europa, pp. 589–630.

Hibbitts, C. A. et al. (2019). "Color centers in salts-Evidence for the presence of sulfates on Europa". *Icarus* 326, pp. 37–47.

Kargel, J. S. (1991). "Brine volcanism and the interior structures of asteroids and icy satellites". *Icarus* 94.2, pp. 368–390.

Kargel, J. S. (2000). "Europa's Crust and Ocean: Origin, Composition, and the Prospects for Life". *Icarus* 148.1, pp. 226–265.

Kivelson, M. G. et al. (2000). "Galileo magnetometer measurements: A stronger case for a subsurface ocean at Europa". *Science* 289.5483, pp. 1340–1343.

Mador, I. L. et al. (1954). “Production and bleaching of color centers in x-rayed Alkali halide crystals”. *Physical Review* 96.3, p. 617.

McCord, T. B. et al. (1998). “Salts on Europa’s Surface Detected by Galileo’s Near Infrared Mapping Spectrometer”. *Science* 280.5367, pp. 1242–1245.

McFadden, L. A., J. F. Bell, and T. B. McCord (1980). “Visible spectral reflectance measurements (0.33-1.1 microns) of the Galilean satellites at many orbital phase angles”. *Icarus* 44.2, pp. 410–430.

Nash, D. B. and F. P. Fanale (1977). “Io’s surface composition based on reflectance spectra of sulfur/salt mixtures and proton-irradiation experiments”. *Icarus* 31.1, pp. 40–80.

Nordheim, T. A., K. P. Hand, and C. Paranicas (2018). “Preservation of potential biosignatures in the shallow subsurface of Europa”. *Nature Astronomy* 2.8, p. 673.

O’Brien, D. P., P. Geissler, and R. Greenberg (2002). “A melt-through model for chaos formation on Europa”. *Icarus* 156.1, pp. 152–161.

Paranicas, C., R. W. Carlson, and R. E. Johnson (2001). “Electron bombardment of Europa”. *Geophysical Research Letters* 28.4, pp. 673–676.

Poston, M. J., R. W. Carlson, and K. P. Hand (2017). “Spectral Behavior of Irradiated Chloride Crystals Under Europa-Like Conditions”. *Journal of Geophysical Research: Planets* 122.12, pp. 2644–2654.

Schneider, I. and C. E. Bailey (1969). “Charged F-aggregate centers in NaCl”. *Solid State Communications* 7.9, pp. 657–660.

Schwartz, K. et al. (2008). “Effect of electronic energy loss and irradiation temperature on color-center creation in LiF and NaCl crystals irradiated with swift heavy ions”. *Physical Review B* 78.2, p. 024120.

Seitz, F. (1946). “Color centers in alkali halide crystals”. *Reviews of modern physics* 18.3, p. 384.

Sotin, C., J. W. Head, and G. Tobie (2002). “Europa: Tidal heating of upwelling thermal plumes and the origin of lenticulae and chaos melting”. *Geophysical Research Letters* 29.8, pp. 74–1.

Spencer, J. R., W. M. Calvin, and M. J. Person (1995). “Charge-coupled device spectra of the Galilean satellites: Molecular oxygen on Ganymede”. *Journal of Geophysical Research: Planets* 100.E9, pp. 19049–19056.

Thomas, E. C. et al. (2017). “Composition and evolution of frozen chloride brines under the surface conditions of Europa”. *ACS Earth and Space Chemistry* 1.1, pp. 14–23.

Waite, J. H. et al. (2006). “Cassini ion and neutral mass spectrometer: Enceladus plume composition and structure”. *science* 311.5766, pp. 1419–1422.

Waite, J. H. et al. (2017). “Cassini finds molecular hydrogen in the Enceladus plume: evidence for hydrothermal processes”. *Science* 356.6334, pp. 155–159.

Zimmer, C., K. K. Khurana, and M. G Kivelson (2000). “Subsurface Oceans on Europa and Callisto: Constraints from Galileo Magnetometer Observations”. *Icarus* 147.2, pp. 329–347.

Zolotov, M. Y. and E. L. Shock (2001). “Composition and stability of salts on the surface of Europa and their oceanic origin”. *Journal of Geophysical Research: Planets* 106.E12, pp. 32815–32827.

Chapter 3

ENDOGENIC AND EXOGENIC CONTRIBUTIONS TO VISIBLE-WAVELENGTH SPECTRA OF EUROPA'S TRAILING HEMISPHERE

Trumbo, S. K., M. E. Brown, and K. P. Hand (2020). "Endogenic and exogenic contributions to visible-wavelength spectra of Europa's trailing hemisphere". *The Astronomical Journal* 160.6, p. 282. DOI: 10.3847/1538-3881/abc34c.

ABSTRACT

The composition of Europa's trailing hemisphere reflects the combined influences of endogenous geologic resurfacing and exogenous sulfur radiolysis. Using spatially resolved visible-wavelength spectra of Europa obtained with the Hubble Space Telescope, we map multiple spectral features across the trailing hemisphere and compare their geographies with the distributions of large-scale geology, magnetospheric bombardment, and surface color. Based on such comparisons, we interpret some aspects of our spectra as indicative of purely exogenous sulfur radiolysis products and other aspects as indicative of radiolysis products formed from a mixture of endogenous material and magnetospheric sulfur. The spatial distributions of two of the absorptions seen in our spectra—a widespread downturn toward the near-UV and a distinct feature at 530 nm—appear consistent with sulfur allotropes previously suggested from ground-based spectrophotometry. However, the geographies of two additional features—an absorption feature at 360 nm and the spectral slope at red wavelengths—are more consistent with endogenous material that has been altered by sulfur radiolysis. We suggest irradiated sulfate salts as potential candidates for this material, but we are unable to identify particular species with the available data.

3.1 Introduction

Images of Europa from the *Voyager* and *Galileo* spacecrafts show striking color variations across the surface that exhibit marked hemispherical differences and correlations with surface geology (e.g. Johnson et al., 1983; McEwen, 1986; Buratti and Golombek, 1988; Clark et al., 1998; Fanale et al., 1999). These visible patterns likely reflect the combined influences of endogenous and exogenous sources on the underlying surface composition. A unique association of color with geologic features, such as lineae and heavily disrupted “chaos" terrain (Figure 3.1), pervades the entire surface and hints at the possibility that compositional fingerprints of the internal ocean may persist within recent geology. However, a distinct color contrast between the leading and trailing hemispheres, in which the geologic features of the trailing hemisphere are significantly darker and redder than their leading-hemisphere counterparts (Figure 3.1), appears to reflect the constant exogenous alteration of the trailing-hemisphere surface chemistry via sulfur radiolysis (McEwen, 1986; Nelson et al., 1986; Johnson et al., 1988; Carlson et al., 2009). Sulfur plasma ions from the volcanoes of Io co-rotate with Jupiter’s magnetic field and continuously deposit onto the trailing hemisphere (Pospieszalska and Johnson, 1989; Paranicas et al., 2009), where bombardment by energetic magnetospheric electrons, protons, and ions (Paranicas et al., 2001; Paranicas, 2002; Paranicas et al., 2009) drives a chemically active radiolytic sulfur cycle that affects the underlying composition (Carlson et al., 2002; Carlson et al., 2005). Indeed, continuous lineae that traverse from the trailing to the leading hemisphere appear to change color, becoming less red as they become sheltered from the impinging sulfur plasma (Figure 3.1). Such exogenic processing complicates the interpretation of surface components as oceanic signatures, even within geologic terrain. Disentangling potential endogenous species from radiolytic products is thus critical to understanding the surface composition of Europa and thereby constraining the chemistry of the ocean below.

The imagery implies that visible wavelengths contain compositional information, which may help distinguish endogenic from exogenic influences. Indeed, multiple studies have utilized broadband photometry and spectral ratios from these images to reveal patterns in visible reflectance associated with plasma bombardment and geologic units (McEwen, 1986; Nelson et al., 1986; Johnson et al., 1988; Buratti and Golombek, 1988; Clark et al., 1998; Fanale et al., 1999). However, as neither *Voyager* nor *Galileo* carried a visible-wavelength spectrometer, such studies lacked detailed spectral information that could provide further insight into the compositional differences responsible for the patterns observed.

Until recently, visible spectroscopy of the surface has been limited to disk-integrated observations obtained from the ground (e.g Johnson and McCord, 1970; Johnson, 1970; McFadden et al., 1980; Spencer et al., 1995; Carlson et al., 2009). These spectra echo the leading/trailing albedo and color contrasts seen in imagery and reveal some notable spectral features, including possible absorptions near 360 and 530 nm on the trailing hemisphere and a broad, global downturn toward the near UV (with a band edge at ~500 nm) that is stronger on the trailing hemisphere. However, despite the fact that Europa's surface color shows a clear association with geology, suggesting endogenous influences at visible wavelengths, the features visible in the ground-based spectra have most often been attributed entirely to sulfur allotropes and SO_2 (Spencer et al., 1995; Carlson et al., 2009). Though it was suggested that some sulfur could be endogenic, these species are also anticipated products of the exogenic sulfur implantation (Steudel et al., 1986; Carlson et al., 2002; Carlson et al., 2009), which is indiscriminate of underlying geology.

More recent thinking, however, has considered the possible visible-wavelength contributions of salts related to the internal ocean, which would more plausibly follow disrupted terrain and can become visibly colored due to the formation of radiation-induced defects known as "color centers" (Hand and Carlson, 2015; Poston et al., 2017; Hibbitts et al., 2019). Distinguishing between the potential spectral signatures of salts and sulfur products may be possible with spatially resolved spectroscopy, which can isolate large-scale geologic regions. Indeed, spatially resolved visible-wavelength spectra taken with the Hubble Space Telescope (HST) have already revealed what appears to be a color-center absorption of irradiated sodium chloride (NaCl) at 450 nm on the leading hemisphere, challenging the idea that Europa's surface color and visible spectrum solely reflect sulfur species (Trumbo et al., 2019). The NaCl feature appears exclusively on the leading hemisphere, separate from the trailing-hemisphere sulfur radiolysis, and correlates with surface geology and color, corresponding particularly to Tara Regio, a large, visibly yellow region of chaos terrain (Figure 3.1). NaCl may explain some of the visible patterns on the leading hemisphere, but the species responsible for those on the trailing hemisphere remain uncertain. Here, we use the same HST visible-wavelength dataset to investigate the composition of the trailing hemisphere. We map visible spectral features across the surface and compare their geographic distributions with surface geology, surface color, and particle bombardment patterns in an attempt to distinguish between endogenic and exogenic origins.

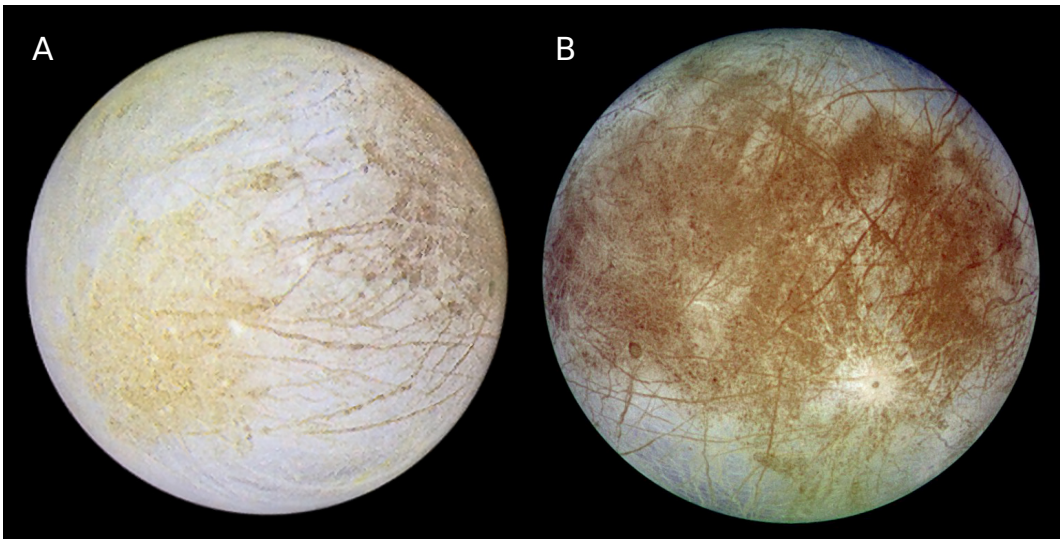

Figure 3.1: *Galileo* SSI color images of approximately the leading (A) and approximately the trailing (B) hemispheres (PIA01295 and PIA00502 in the NASA JPL Photojournal). The actual central longitudes of the images are closer to 45°W and 295°W, respectively. These approximate true-color images were created using the *Galileo* violet, green, and near-infrared (986 nm) filters. Both images show a clear association of color with geologic features, though the geology of the trailing hemisphere appears significantly redder than its more yellow leading-hemisphere counterparts. Individual lineae that traverse from the trailing to the leading hemisphere change color from red to yellow as they leave the sulfur-implantation experienced on the trailing hemisphere. The surface color's simultaneous correlation with geology and dichotomy between the hemispheres suggest that the color may indicate endogenous material on the leading hemisphere and endogenous material altered by sulfur radiolysis on the trailing hemisphere. The large yellow patch in the lower left of the leading-hemisphere image is the large-scale chaos region Tara Regio, where HST spectra detect irradiated NaCl (Trumbo et al., 2019). Image credits: NASA/JPL/University of Arizona.

3.2 Observations and Data Reduction

We observed Europa with the Space Telescope Imaging Spectrograph (STIS) across four HST visits in 2017. The corresponding dates, times, and geometries are listed in Table 3.1. During each visit, we repeatedly stepped the 52″ x 0.1″ slit in 0.06″ increments across the full disk of Europa, resulting in overlapping aperture positions. We executed this slit-scan pattern twice per visit—once each in the G430L and G750L first-order spectroscopy modes (R ~500) to achieve full 300–1000 nm wavelength coverage. At each slit position, we integrated for either 9 (G750L) or 10 seconds (G430L). Flux- and wavelength-calibrated data were then provided by HST after standard reduction with the STIS calibration pipeline (calstis). Using the same

Table 3.1: HST STIS G430L/G750L observations of Europa

Date (UT)	Time (Start/End)	Central Lon.	Central Lat.
2017 May 13	00:20/01:41	224	-3.06
2017 Jun 29	08:19/08:55	25	-2.91
2017 Aug 1	04:43/05:20	133	-2.91
2017 Aug 6	12:27/13:47	314	-2.92

pipeline, but including the calstis defringing procedures, we reprocessed the G750L data to remove substantial fringes from the longest wavelengths. We extracted single spectra by taking individual rows from the two-dimensional spectral images, corresponding to the 0.05″ pixel-scale (~150-km diffraction-limited resolution at 450 nm). We then divided each spectrum by the ASTM E-490 solar reference spectrum (ASTM, 2000) to convert to reflectance.

The G750L data (~550–1000 nm) seemed to contain multiple artifacts, some of which may have been residuals of the defringing process similar to those seen in STIS spectra of Mars (Bell and Antsy, 2007). In addition, significant slit losses and the broad point spread function of STIS distorted the continuum spectral shape in the G750L setting. To correct for these effects, we fit a spline curve to a high-quality ground-based spectrum of the leading hemisphere (Spencer et al., 1995) and extended the fit as a constant beyond the extent of the ground-based spectrum (~775 nm), which is approximately consistent with spectrophotometric measurements at these wavelengths (McFadden et al., 1980). We then multiplied our spectra by the ratio of this curve to a corresponding disk-integrated spectrum constructed from our G750L data. This approach simultaneously divided out global artifacts from the G750L spectra and corrected the continuum shape for slit losses, while preserving relative differences between individual spectra. Finally, to produce continuous 300–1000 nm spectra of the entire surface, we combined the G430L and G750L settings, scaling as appropriate to correct minor flux offsets and smoothing the G430L data to match the G750L signal-to-noise. We calculated the corresponding latitude/longitude coordinates of each extracted pixel using the known phase and angular size of Europa (as obtained from JPL Horizons) and the aperture geometry information included in the HST FITS headers.

3.3 Spectral Maps

Our spectra of the trailing hemisphere (Figure 3.2) show the same strong downturn toward the near UV (with a band edge around 500 nm) that was seen in prior ground-based spectrophotometry, and better spectrally resolve the discrete features near 360 and 530 nm that were more tentatively detected (Johnson and McCord, 1970; Johnson, 1970; McFadden et al., 1980; Carlson et al., 2009). Previously, it was suggested that an assortment of sulfur allotropes could explain all three features, with the 360 and 530 nm absorptions tentatively identified as S_μ (polymeric sulfur) and S_4 (tetrasulfur), respectively, and the broad near-UV downturn most often associated with α-S_8 (orthorhombic cyclo-octal sulfur) (Spencer et al., 1995; Carlson et al., 2009). In one respect, invoking sulfur allotropes to explain the visible spectrum of the trailing hemisphere makes sense due to the sulfur implantation and radiolysis known to be occurring there. However, the imagery clearly implies that some aspects of the visible spectrum must be related to geology, which one would not necessarily expect of radiolysis products composed of pure sulfur. In order to investigate which aspects of our spectra may be endogenous in origin and which can be attributed to exogenous sulfur chemistry, we map the strength of the aforementioned features across the surface and look for correlations with surface color, geology, and radiation bombardment patterns.

To independently measure the strength of the discrete 360 nm absorption and of the larger-scale near-UV downturn on which it is superimposed, we normalize each spectrum to the median reflectance of the 415–425 nm region and fit a linear continuum from 307.5 to 425 nm, excluding the portion corresponding to the discrete absorption (~315–415 nm). We assess each fit by eye and, if necessary, make small changes to these bounds. We take the slope of the fitted continuum as a measure of the magnitude of the near-UV downturn. We then divide out the calculated continuum from each spectrum and integrate the residual absorption to obtain the band area of the 360 nm feature. We take a similar approach to measure the band area of the 530 nm feature, instead using a second-order polynomial continuum between ~480 and 770 nm, excluding the wavelengths of the apparent absorption (~500–700 nm) and making adjustments when necessary to achieve a satisfactory continuum fit. Representative continua are included in Figure 3.2. Finally, we map our measures of all three absorptions across the surface using the geographic coordinates as obtained in Section 3.2. We exclude data near the limb of Europa, as the spectra are of poorer quality, making accurate quantification of spectral features difficult.

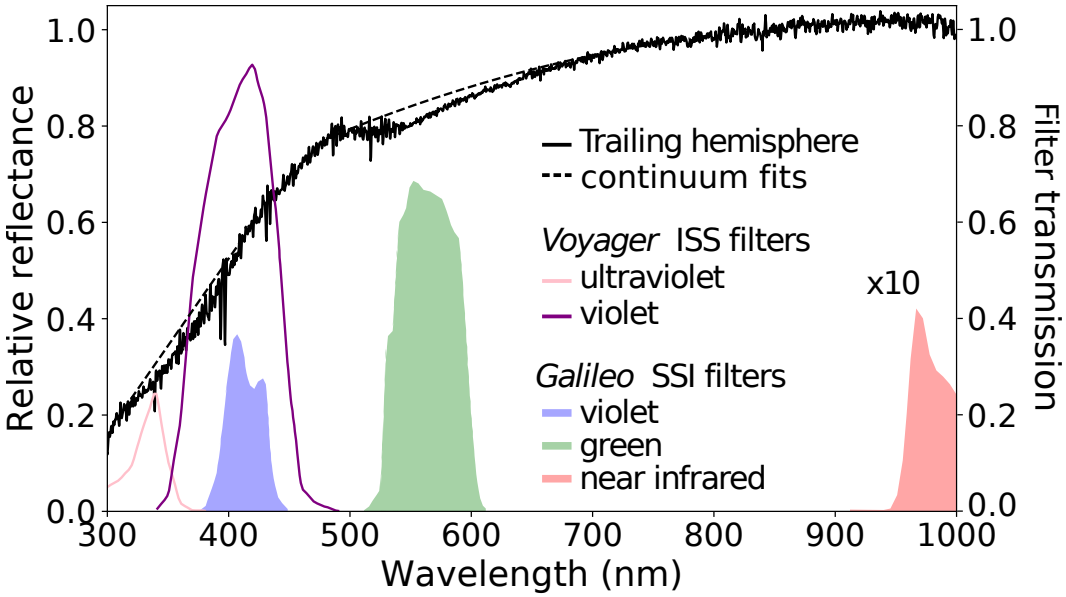

Figure 3.2: Representative spectrum from our HST data of the trailing hemisphere of Europa compared to the *Voyager* and *Galileo* imaging filters. The spectrum is an average from Eastern Annwn Regio and features a strong near-UV downturn with a band edge near 500 nm, as well as two discrete features near 360 and 530 nm. Black dashed lines indicate representative continuum fits akin to those used to map the strength of each feature in our individual spectra. We include the *Voyager* ultraviolet and violet filter responses underneath the spectrum, as well as the *Galileo* filters used to create the images in Figure 3.1. The *Galileo* near-infrared (986 nm) filter response is multiplied by 10 for clarity.

Figure 3.3 shows the results of this mapping compared to the *Voyager* UV/VI ratio map (McEwen, 1986; Carlson et al., 2005; Carlson et al., 2009), which was constructed from images taken in the *Voyager* ultraviolet (UV) and violet (VI) filters. The *Voyager* UV/VI map (Figure 3.3a) has long been interpreted to primarily reflect the effects of exogenous sulfur implantation on the trailing hemisphere, as the large-scale pattern of UV dark material forms an elliptic pattern centered around the trailing point (0°N, 270°W) that largely coincides with the expected patterns of both Iogenic sulfur and electron bombardment (Pospieszalska and Johnson, 1989; Paranicas et al., 2001; Paranicas et al., 2009). Indeed, like the expected sulfur flux, the *Voyager* UV/VI ratio varies roughly as the cosine of the angle from the trailing point, though the relationship is not perfectly linear (Nelson et al., 1986; McEwen, 1986). However, as McEwen (1986) noted, the UV/VI map also features smaller-scale patterns that appear to be endogenic in origin and that precisely associate with geology. In particular, the large-scale chaos regions Dyfed Regio (~250°W) and

Eastern Annwn Regio (~294°W) and the intervening smaller-scale chaos regions appear especially dark in the UV/VI map, but discrete features south of Pwyll Crater (25°S, 271°W) also appear distinct from the background elliptic pattern. In fact, in comparing the *Voyager* ultraviolet and violet filter responses (Danielson et al., 1981) to a representative trailing-hemisphere spectrum (Figure 3.2), we see that the UV/VI ratio simultaneously measures two different things—the large near-UV downturn and the discrete 360 nm feature. Our analysis attempts to separate the two.

Near-UV downturn

We find that mapping the slope across the 315–415 nm region (our proxy for the near-UV downturn) reproduces the large-scale, apparently exogenic pattern of the UV/VI map. With the exception of a few spuriously strong slopes near the northern limbs of each observation, which we believe are pixel-dependent artifacts, the slopes on the trailing hemisphere follow a largely uniform and symmetric elliptic distribution centered on the trailing point and tapering toward the sub- and anti-Jovian points (Figure 3.3b). Again, this pattern is largely consistent with the expected geographies of sulfur implantation and electron bombardment on the trailing hemisphere (Pospieszalska and Johnson, 1989; Paranicas et al., 2001; Paranicas et al., 2009), suggesting an exogenic origin for the near-UV downturn. It is worth noting, however, that this slope is not a perfect measure of the near-UV downturn everywhere across the surface, as it is disrupted by the 450 nm NaCl absorption on the leading hemisphere (Trumbo et al., 2019). Indeed, the NaCl feature, which falls partly within the *Voyager* violet filter and is strongest in the large-scale chaos region Tara Regio (10°S, 75°W), explains much of the red "UV-bright" material in the *Voyager* UV/VI map and results in a depressed slope by our measure. In reality, this region also exhibits an overall drop in reflectance toward the near-UV that is comparable to that of the immediately surrounding terrain. In fact, though the near-UV downturn is strongest on the trailing hemisphere, all of our spectra exhibit a downturn toward the near UV, and the presence of an absorption edge at ~500 nm appears to be a truly global characteristic that is independent of terrain type. Thus, while the strong near-UV downturn on the trailing hemisphere certainly appears to result from the exogenous sulfur chemistry, potentially reflecting the previously suggested sulfur allotrope α-S_8 or some combination of sulfur allotropes that absorb strongly in the UV, alternative explanations may be worth considering for the weaker near-UV downturn observed elsewhere. Indeed, the near ubiquitous presence of an

absorption edge near 500 nm on the other icy Galilean satellites (Spencer et al., 1995) as well as on the icy Saturnian satellites (Hendrix et al., 2018) supports this idea. Radiation-processed organics are invoked to explain the near-UV downturn on the Saturnian satellites (Hendrix et al., 2018). However, limited laboratory data have suggested that radiation-damaged water ice could exhibit a similar near-UV downturn (Sack et al., 1991), which perhaps presents an alternative explanation for the leading hemisphere and icy regions of Europa, as there is currently no evidence for widespread organics at other wavelengths.

360 nm feature

Our map of the discrete 360 nm band (Figure 3.3c) reveals a more irregular and spatially localized pattern that is strongest near the trailing point, but that does not fill the entire elliptic pattern of exogenous alteration. Instead, the geographic distribution of the 360 nm feature appears to correspond to the same geology as the endogenic patterns visible in the *Voyager* UV/VI map, but simply mapped at the coarser spatial resolution of our HST data. Like the lowest *Voyager* UV/VI ratios, the strongest 360 nm absorptions appear associated with Dyfed Regio, Eastern Annwn Regio, and the intervening smaller-scale chaos terrain, with more moderate strengths south of Pwyll Crater. In fact, as the UV/VI ratio is necessarily decreased by the presence of the 360 nm feature, we can say with some certainty that our map of the 360 nm band strength reflects the same geologic regions. Indeed, applying the HST point spread function and pixel scale to a starting distribution corresponding to the lowest ratios in the Voyager map produces a pattern very similar to the geography of the 360 nm feature that we observe.

The association with geologically young chaos terrain implies that the 360 nm feature reflects endogenous influences on the surface composition. However, its confinement to the sulfur-bombarded trailing hemisphere simultaneously suggests that it is related to the exogenous sulfur radiolysis occurring there. Indeed, the fact that the 360 nm absorption is not equally strong within all trailing-hemisphere chaos terrain, but is instead concentrated within that closest to the trailing point, suggests that it may depend heavily on the impinging sulfur flux. All together, this geography is suggestive of an endogenous material that has been compositionally altered by sulfur radiolysis. Previously, the 360 nm absorption was tentatively attributed to the pure sulfur allotrope S_μ (Carlson et al., 2009). However, as S_μ can likely result solely from the radiolysis of implanted Iogenic sulfur (Steudel et al., 1986; Carlson et al., 2009), requiring no endogenous input, there is no obvious reason to expect

a correlation with chaos terrain. Thus, while it is conceivable that there may be unknown effects acting to concentrate or enhance the stability of S_μ within chaos regions, it is worth reevaluating the cause of the 360 nm feature and considering species that are not pure sulfur, but that instead form radiolytically from a mixture of Iogenic sulfur and endogenic materials.

530 nm feature

The 530 nm absorption proved more difficult to quantify, as it falls at the junction between the G430L and G750L settings and very near the ~500 nm band edge of the near-UV downturn. Thus, the measurement of this feature was somewhat sensitive to slight slope and flux mismatches between settings, particularly at the limbs, as well as to changes in the near-UV absorption edge. As a result, our map of the 530 nm absorption is less certain, though mapping with different polynomial continua and fitting parameters consistently produces qualitatively similar geographies. We estimate the pixel-by-pixel uncertainty to be less than 1.5 nm of band area on average.

The distribution we obtain (Figure 3.3d) is similar to that of the 360 nm feature in that it also displays the strongest absorptions near the trailing point and does not fill the entire exogenic alteration pattern. However, without a corresponding high-spatial-resolution imaging map sensitive to the 530 nm absorption, it is difficult to evaluate any potential correlation with the chaos terrain containing the 360 nm feature. Indeed, while such a correlation seems plausible from our map, the observed distribution of the 530 nm feature is also largely consistent with a simple concentration nearest the trailing point, which receives the highest sulfur flux. Thus, though it is possible that the 530 nm absorption also results from radiolytically altered endogenous material, its previous identification as S_4 is equally consistent with our data.

Correlations with visible color

Though the strong near-UV downturn is widespread on the trailing hemisphere and at least the 360 nm feature correlates with some trailing hemisphere chaos terrain, none of the spectral features we have investigated thus far consistently correspond to the red color that appears common to all geology across the trailing hemisphere (Figure 3.1). The near-UV elliptic pattern overprints much of the underlying geologic features, but is significantly more uniform and more symmetric about the trailing point than is the visibly red large-scale geology, which is asymmetric and offset west from the apex. In contrast, the 360 nm feature does associate specifically with

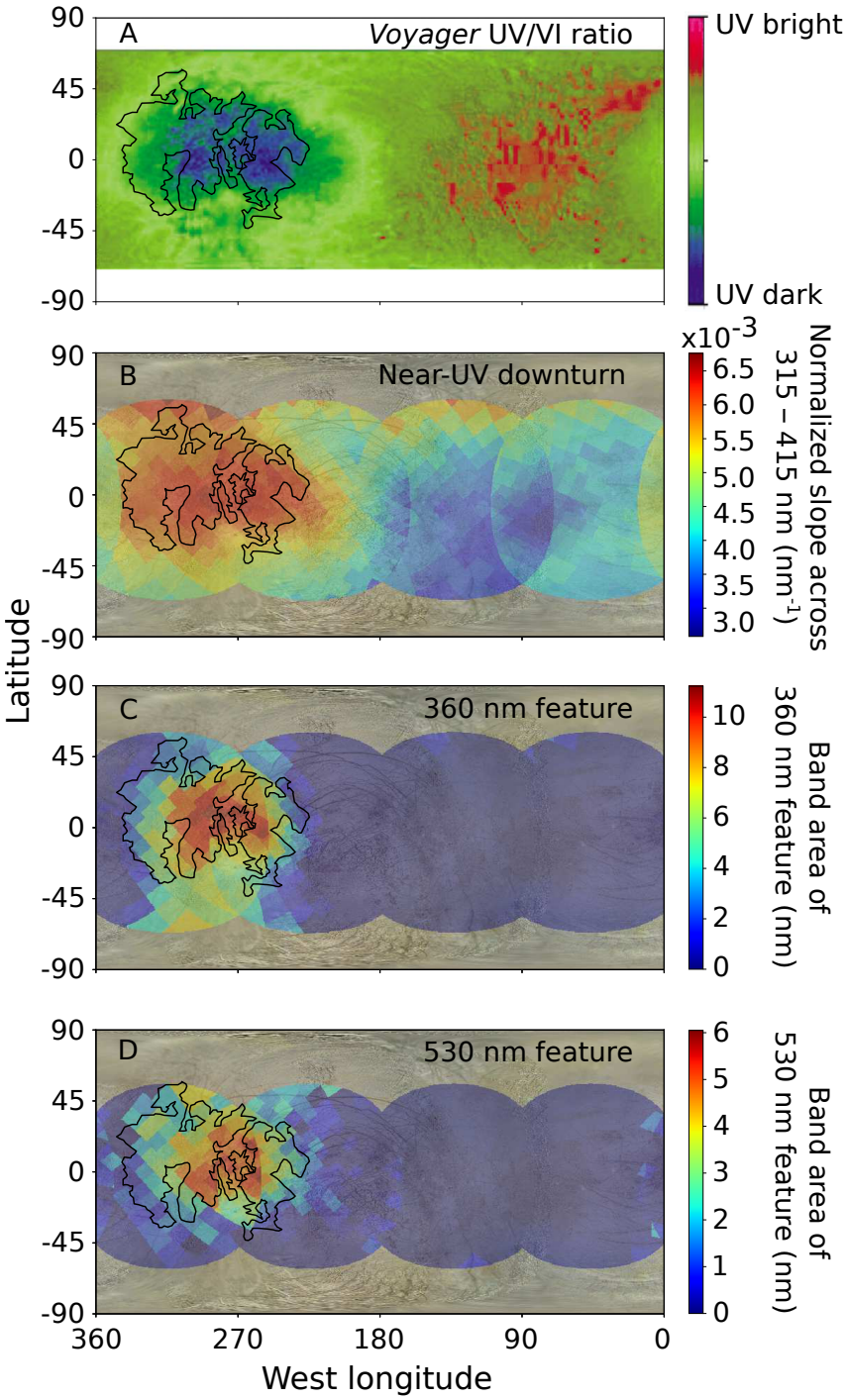

Figure 3.3: (A) *Voyager* UV/VI ratio map adapted from Carlson et al. (2005), but originally produced by McEwen (1986). The large-scale elliptic pattern of UV-dark material on the trailing hemisphere likely reflects the exogenous sulfur chemistry occurring there. However, the UV/VI ratio also displays smaller-scale patterns associated with the large-scale chaos regions Dyfed Regio and Eastern Annwn Regio, the smaller-scale chaos terrain between them, and some apparent geology south of Pwyll Crater. Black outlines indicate the chaos terrain mentioned and are adapted from Doggett et al. (2009). (continued below)

Figure 3.3: (continued) The responses of the *Voyager* ultraviolet and violet filters used to create this map are included in Figure 3.2. (B) Map of the slope from 307.5 to 425 nm (our proxy for the near-UV downturn) in our HST spectra, which reproduces the large-scale, exogenic pattern of the UV/VI map. This distribution suggests that the near-UV downturn reflects exogenous influences. (C) Map of the 360 nm band strength in our HST spectra, which resembles the smaller-scale, apparently endogenic portions of the *Voyager* UV/VI map. This geography is suggestive of a combination of endogenic and exogenic influences. (D) Map of the 530 nm band strength in our HST spectra, which may be consistent with either an association with geology near the trailing point or with a simple dependence on the highest sulfur fluxes.

some of this geology, particularly Dyfed Regio and the eastern portion of Annwn Regio nearest the trailing point, but it is much weaker within the western portions of Annwn Regio, which are similarly red in color to their eastern counterparts. The 530 nm absorption is equally constrained to the most central portions of the trailing hemisphere. Thus, while all three features necessarily influence the colors visible in the *Voyager* and *Galileo* imagery, none appear to be an underlying commonality specifically associated with the widespread red material.

Instead, the aspect of our spectra that we find corresponds best geographically to the red material in the imagery is the slope in the 700 nm region. This slope appears to result from a broad absorption that extends through the red wavelengths before interfering with the 530 nm feature. As a proxy for its strength, we normalize our spectra to the median reflectance between 745 and 750 nm, linearly fit the data between 650 and 750 nm, and then map the resulting slopes across the surface. Figure 3.4 shows the result of this mapping compared to an approximate true-color mosaic of Europa demonstrating the extent and locations of reddish material on the surface (image credit: NASA / JPL / Björn Jónsson). Unlike any of the spectral maps discussed above, our map of this absorption seems uniquely correlated with all of the visibly red large-scale chaos terrain on the trailing hemisphere, highlighting not just Dyfed Regio and the eastern portions of Annwn Regio, but also the western portions of Annwn Regio, which extend across the sub-Jovian point. In fact, the absorption even appears weakly within the less-red large-scale chaos terrain near the anti-Jovian point. However, like the red color visible in imagery, this feature is absent from the chaos terrain on the leading hemisphere, which is sheltered from the trailing-hemisphere sulfur implantation and the resultant sulfur radiolytic chemistry.

Our map may reflect the same absorber as does the incomplete *Galileo* NIMS 0.7/1.2

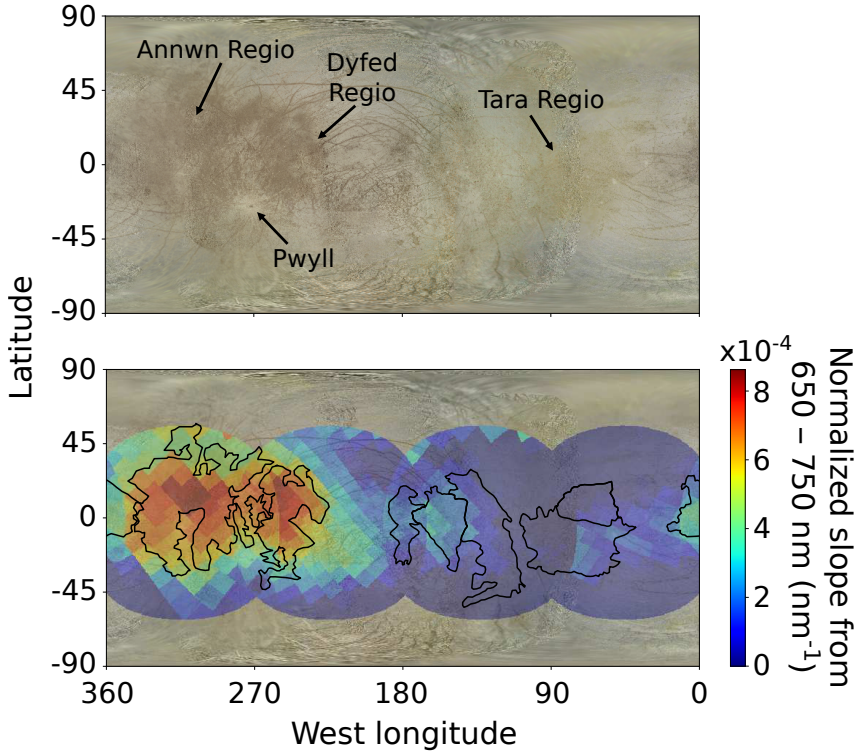

Figure 3.4: Map of the spectral slope from 650 to 750 nm compared to an approximate true-color mosaic of Europa's surface (image credit: NASA / JPL / Björn Jónsson). This slope acts as a measure of the broad absorption feature visible across the red wavelengths and corresponds well to the reddish material visible in the imagery. Our map of this slope highlights all of the large-scale trailing-hemisphere chaos terrain and even the less-red chaos regions near the sub- and anti-Jovian points to a lesser extent (black chaos outlines are adapted from Doggett et al. (2009)). As the broad absorption across the red wavelengths appears common to all of the large-scale geology experiencing sulfur radiolysis, it likely reflects species formed via the radiolysis of a mixture of endogenic material and implanted Iogenic sulfur.

μm ratio map published previously, which highlighted some of the same regions (Carlson et al., 2005). Like the ground-based spectra, the NIMS map was interpreted to most likely reflect pure sulfur chains or polymers, potentially produced as part of the radiolytic sulfur cycle on the trailing hemisphere. However, as the absorber and the reddish color with which it correlates appear so specifically associated with geologic features, we suggest that a radiolytically altered endogenous material better explains the observed geography. We discuss possible candidates in the next section.

3.4 Discussion: potential compositions

The HST spectra of Europa's trailing hemisphere appear to reflect both endogenous and exogenous influences on the surface composition. The implantation and subsequent radiolysis of sulfur from Io almost certainly results in the formation of sulfur allotropes, such as S_8 and S_4 (Steudel et al., 1986; Carlson et al., 2002; Carlson et al., 2009), which will affect the visible spectrum and may explain the strong near-UV downturn and 530 nm feature we observe on the trailing hemisphere. Indeed, these two species have been invoked to explain similar absorption features on Io (Spencer et al., 2004; Carlson et al., 2009). However, Europa's simultaneous global association of color with geology and dichotomy of color between the leading and trailing hemispheres seems to suggest the presence of endogenous material that has been chemically altered by the exogenous sulfur radiolysis. The geographies of the 360 nm feature and of the 700 nm slope in our spectra appear most consistent with species that are radiolytically produced from a mixture of Iogenic sulfur and endogenic material. Salts from the internal ocean, which have long been considered as likely components of Europa's surface (e.g McCord et al., 1998; McCord et al., 1999; Dalton, 2007; Dalton et al., 2012; Hanley et al., 2014; Shirley et al., 2016), are perhaps the most obvious candidates for the endogenic starting material. Though the nature of such salts is still debated, recent work utilizing spatially resolved ground-based near-infrared spectra has suggested that chlorides may dominate Europa's endogenic surface salts (Brown and Hand, 2013; Fischer et al., 2015; Fischer et al., 2017; Ligier et al., 2016). Specifically, Brown and Hand (2013) proposed a conceptual model in which these hypothesized chlorides participate in the radiolytic sulfur cycle on the trailing hemisphere and convert to sulfates when irradiated in the presence of Iogenic sulfur. In this picture, endogenic chloride-rich material would persist within geologic terrain on the leading hemisphere, where it is sheltered from the incoming sulfur plasma, but become progressively altered to a more sulfate-rich composition within those terrains subjected to the sulfur radiolysis on the trailing hemisphere. It should be noted that this hypothesis differs from that of Ligier et al. (2016), who also hypothesized the presence of chlorinated salts using a similar near-infrared dataset to that of Brown and Hand (2013), but instead interpreted their data to reflect magnesium-bearing chlorinated salts within the chaos terrain of the trailing hemisphere. However, the compositions suggested by Ligier et al. (2016) result from the linear mixture modeling of largely featureless continua, rather than from the detection of distinct, compositionally diagnostic absorption features, which is necessary to unambiguously identify surface species. Indeed, the recent

HST detection of a 450 nm absorption indicative of irradiated NaCl within large-scale chaos regions on the leading hemisphere (Trumbo et al., 2019) represents the only unambiguous detection of chlorinated salts on Europa to date and is consistent with the conceptual view laid out by Brown and Hand (2013). Thus, sulfate salts may represent a likely candidate for the altered endogenous material implied by the visible-wavelength data of the trailing hemisphere.

Though many candidate sulfate salts are typically white at visible wavelengths, like NaCl, they can become significantly discolored when subjected to radiation conditions like those at the surface of Europa (Nash and Fanale, 1977; Hibbitts et al., 2019). In fact, Hibbitts et al. (2019) recently proposed that irradiated sulfate salts may explain the ground-based disk-integrated spectrophotometry of the trailing hemisphere. Specifically, Hibbitts et al. (2019) noted that irradiated $MgSO_4$, a species already suggested from the infrared spectra of Brown and Hand (2013), provides a decent fit to the overall shape of the trailing hemisphere spectrum in the visible, while salts that form broad color-center absorptions near 600 nm could contribute to the apparent broad absorption beyond 500 nm, which we have shown to be a convolution of the 530 nm feature and a wider absorption spanning the red wavelengths.

Figure 3.5 compares an average spectrum of Eastern Annwn Regio to some of these proposed irradiated sulfate salts and to select irradiated chloride salts, as well as to the sulfur allotropes discussed in the previous section. Like the spectrum of Eastern Annwn Regio, that of irradiated $MgSO_4$ also exhibits a pronounced near-UV downturn. Thus, it is possible that $MgSO_4$ may contribute to the strong near-UV downturn we find on the trailing hemisphere, though sulfur allotropes almost certainly contribute as well and are likely required to explain the elliptic distribution we observe (Figure 3.3b). Both irradiated KCl and S_4 exhibit absorptions nearby in wavelength to the 530 nm feature we observe on Europa. However, S_4 provides a more satisfactory explanation, both in terms of the wavelength of the band minimum (Figure 3.5) and in terms of the geographic distribution (Figure 3.3d), as one would expect KCl to be spatially associated with the previously observed NaCl on the leading hemisphere (Trumbo et al., 2019). Though sulfur allotropes may be implicated for the near-UV downturn and perhaps the 530 nm absorption, color-center absorptions by irradiated sulfate salts similar to the shown Na_2SO_4 or $Na_2Mg(SO_4)_2 \cdot 4H_2O$ (bloedite) may better explain the broad absorption causing the observed spectral slope at 700 nm (Figure 3.4), which maps to the reddish material

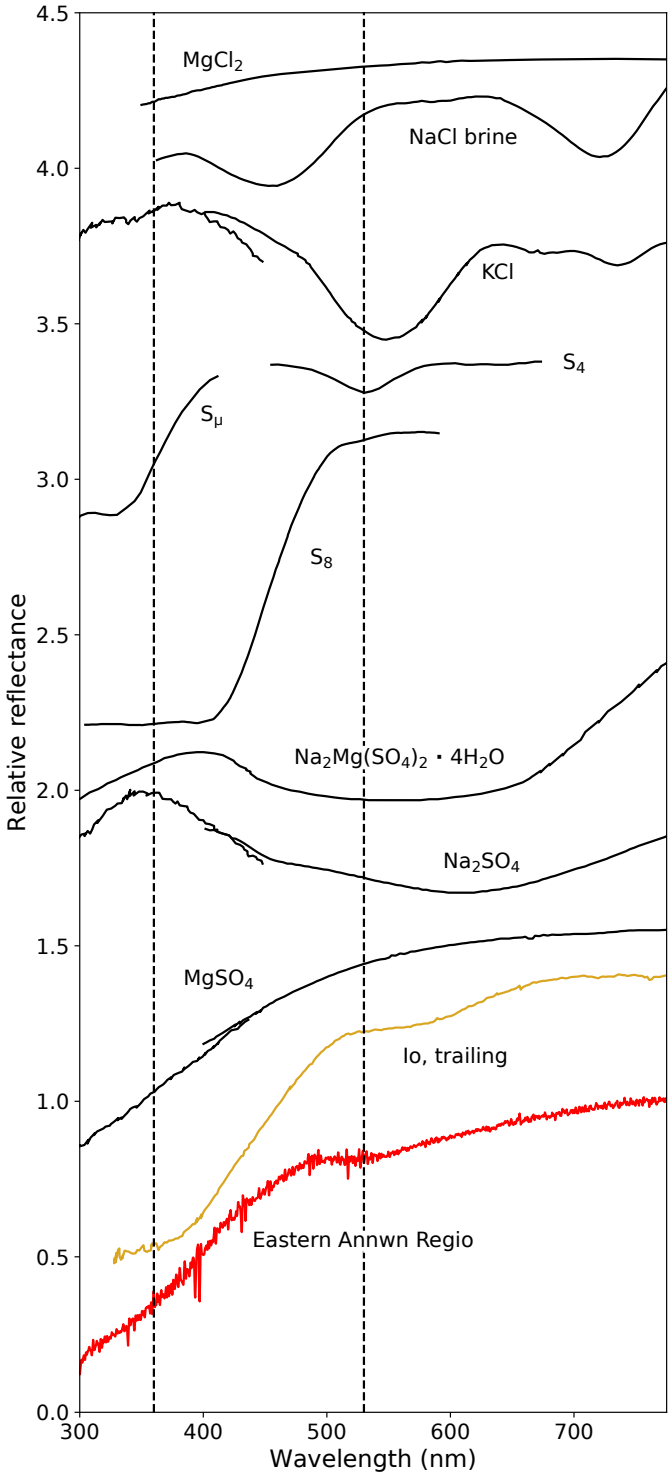

Figure 3.5: Average spectrum of Eastern Annwn Regio compared to the spectra of multiple sulfur allotropes, select irradiated sulfate and chloride salts, and the trailing hemisphere of Io. Vertical dashed lines indicate the approximate wavelengths of the band minima for the 360 and 530 nm absorptions on Europa. (continued below)

Figure 3.5: (continued) With the exception of the S_μ and S_4 spectra, which are scaled arbitrarily for clarity, all of the spectra are scaled to unity at their longest wavelengths and offset vertically from each other. The spectra of the sulfur allotropes are adapted from Carlson et al. (2009), the $Na_2Mg(SO_4)_2 \cdot 4H_2O$ (bloedite) spectrum is taken from Nash and Fanale (1977), the Na_2SO_4, $MgSO_4$, and KCl spectra are from Hibbitts et al. (2019), the NaCl brine spectrum is from Hand and Carlson (2015), the $MgCl_2$ spectrum is taken from the supplementary materials of Trumbo et al. (2019), and the Io spectrum is from Spencer et al. (1995). With the exception of the S_μ spectrum, all of the spectra shown represent irradiated samples. The $Na_2Mg(SO_4)_2 \cdot 4H_2O$ (bloedite) spectrum shows a proton-irradiated sample, the remaining salt spectra show electron-irradiated samples, and the S_4 and S_8 spectra are of UV-irradiated samples. With the exception of the NaCl brine spectrum, which was taken at 100 K, and the S_8 and S_4 spectra, which were obtained at 77 K, all of the shown laboratory spectra were obtained at room temperature.

visible in imagery. However, these laboratory spectra bear little resemblance to the Europa spectrum beyond both exhibiting broad features across the red wavelengths. Thus, a conclusive correspondence between sulfate color centers and the Europa spectra is by no means implied from the available data. In fact, it is impossible to either identify or rule out any of the sulfates shown, due to the broad nature of their absorption features, the interference of multiple features within the Europa spectra, and the limitations of the laboratory data, which were obtained at room temperature using unrealistically high radiation fluxes. Furthermore, though our observed geography of the 360 nm feature on Europa suggests that it too results from altered endogenous material, none of the examined laboratory spectra provide a satisfactory explanation for this absorption. Thus, while we, in part, agree with Hibbitts et al. (2019) and suggest that irradiated sulfate salts may explain those aspects of the visible Europa spectra that correlate with geologic features on the trailing hemisphere, a better understanding of the surface composition and sulfur radiolysis chemistry and additional laboratory spectra are needed to fully address this hypothesis.

3.5 Conclusions

Utilizing spatially resolved visible-wavelength spectra of Europa from HST, we have examined several absorption features unique to the trailing hemisphere in an attempt to disentangle potential endogenous influences from those of the exogenous radiolytic sulfur chemistry. By comparing the distribution of each absorption with surface color, geology, and radiation bombardment patterns, we differentiate be-

tween features that we interpret to reflect pure-sulfur radiolytic products and those that we interpret to reflect species radiolytically produced from a combination of endogenic material and Iogenic sulfur. Two of the features we observe—a widespread near-UV downturn and a distinct feature at 530 nm—appear consistent with sulfur allotropes, as has been suggested based on previous ground-based data. However, the geographies of the remaining features—a discrete absorption at 360 nm and the spectral slope at red wavelengths—appear to indicate endogenous material altered by sulfur radiolysis. Though we cannot uniquely identify the responsible species with currently available data, we suggest irradiated sulfates produced by the radiolysis of endogenous salts as potential candidates. We suggest that future laboratory experiments examining the sulfur radiolysis of potentially endogenous salts and investigating the spectroscopy of irradiated sulfates at Europa-like temperatures and energy fluxes may provide further insight in to the interpretation of the HST spectra.

References

ASTM (2000). *2000 ASTM Standard Extraterrestrial Spectrum Reference E-490-00*. West Conshohocken, PA.

Bell, J. F. and T. M. Antsy (2007). "High spectral resolution UV to near-IR observations of Mars using HST/STIS". *Icarus* 191.2, pp. 581–602.

Brown, M. E. and K. P. Hand (2013). "Salts and Radiation Products on the Surface of Europa". *The Astronomical Journal* 145.4, p. 110.

Buratti, B. and M. Golombek (1988). "Geologic implications of spectrophotometric measurements of Europa". *Icarus* 75.3, pp. 437–449.

Carlson, R. W. et al. (2002). "Sulfuric Acid Production on Europa: The Radiolysis of Sulfur in Water Ice". *Icarus* 157.2, pp. 456–463.

Carlson, R. W. et al. (2005). "Distribution of hydrate on Europa: Further evidence for sulfuric acid hydrate". *Icarus* 177.2, pp. 461–471.

Carlson, R. W. et al. (2009). "Europa". Ed. by R. T. Pappalardo, W. B. McKinnon, and K. Khurana. Tucson, AZ: The University of Arizona Press. Chap. Europa's Surface Composition, pp. 283–328.

Clark, B. E. et al. (1998). "Multispectral terrain analysis of Europa from Galileo Images". *Icarus* 135.1, pp. 95–106.

Dalton, J. B. (2007). "Linear mixture modeling of Europa's non-ice material based on cryogenic laboratory spectroscopy". *Geophysical Research Letters* 34.21, p. L21205.

Dalton, J. B., J. H. Shirley, and L. W. Kamp (2012). "Europa's icy bright plains and dark linea: Exogenic and endogenic contributions to composition and surface properties". *Journal of Geophysical Research: Planets* 117.E3.

Danielson, G. E. et al. (1981). "Radiometric performance of the Voyager cameras". *Journal of Geophysical Research: Space Physics* 86.A10, pp. 8683–8689.

Doggett, T. et al. (2009). "Europa". Ed. by R. T. Pappalardo, W. B. McKinnon, and K. Khurana. Tucson, AZ: University of Arizona Press. Chap. Geologic Stratigraphy and Evolution of Europa's surface, pp. 137–160.

Fanale, F. P. et al. (1999). "Galileo's Multiinstrument Spectral View of Europa's Surface Composition". *Icarus* 139.2, pp. 179–188.

Fischer, P. D., M. E. Brown, and K. P. Hand (2015). "Spatially Resolved Spectroscopy of Europa: The Distinct Spectrum of Large-Scale Chaos". *The Astronomical Journal* 150.5, p. 164.

Fischer, P. D. et al. (2017). "Spatially-resolved spectroscopy of Europa's large-scale compositional units at 3-4 microns with Keck NIRSPEC". *The Astronomical Journal* 153.1, p. 13.

Hand, K. P. and R. W. Carlson (2015). "Europa's surface color suggests an ocean rich with sodium chloride". *Geophysical Research Letters* 42.9, pp. 3174–3178.

Hanley, J. et al. (2014). "Reflectance spectra of hydrated chlorine salts: The effect of temperature with implications for Europa". *Journal of Geophysical Research: Planets* 119.11, pp. 2370–2377.

Hendrix, A. R. et al. (2018). "Icy Saturnian satellites: Disk-integrated UV-IR characteristics and links to exogenic processes". *Icarus* 300, pp. 103–114.

Hibbitts, C. A. et al. (2019). "Color centers in salts-Evidence for the presence of sulfates on Europa". *Icarus* 326, pp. 37–47.

Johnson, R. E. et al. (1988). "Analysis of Voyager images of Europa: Plasma bombardment". *Icarus* 75.3, pp. 423–436.

Johnson, T. V. (1970). "Albedo and spectral reflectivity of the Galilean satellites of Jupiter". PhD thesis. California Institute of Technology.

Johnson, T. V. and T. B. McCord (1970). "Galilean satellites the spectral reflectivity 0.30-1.10 micron". *Icarus* 13.1, pp. 37–42.

Johnson, T. V. et al. (1983). "Global multispectral mosaics of the icy Galilean satellites". *Journal of Geophysical Research: Solid Earth* 88.B7, pp. 5789–5805.

Ligier, N et al. (2016). "VLT/SINFONI observations of Europa: New insights into the surface composition". *The Astronomical Journal* 151.6, p. 163.

McCord, T. B. et al. (1998). "Salts on Europa's Surface Detected by Galileo's Near Infrared Mapping Spectrometer". *Science* 280.5367, pp. 1242–1245.

McCord, T. B. et al. (1999). "Hydrated salt minerals on Europa's surface from the Galileo near-infrared mapping spectrometer (NIMS) investigation". *Journal of Geophysical Research: Planets* 104.E5, pp. 11827–11851.

McEwen, A. S. (1986). "Exogenic and endogenic albedo and color patterns on Europa". *Journal of Geophysical Research: Solid Earth* 91.B8, pp. 8077–8097.

McFadden, L. A., J. F. Bell, and T. B. McCord (1980). "Visible spectral reflectance measurements (0.33-1.1 microns) of the Galilean satellites at many orbital phase angles". *Icarus* 44.2, pp. 410–430.

Nash, D. B. and F. P. Fanale (1977). "Io's Surface Composition Based on Reflectance Spectra of Sulfur/Salt Mixtures and Proton-Irradiation Experiments". *Icarus* 31.1, pp. 40–80.

Nelson, M. L. et al. (1986). "Europa: Characterization and interpretation of global spectral surface units". *Icarus* 65.1, pp. 129–151.

Paranicas, C. (2002). "The ion environment near Europa and its role in surface energetics". *Geophysical Research Letters* 29.5.

Paranicas, C., R. W. Carlson, and R. E. Johnson (2001). "Electron bombardment of Europa". *Geophysical Research Letters* 28.4, pp. 673–676.

Paranicas, C. et al. (2009). "Europa". Ed. by R. T. Pappalardo, W. B. McKinnon, and K. Khurana. Tucson, AZ: The University of Arizona Press. Chap. Europa's Radiation Environment and its Effects on the Surface, pp. 529–544.

Pospieszalska, M. K. and R. E. Johnson (1989). "Magnetospheric ion bombardment profiles of satellites: Europa and Dione". *Icarus* 78.1, pp. 1–13.

Poston, M. J., R. W. Carlson, and K. P. Hand (2017). "Spectral Behavior of Irradiated Chloride Crystals Under Europa-Like Conditions". *Journal of Geophysical Research: Planets* 122.12, pp. 2644–2654.

Sack, N. J. et al. (1991). "Alteration of the UV-visible reflectance spectra of H_2O ice by ion bombardment". *Journal of Geophysical Research: Planets* 96.E2, pp. 17535–17539.

Shirley, J. H., C. S. Jamieson, and J. B. Dalton (2016). "Europa's surface composition from near-infrared observations: A comparison of results from linear mixture modeling and radiative transfer modeling". *Earth and Space Science* 3.8, pp. 326–344.

Spencer, J. R., W. M. Calvin, and M. J. Person (1995). "Charge-coupled device spectra of the Galilean satellites: Molecular oxygen on Ganymede". *Journal of Geophysical Research: Planets* 100.E9, pp. 19049–19056.

Spencer, J. R. et al. (2004). "Jupiter: Planet, Satellites, and Magnetosphere". Ed. by F. Bagenal, T. E. Dowling, and W. B. McKinnon. Cambridge, UK: Cambridge University Press. Chap. Maps and spectra of Jupiter and the Galilean Satellites, pp. 689–698.

Steudel, R., G. Holdt, and A. T. Young (1986). “On the colors of Jupiter’s satellite Io: Irradiation of solid sulfur at 77 K”. *Journal of Geophysical Research: Solid Earth* 91.B5, pp. 4971–4977.

Trumbo, S. K., M. E. Brown, and K. P. Hand (2019). “Sodium chloride on the surface of Europa”. *Science Advances* 5.6. DOI: 10.1126/sciadv.aaw7123.

Chapter 4

A NEW SPECTRAL FEATURE ON THE TRAILING HEMISPHERE OF EUROPA AT 3.78 μm

Trumbo, S. K. et al. (2017). "A new spectral feature on the trailing hemisphere of Europa at 3.78 microns". *The Astronomical Journal* 153.6, p. 250. DOI: 10.3847/1538-3881/aa6d80.

ABSTRACT

We present hemispherically resolved spectra of the surface of Europa from ~3.1 - 4.13 μm, which we obtained using the near infrared spectrometer NIRSPEC on the Keck II telescope. These include the first high-quality L-band spectra of the surface to extend beyond 4 μm. In our data we identify a previously unseen spectral feature at 3.78 μm on the trailing hemisphere. The longitudinal distribution of the feature is consistent with that of a radiolytic product created by electron or Iogenic ion bombardment. This feature is coincident with an absorption feature of SO_2 frost seen in both laboratory spectra and spectra of Io. However, the corresponding, typically stronger 4.07 μm feature of SO_2 frost is absent from our data. This result is contrary to the suggested detection of SO_2 at 4.05 μm in Galileo NIMS data of the trailing hemisphere, which was severely affected by radiation noise. We use simple spectral modeling to argue that the 3.78 μm feature is not easily explained by the presence of SO_2 frost on the surface. We explore alternative explanations and discuss other potential candidate species.

4.1 Introduction

The surface composition of Europa is of prime interest, because it may ultimately constrain the composition of the ocean below. However, because Europa is located within Jupiter's magnetosphere, its surface is continuously bombarded with energetic charged particles trapped within Jupiter's rapidly rotating magnetic field. These include both high-energy electrons and lower-energy sulfur ions originating from the volcanos of Io (Paranicas et al., 2001; Paranicas, 2002). The resultant interactions drive much of Europa's known surface chemistry by radiolytically processing the surface and creating several new products (e.g. Carlson et al., 2002; Carlson et al., 2005; Paranicas et al., 2009). Europa is tidally locked to Jupiter, and Jupiter rotates much faster than Europa completes its orbit (11.2 hours synodic to Europa vs. Europa's 3.55 day orbital period). Thus, most particles trapped within Jupiter's co-rotating magnetosphere preferentially impact the trailing hemisphere, producing the "bullseye" pattern of radiolytically produced hydrated material observed by Galileo NIMS (Near Infrared Mapping Spectrometer) (e.g. Paranicas et al., 2001; Paranicas et al., 2009; Carlson et al., 2009). Laboratory investigations of radiolytic chemistry in sulfur-water ice mixtures suggest hydrated sulfuric acid as the dominant product, and indeed this species fits the NIMS spectra well (Carlson et al., 1999a; Carlson et al., 2002; Carlson et al., 2005).

To date, much of the compositional information, including that indicative of radiolytic chemistry, has been deduced from NIMS observations (e.g. McCord et al., 1998; McCord et al., 1999; Carlson et al., 2002; Carlson et al., 2005; Carlson et al., 2009; Hansen and McCord, 2008). In addition to the hypothesized trailing hemisphere sulfuric acid (Carlson et al., 1999a), other likely detections include CO_2 at 4.25 μm on both the leading and trailing hemispheres (McCord et al., 1998; Smythe, 1998; Hand et al., 2007; Hansen and McCord, 2008) and H_2O_2 at 3.5 μm on the leading hemisphere (Carlson et al., 1999b). However, observations in the 3–5 μm range of the trailing hemisphere were severely limited by the intense radiation environment at Europa's orbit, and, as a result, the data are of low quality. Recent ground-based observations have provided the best-quality data in this wavelength region. Hand and Brown (2013) presented the first high quality 3–4 μm spectra of Europa's surface, in which H_2O_2 was hemispherically resolved across four nights of observation. These data also revealed a previously unseen feature at 3.78 μm, which is the focus of this paper.

The feature is localized to the trailing hemisphere, which suggests it might be a

Table 4.1: Table of Keck NIRSPEC Observations

Date (UT)	Target	Time Start/End	Airmass Start/End	Longitude Range	Int. Time (s)
2011 Sep 17	Europa	12:45/12:54	1.01/1.01	315 - 316	840
	HD 9866	13:56	1.10		40
2011 Sep 18	Europa	11:47/13:58	1.06/1.02	52 - 62	6240
	HD 9866	11:40	1.02		40
2011 Sep 19	Europa	12:50/13:20	1.01/1.01	158 - 161	1440
	HD 9866	11:25	1.02		40
2011 Sep 20	Europa	11:55/13:57	1.04/1.04	256 - 264	5760
	HD 9866	11:48	1.04		40
2013 Nov 24	Europa	13:03 /15:30	1.00/1.09	245 - 255	3800
	G91-3	13:20/13:34	1.00/1.11		750

radiolytic product produced via bombardment by electrons or Iogenic ions. However, whether the new feature is actually indicative of a previously undetected species or is simply a result of a component already confirmed at other wavelengths, is not immediately clear. Perhaps the most obvious candidate is SO_2 frost, which has a 3.78 μm absorption (e.g. Nash and Betts, 1995) and has been confirmed at UV wavelengths with a trailing hemisphere enhancement (Lane et al., 1981; Noll et al., 1995; Hendrix et al., 1998). SO_2 dominates the 3–4 μm spectrum of Io (e.g. Howell et al., 1989; Nash and Betts, 1995; Carlson et al., 1997) and is an expected product of Iogenic sulfur implantation on Europa (Carlson et al., 2002; Carlson et al., 2005).

The spectrum of SO_2 frost has a much stronger feature at ~4.07 μm, which is beyond the data of Hand and Brown (2013). Hansen and McCord (2008) report a marginal detection of SO_2 at 4.05 μm in NIMS spectra of the trailing hemisphere. These data were taken during distant Europa passes to minimize radiation noise, but they are still of much lower quality than can be achieved from the ground. Furthermore, the reported SO_2 band strengths of up to 40% are inconsistent with the 0.1% average 4.07 μm band strength predicted from the UV detections (Sack et al., 1992; Carlson et al., 2009). The only reported ground-based L-band detection of SO_2 on Europa (Carter et al., 2013) is a result of erroneous observations of the surface of Io and should be disregarded.

To investigate the possibility that the 3.78 μm feature is due to SO_2, we obtained high-quality L-band spectra of the trailing hemisphere from ~3.33–4.13 μm using the near infrared spectrograph NIRSPEC at the W. M. Keck Observatory (McLean et al., 1998). In contrast with the results of Hansen and McCord (2008), the 4.07 μm

feature of SO_2 is not visible in our spectrum. We apply simple spectral models to argue that the 3.78 μm feature is not explained by SO_2 and, thus, is highly indicative of an unidentified radiolytic surface constituent. We discuss potential candidates in Section 4.4.

4.2 Observations and Data Reduction

We observed the trailing hemisphere of Europa on 2013 Nov. 24, using the near-infrared spectrograph NIRSPEC on the KECK II telescope. We used the 42" x 0.57" slit in low-resolution mode (R $\sim$ 2000), covering a wavelength range of $\sim$3.3–4.15 μm in the L-band. At the time of observation, Europa had an angular diameter of 0.97", such that roughly 60% of the disk fit within the slit. For telluric calibration, we observed G91-3, a V = 7.4 G2V star that was $\sim$3.6° away from Europa on the sky. We observed both targets in an ABBA nodding pattern. Each Europa pointing consisted of 100 half-second coadds, and each calibrator pointing consisted of 50 half-second coadds. We also present previously published L-band spectra from Hand and Brown (2013). Details of the corresponding observations and analyses can be found within the referenced paper, although a summary of all observations is presented in Table 4.1.

We performed all new analysis using custom Python codes, following the standard procedures of image rectification, image pair subtraction, residual sky subtraction, and telluric and wavelength calibration. We used the Astropy (Robitaille et al., 2013) and skimage.transform (Walt et al., 2014) packages for image display and rectification, respectively. For wavelength calibration, we used an ATRAN atmospheric transmission spectrum (Lord, 1992). We leave off a small region of data at the long-wavelength end of our spectrum due to excessive thermal background levels. We averaged the spectra over the entire longitude range observed to maximize signal-to-noise.

4.3 Spectral Modeling: SO_2

The hemispherically resolved spectra originally presented in Hand and Brown (2013) are reproduced in Figure 4.1. The 3.78 μm feature is clearly visible in the trailing hemisphere spectrum centered at 260° west longitude and is just visible in the trailing to sub-Jovian spectrum centered at 316° west longitude. However, it is very weak or absent from the leading and leading to anti-Jovian spectra. Figure 4.2 shows our average spectrum of the trailing hemisphere out to 4.13 μm. The data are scaled such that the maximum value is roughly the geometric albedo of the trailing

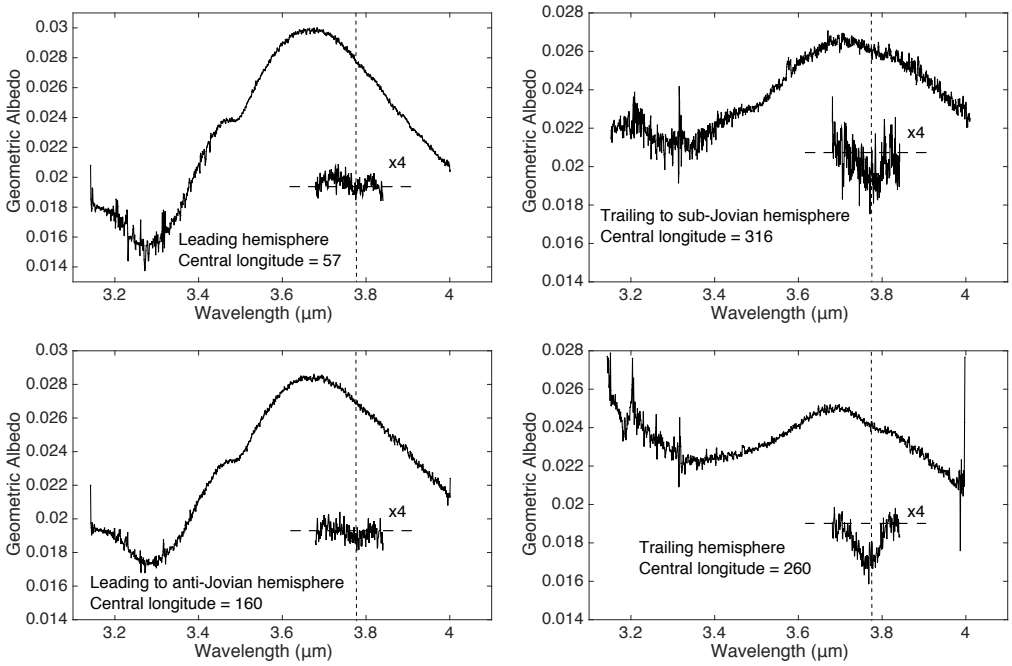

Figure 4.1: Averaged hemispherically resolved spectra of Hand and Brown (2013). Data are normalized to the geometric albedo of the leading hemisphere peak, as measured by NIMS. The central longitude of each spectrum is included. Dotted lines mark the 3.78 μm position. The 3.78 μm feature is most prominent in the trailing hemisphere spectrum.

hemisphere peak, as measured by NIMS. The 3.78 μm feature is again visible, but the 4 μm region is smooth and absent of any visible SO_2 absorptions. As these data are somewhat noisier than the 2011 data of Hand and Brown (2013), we use the latter for all subsequent analyses of the 3.78 μm absorption.

While the 4.07 μm feature of SO_2 frost is typically much deeper than the corresponding 3.78 μm feature, these ratios can change significantly with increasing grain size, as the 4.07 μm feature broadens and saturates. To investigate whether it is possible to simultaneously explain the 3.78 μm feature and the 4 μm region in the Europa spectrum, we used a simple one-component Hapke model (Hapke, 1981) to produce simulated spectra of SO_2 frost for multiple effective particle diameters. Using optical constants from Schmitt et al. (1994), we produced spectra of solid SO_2 at 125 K using effective particle sizes of 10, 100, 1000, and 1500 μm. We then performed continuum subtraction and scaled each spectrum to fit the band area of the observed 3.78 μm absorption. The fit for a 10 μm effective particle diameter is shown in Figure 4.3. While SO_2 does not appear to fit the 3.78 μm feature well, we used the

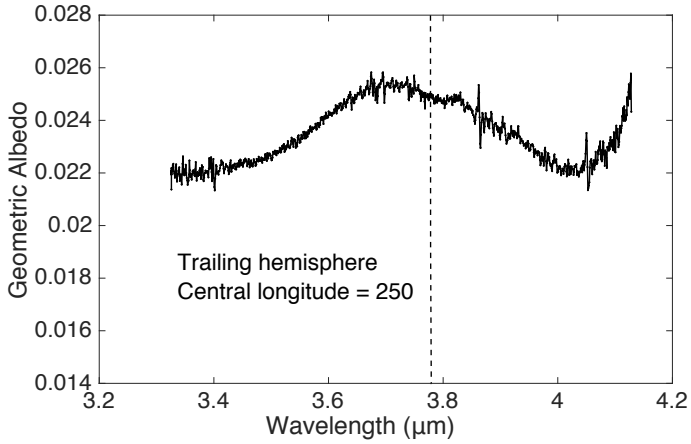

Figure 4.2: Averaged trailing hemisphere spectrum out to 4.13 μm. The data are scaled such that the peak matches the geometric albedo observed by NIMS. The central longitude of the observations is also included. The 3.78 μm feature is clearly visible (indicated by dashed line), but there is no obvious absorption at either 3.56 or 4.07 μm.

resultant mixing ratios to investigate whether the corresponding 4.07 μm features would be visible in our spectrum. However, this comparison is complicated by the fact that our data do not span the entire width of the broad 4.07 μm feature, which extends beyond the edge of the L-band atmospheric transmission window. Because we are lacking data on both sides of the potential feature, we were unable to reliably remove the continuum from our data without making assumptions about its shape. Instead, we linearly mixed the simulated SO_2 spectra with our Europa spectrum in the ratios necessary to explain the observed 3.78 μm feature and assessed the resultant 4 μm regions by eye. The result for a 10 μm effective particle size is shown in Figure 4.4.

At 10 μm, the effect of the 4.07 μm feature is clearly distinguishable from the continuum and would be apparent in our data. At sufficiently large grain sizes, however, the 4.07 μm feature becomes difficult to distinguish from the already dipping Europa continuum in these mixtures. Thus, we do not rule out large SO_2 grain sizes on the basis of the 4 μm region alone. Instead, we use the comparatively small 3.56 μm absorption of SO_2 as a further constraint. For this analysis, we again use the 2011 data of Hand and Brown (2013) due to its superior quality. In the wavelength region of this feature, the Europa continuum is smooth with a high signal-to-noise, allowing for reliable continuum subtraction. Clipping the wavelength region corresponding to the 3.56 μm absorption from our data, we fit

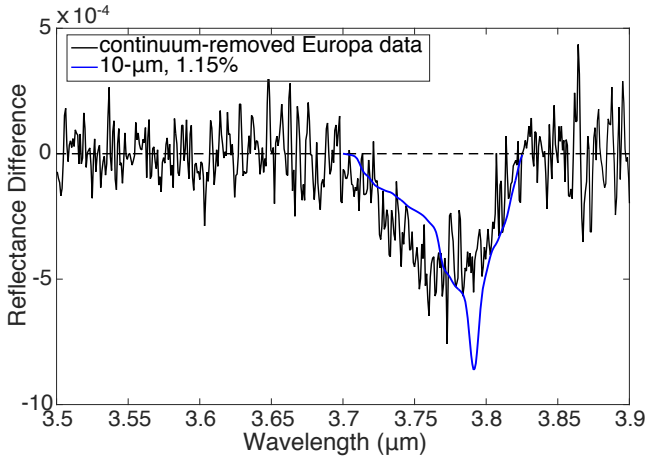

Figure 4.3: The 3.78 μm feature on the trailing hemisphere of Europa after continuum removal. Overlaid is the SO_2 3.78 μm feature corresponding to an effective grain size of 10 μm. It has been scaled to match the band area of our observed absorption feature. The scaling factor is presented in the legend. Continuum removal was performed on the 2011 data of Hand and Brown (2013), because it has the highest signal-to-noise.

a fourth-order polynomial continuum and removed it from our Europa spectrum. Then, scaling the continuum-removed 3.56 μm SO_2 feature by the same factor needed to fit the 3.78 μm feature observed on Europa, we compare the band strengths with our subtracted data (Figure 4.5).

Figure 4.5 suggests that SO_2 should be detectable at 3.56 μm in our data, even for a small effective grain size of 10 μm. Indeed, we can put a 5σ upper limit of a 0.46% mixing ratio, which is two and a half times lower than the 1.15% expected from the strength of the 3.78 μm feature. While the 4.07 μm SO_2 feature becomes difficult to detect in our data at larger grain sizes, the depth of the 3.56 μm feature increases relative to that of the 3.78 μm feature, becoming even more detectable in our data. Conversely, the 4.07 μm feature becomes stronger relative to the 3.78 μm feature at grain sizes below 10 μm. Thus, we are confident that the absence of any detected SO_2 features at 3.56 or 4.07 μm in our data excludes the possibility that the observed 3.78 μm feature is explained by the presence of SO_2 on Europa's surface. SO_2 is a relatively minor product of the radiolytic sulfur cycle on Europa, the two most abundant and stable being H_2SO_4 and sulfur chain polymers (Carlson et al., 2002). Thus, while SO_2 is likely present on the surface of Europa, it is not in high enough abundance to explain the 3.78 μm feature.

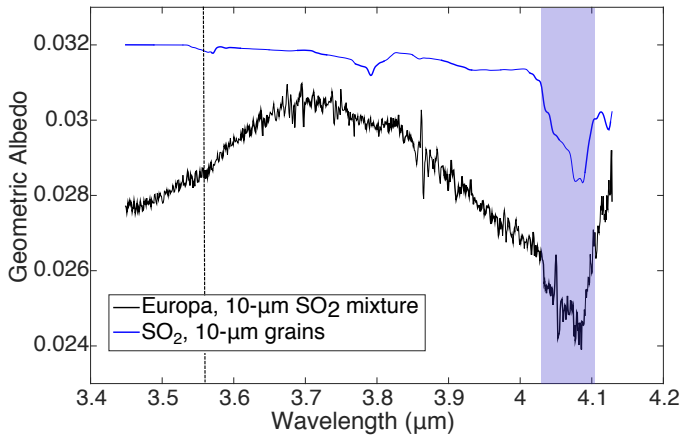

Figure 4.4: Linear mixture of the 2013 trailing hemisphere Europa spectrum with SO_2 at a 10 μm effective grain size is shown in black. The mixing ratio reflects the amount needed to produce the observed 3.78 μm band area. For comparison, a simulated SO_2 spectrum for a 10 μm effective particle size is shown in blue. It has been scaled by the same mixing ratio and arbitrarily shifted along the y-axis. The 4.07 μm feature of SO_2, highlighted in blue, is clearly distinguishable from the continuum shape of the mixture. The location of the 3.56 μm SO_2 feature is indicated by the dashed line. We argue that SO_2 grain sizes less than or equal to 10 μm would produce obvious 4.07 μm features in our data, despite the continuum shape.

4.4 Search for Alternative Candidates

No other confirmed species on the surface of Europa has a 3.78 μm absorption. Therefore, this feature indicates an undiscovered surface constituent. We searched the USGS, ASTER, and NASA Goddard Cosmic Ice spectral libraries, as well as the Nyquist et al. (1997) compilation of IR spectra, for substances with 3.78 μm absorptions. Our search was not only constrained to likely radiolytic products, namely sulfur compounds, but it encompassed several categories of interest for Europa, including sulfates, carbonates, nitrates, phosphates, oxides, and various ices relevant to the study of outer solar system bodies. Of all of the species we looked at, only carbonic acid (H_2CO_3), bloedite ($Na_2Mg(SO_4)_2 \cdot 4H_2O$), and anhydrite ($CaSO_4$) had absorptions near 3.78 μm and lacked strong absorptions at other wavelengths that would have been seen by either NIMS or past ground-based work.

Carbonic acid is a radiolytic product that results from the bombardment of CO_2 and water ice mixtures with energetic electrons (e.g. Brucato et al., 1997; Gerakines et al., 2000; Hand et al., 2007), a process that occurs on the trailing hemisphere of Europa. However, laboratory experiments conducted under Europa-like conditions

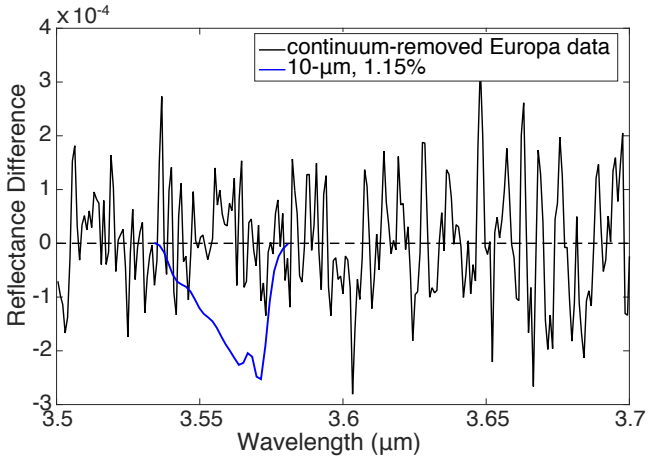

Figure 4.5: Comparison of our continuum-removed Europa spectrum and the continuum-removed 3.56 μm SO_2 feature for an effective grain size of 10 μm. Again, we use the 2011 data of Hand and Brown (2013) due to its superior signal-to-noise. The SO_2 absorption has been scaled by the 1.15% needed to fit the observed area of the 3.78 μm feature. Despite the small grain size and relative weakness of this feature, the absorption would be detected in our data, if it were present.

(Hand et al., 2007) result in a spectral feature that fits our observed feature poorly (Figure 4.6). The carbonic acid feature is broader and shifted by ~0.1 μm toward long wavelengths relative to our detected feature.

Bloedite, a hydrated sodium-magnesium sulfate, has been previously proposed as one of many potential fits to the 1 - 2.5 μm continuum of Europa's surface (e.g. Dalton et al., 2005; Carlson et al., 2009). Its presence, as well as the presence of anhydrite (also a sulfate), would seem to fit with the long-held hypothesis that the ocean is dominated by sulfate salts (e.g. Kargel, 1991; Kargel, 2000; Fanale et al., 2001). However, the confinement of the 3.78 μm feature to the trailing hemisphere would suggest that these sulfates participate in the radiolytic chemistry. One possibility is that they begin as chlorides and convert to sulfates upon sulfur ion bombardment, as suggested in Brown and Hand (2013). However, neither bloedite nor anhydrite provide good fits to the 3.78 μm feature. Our observed feature is narrower than that of bloedite and broader than that of anhydrite. In addition, the features of both bloedite and anhydrite are shifted longward of our observed band center. Both library spectra used, however, were taken at Earth temperatures, so it is possible that the fit quality would change under Europa-like conditions.

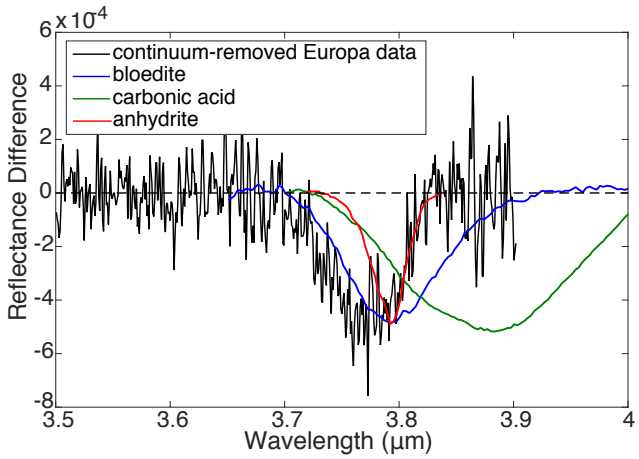

Figure 4.6: Bloedite, carbonic acid, and anhydrite compared to the 3.78 μm feature of Europa (using the 2011 data of Hand and Brown (2013)). The bloedite spectrum is taken from the USGS spectral library (Clark et al., 2007), the anhydrite spectrum is from the ASTER spectral library (Baldridge et al., 2009), and the carbonic acid feature is radiolytically produced from a mixture of CO_2 and water ice at 90 K (Hand et al., 2007). All features were scaled to match the approximate depth of the observed absorption.

4.5 Conclusions

Using ground-based L-band spectroscopy, we have detected a new absorption feature on the trailing hemisphere of Europa at 3.78 μm. The geography of this spectral feature is consistent with that of a radiation product; however it cannot be explained by any known radiolytic species on the surface. SO_2 provides the closest match of known species, but possesses a weak absorption at 3.56 μm and a strong absorption at 4.07 μm, both of which are absent from our data. Thus, we conclude that the 3.78 μm feature represents a new, unidentified surface component. Extensive library searches yielded only three plausible candidates—carbonic acid, bloedite, and anhydrite. With the exception of carbonic acid, the majority of available spectra were taken under Earth conditions, and all provided imperfect fits to the data. Ultimately, we are unable to positively identify the source of the 3.78-μm feature, although there are possible candidates. This highlights the need for more laboratory spectra taken under Europa-like conditions at these wavelengths, particularly of species likely to exist in a different state or mixture than they do on Earth.

References

Baldridge, A. M. et al. (2009). "The ASTER Spectral Library Version 2.0". *Remote Sensing of Environment* 113, pp. 711–715.

Brown, M. E. and K. P. Hand (2013). "Salts and Radiation Products on the Surface of Europa". *The Astronomical Journal* 145.4, p. 110.

Brucato, J. R., M. E. Palumbo, and G. Strazzulla (1997). "Carbonic acid by ion implantation in water/carbon dioxide ice mixtures". *Icarus* 125.1, pp. 135–144.

Carlson, R. W., R. E. Johnson, and M. S. Anderson (1999a). "Sulfuric Acid on Europa and the Radiolytic Sulfur Cycle". *Science* 286.5437, pp. 97–99.

Carlson, R. W. et al. (1997). "The distribution of sulfur dioxide and other infrared absorbers on the surface of Io". *Geophysical Research Letters* 24.20, pp. 2479–2482.

Carlson, R. W. et al. (1999b). "Hydrogen Peroxide on the Surface of Europa". *Science* 283.5410, pp. 2062–2064.

Carlson, R. W. et al. (2002). "Sulfuric Acid Production on Europa: The Radiolysis of Sulfur in Water Ice". *Icarus* 157.2, pp. 456–463.

Carlson, R. W. et al. (2005). "Distribution of hydrate on Europa: Further evidence for sulfuric acid hydrate". *Icarus* 177.2, pp. 461–471.

Carlson, R. W. et al. (2009). "Europa". Ed. by R. T. Pappalardo, W. B. McKinnon, and K. Khurana. Tucson, AZ: The University of Arizona Press. Chap. Europa's Surface Composition, pp. 283–328.

Carter, J. et al. (2013). "Reeconnaissance Compositional Mapping of the Icy Satellites of Jupiter Europa and Ganymede: Early Results". *LPSC*. Vol. 44, p. 1748.

Clark, R. N. et al. (2007). *USGS digital spectral library splib06a: U.S. Geological Survey, Digital Data Series 231*.

Dalton, J. B. et al. (2005). "Spectral comparison of heavily hydrated salts with disrupted terrains on Europa". *Icarus* 177.2, pp. 472–490.

Fanale, F. P. et al. (2001). "An experimental estimate of Europa's "ocean" composition independent of Galileo orbital remote sensing". *Journal of Geophysical Research: Planets* 106.E7, pp. 14595–14600.

Gerakines, P. A., M. H. Moore, and R. L. Hudson (2000). "Carbonic acid production in H_2O: CO_2 ices. UV photolysis vs. proton bombardment". *Astronomy and Astrophysics* 357.793-800.

Hand, K. P. and M. E. Brown (2013). "Keck II Observations of Hemispherical Differences in H_2O_2 on Europa". *The Astrophysical Journal* 766.2, p. L21.

Hand, K. P., R. W. Carlson, and C. F. Chyba (2007). "Energy, chemical disequilibrium, and geological constraints on Europa". *Astrobiology* 7.6, pp. 1006–22. URL: http://www.ncbi.nlm.nih.gov/pubmed/18163875.

Hansen, G. B. and T. B. McCord (2008). "Widespread CO2 and other non-ice compounds on the anti-Jovian and trailing sides of Europa from Galileo/NIMS observations". *Geophysical Research Letters* 35.1.

Hapke, B. (1981). “Bidirectional reflectance spectroscopy: 1. Theory”. *Journal of Geophysical Research: Solid Earth* 86.B4, pp. 3039–3054.

Hendrix, A. R. et al. (1998). “Europa: Disk-resolved ultraviolet measurements using the Galileo ultraviolet spectrometer”. *Icarus* 135.1, pp. 79–94.

Howell, R. R. et al. (1989). “High-resolution infrared spectroscopy of Io and possible surface materials”. *Icarus* 78.1, pp. 27–37.

Kargel, J. S. (1991). “Brine volcanism and the interior structures of asteroids and icy satellites”. *Icarus* 94.2, pp. 368–390.

Kargel, J. S. (2000). “Europa’s Crust and Ocean: Origin, Composition, and the Prospects for Life”. *Icarus* 148.1, pp. 226–265.

Lane, A. L, R. M. Nelson, and D. L Matson (1981). “Evidence for sulphur implantation in Europa’s UV absorption band”. *Nature* 292, pp. 38–39.

Lord, S. D. (1992). *NASA Technical Memorandum 103957*. Ames Research Center, Moffett Field, CA.

McCord, T. B. et al. (1998). “Non-water-ice constituents in the surface material of the icy Galilean satellites from the Galileo near-infrared mapping spectrometer investigation”. *Journal of Geophysical Research: Planets* 103.E4, pp. 8603–8626.

McCord, T. B. et al. (1999). “Hydrated salt minerals on Europa’s surface from the Galileo near-infrared mapping spectrometer (NIMS) investigation”. *Journal of Geophysical Research: Planets* 104.E5, pp. 11827–11851.

McLean, I. S. et al. (1998). “Design and development of NIRSPEC: a near-infrared echelle spectrograph for the Keck II telescope”. *Proc. SPIE* 3354, pp. 566–578.

Nash, D. B. and B. H. Betts (1995). “Laboratory Infrared Spectra (2.3-23 μm) of SO 2 Phases: Applications to Io Surface Analysis”. *Icarus* 117.2, pp. 402–419.

Noll, K. S., H. A. Weaver, and A. M. Gonnella (1995). “The albedo spectrum of Europa from 2200 Å to 3300 Å”. *Journal of Geophysical Research: Planets* 100.E9, pp. 19057–19059.

Nyquist, R. A., C. L. Putzig, and M. A. Leugers (1997). *Infrared and Raman Spectral Atlas of Inorganic Compounds and Organic Salts*. Vol. 3. San Diego, CA: Academic Press.

Paranicas, C. (2002). “The ion environment near Europa and its role in surface energetics”. *Geophysical Research Letters* 29.5.

Paranicas, C., R. W. Carlson, and R. E. Johnson (2001). “Electron bombardment of Europa”. *Geophysical Research Letters* 28.4, pp. 673–676.

Paranicas, C. et al. (2009). “Europa”. Ed. by R. T. Pappalardo, W. B. McKinnon, and K. Khurana. Tucson, AZ: The University of Arizona Press. Chap. Europa’s Radiation Environment and its Effects on the Surface, pp. 529–544.

Robitaille, T. P., E. J. Tollerud, P. Greenfield, et al. (2013). “Astropy Collaboration”. *Astronomy and Astrophysics* 558.A33, p. 9.

Sack, N. J. et al. (1992). “The effect of magnetospheric ion bombardment on the reflectance of Europa’s surface”. *Icarus* 100.2, pp. 534–540.

Schmitt, B. et al. (1994). “Identification of three absorption bands in the 2-μm spectrum of Io”. *Icarus* 111.1, pp. 79–105.

Smythe, W. D. (1998). “Galileo NIMS measurements of the absorption bands at 4.03 and 4.25 microns in distant observations of Europa”. *Bulletin of the American Astronomical Society* 30, p. 1450.

Walt, S. van der et al. (2014). “scikit-image: image processing in Python”. *PeerJ* 2.e453.

Chapter 5

H_2O_2 WITHIN CHAOS TERRAIN ON EUROPA'S LEADING HEMISPHERE

Trumbo, S. K., M. E. Brown, and K. P. Hand (2019). "H_2O_2 within Chaos Terrain on Europa's Leading Hemisphere". *The Astronomical Journal* 158.3, p. 127. DOI: 10.3847/1538-3881/ab380c.

ABSTRACT

Hydrogen peroxide is part of an important radiolytic cycle on Europa and may be a critical source of oxidants to the putative subsurface ocean. The surface geographic distribution of hydrogen peroxide may constrain the processes governing its abundance as well as its potential relevance to the subsurface chemistry. However, maps of Europa's hydrogen peroxide beyond hemispherical averages have never been published. Here, we present spatially resolved L-band (3.16–4 μm) observations of Europa's 3.5 μm hydrogen peroxide absorption, which we obtained using the near-infrared spectrometer NIRSPEC and the adaptive optics system on the Keck II telescope. Using these data, we map the strength of the 3.5 μm absorption across the surface at a nominal spatial resolution of ~300 km. Though previous disk-integrated data seemed consistent with the laboratory expectation that Europa's hydrogen peroxide exists primarily in its coldest and iciest regions, we find nearly the exact opposite at this finer spatial scale. Instead, we observe the largest hydrogen peroxide absorptions at low latitudes on the leading and anti-Jovian hemispheres, correlated with chaos terrain, and relative depletions toward the cold, icy high latitudes. This distribution may reflect the effects of decreased hydrogen peroxide destruction due to efficient electron scavenging by CO_2 within chaos terrain.

5.1 Introduction

The continuous bombardment of Europa's surface by energetic particles within Jupiter's magnetosphere results in extensive radiolytic processing of the surface ice (e.g. Johnson and Quickenden, 1997). The impinging electrons, protons, and ions lead to the dissociation of water molecules, producing OH radicals, which can recombine to produce hydrogen peroxide (H_2O_2) and other oxidants (e.g, Johnson et al., 2003; Cooper et al., 2003; Loeffler et al., 2006). H_2 is lost in the process, creating an increasingly oxidizing surface. Understanding this radiolytic cycle on Europa is not only important in terms of Europa's surface composition and the general study of surface-magnetosphere interactions on icy bodies, but it is also critical for assessing the potential chemical energy sources within Europa's subsurface ocean. Hydrothermal processes at the seafloor may be a source of reductants, but the potential habitability of Europa's ocean will likely depend on a complementary supply of oxidants, such as H_2O_2, from the radiolytically processed surface (Chyba, 2000; Hand et al., 2009).

The geographic distribution of Europa's H_2O_2 may hold clues to the processes controlling its presence on the surface as well as to its potential delivery to the subsurface ocean. The *Galileo* Near Infrared Mapping Spectrometer (NIMS) definitively detected H_2O_2 on the surface via a prominent 3.5 μm absorption in an average spectrum of the leading/anti-Jovian quadrant (Carlson et al., 1999). However, the intense radiation encountered during closer flybys of Europa resulted in poor-quality spectra beyond 3 μm, and no spatially resolved NIMS maps of H_2O_2 were ever published. To date, ground-based spectra, in which the 3.5 μm absorption of H_2O_2 was rotationally resolved across four nights of observation, have provided the best constraints on its geography (Hand and Brown, 2013). These spectra show the largest absorptions on the leading and anti-Jovian hemispheres, in agreement with the NIMS observation, and almost no detectable absorption on the trailing hemisphere. At this scale, Europa's H_2O_2 distribution was easily attributed to the availability of surface water ice and the low surface temperatures associated with Europa's iciest regions, which lie at the mid to high latitudes of the leading and anti-Jovian hemispheres (Brown and Hand, 2013). Water molecules are a necessary precursor for H_2O_2 production, and laboratory experiments studying the production of H_2O_2 via water ice radiolysis (Moore and Hudson, 2000; Loeffler et al., 2006; Zheng et al., 2006; Hand and Carlson, 2011) consistently observe lower equilibrium abundances with increasing temperature, in some cases by nearly a factor of seven across the ~80–120 K temperature range relevant to Europa (Hand and Carlson, 2011).

Table 5.1: Keck NIRSPAO Slit Positions

Date (UT)	Hemisphere	Slit Orientation	Airmass Range	Total Int. Time (min)	Central Longitude	Central Latitude	Telluric Calibrator
2016 Feb 24	trailing/sub-Jovian	E/W	1.10–1.75	120	338 W	1 S	HD 98947
2016 Feb 24	sub-Jovian	N/S	1.03–1.07	100	348 W	2 S	HD 98947
2016 Feb 25	leading	E/W	1.24–1.38	40	79 W	0 N	HD 98947
2016 Feb 25	leading	E/W	1.11–1.18	40	82 W	12 S	HD 98947
2016 Feb 25	leading	N/S	1.04–1.08	40	88 W	2 S	HD 98947
2016 Feb 25	leading	E/W	1.08–1.14	40	95 W	0 N	HD 98947
2018 Jun 06	leading	N/S	1.40–1.42	10	119 W	4 S	HD 128596
2018 Jun 06	leading	N/S	1.36–1.38	10	124 W	4 S	HD 128596
2018 Jun 06	leading/anti-Jovian	N/S	1.24–1.30	20	166 W	3 S	HD 128596
2018 Jun 06	leading/anti-Jovian	N/S	1.22–1.26	20	146 W	3 S	HD 128596
2018 Jun 06	leading/anti-Jovian	N/S	1.25–1.25	10	162 W	3 S	HD 128596
2018 Jun 06	leading	N/S	1.22–1.22	15	115 W	4 S	HD 128596
2018 Jun 06	leading	N/S	1.23–1.25	20	104 W	3 S	HD 128596
2018 Jun 06	leading	N/S	1.26–1.30	20	87 W	3 S	HD 128596
2018 Jun 06	leading	N/S	1.30–1.32	10	120 W	4 S	HD 128596

Considering all of the published observations and laboratory data, one might reasonably expect that higher spatial resolution observations show an abundance of H_2O_2 at the icy high latitudes of Europa's leading and anti-Jovian hemispheres, and relative depletions at the warm equator, which likely contains a significant non-ice fraction in the form of endogenous salt deposits associated with largescale regions of geologically young and highly disrupted chaos terrain (Fischer et al., 2015; Fischer et al., 2017; Trumbo et al., 2019). In order to address this hypothesis, we obtained spatially resolved L-band spectra of Europa's surface, with the goal of mapping the geographic distribution of its 3.5 μm H_2O_2 band.

5.2 Observations and Data Reduction

We observed Europa on Feb. 24th and 25th of 2016 and again on June 6th of 2018 using the near-infrared spectrograph NIRSPEC and the adaptive optics system on the KECK II telescope. We used the 3.92″ x 0.072″ slit in low-resolution mode (R $\sim$ 2000). Our data cover the wavelength range of $\sim$3.16–4 μm in the L-band. As a telluric calibrator for the 2016 observations, we observed HD 98947, a V = 6.9 G5 star that was $\sim$ 1.2° from Europa on the sky. In 2018, we used HD 128596, a V = 7.5 G2 star with a 3.9° separation from Europa. We observed all targets in an ABBA nodding pattern. For our 2016 data, each Europa pointing consisted of 30 20-second coadds, and each calibrator pointing consisted of 15 2-second coadds. In 2018, we reduced the integration times to 30 10-second co-adds for each Europa pointing and 10 2-second coadds for each calibrator pointing.

During both sets of observations, Europa had an angular diameter of nearly 1″, corresponding to $\sim$ 10 $\sim$300-km resolution elements at the diffraction limit of Keck

at 3.5 μm. For each Europa pointing, we aligned the slit in either an E/W or N/S orientation with respect to Europa's north pole. We obtained a corresponding SCAM guide camera image for each exposure as a record of the exact slit positions on the disk. The telescope pointing tended to drift significantly during nods for the 2018 observations. Thus, we used these images in real time to manually maintain a consistent slit position across each ABBA set.

We reduce all data in Python, following the standard methodology of image rectification, image pair subtraction, residual sky subtraction, and telluric and wavelength calibration, utilizing both the Astropy (Robitaille et al., 2013) and skimage.transform (Walt et al., 2014) packages. We use an ATRAN atmospheric transmission spectrum (Lord, 1992) for wavelength calibration. Some of the raw spectral files display readout artifacts, which artificially brighten every 8th pixel in the dispersion direction. Thus, we replace each affected pixel by the average of the two immediately adjacent pixels.

Following this initial data reduction, we extract spectra for individual spatial resolution elements within each slit position. Using the Python Basemap package and the calculated size of Europa in SCAM pixels (0.0168″/pixel), we align the SCAM image corresponding to each NIRSPEC exposure with an orthographic projection and estimate the coordinates of the slit on the disk. Though we made real-time manual corrections to the inaccurate telescope nodding experienced during the 2018 observations, some ABBA sets still exhibited significant position discrepancies between nods. Thus, we align SCAM images and estimate the corresponding slit coordinates for each nod independently. We then locate Europa in the 2D spectral images using its calculated size in NIRSPEC pixels (0.013″/pixel) and extract individual spectra corresponding to an 8-pixel spatial resolution element, stepping by 4 spatial pixels between extractions. We determine the geographic coordinates of each extracted spectrum using the previously obtained slit positions and the aforementioned NIRSPEC pixel scale.

To minimize geographic smearing, while still maximizing the signal-to-noise, we average spectra from overlapping slit positions, as determined by manually inspecting the SCAM images and the extracted coordinates corresponding to each nod. In the case of the trailing/sub-Jovian slits, we tolerate moderate spatial smearing in favor of the enhanced signal-to-noise needed to quantify weak H_2O_2 absorptions. In all cases, we account for any resulting adjustments to the effective slit width and to the geographic area covered by each spectrum. Table 5.1 summarizes our

observations and the geometries of geographically unique slit positions.

5.3 H_2O_2 Mapping

In order to determine the geographic distribution of Europa's 3.5 μm H_2O_2 absorption, we calculate its band area in each individual extracted spectrum. For most spectra, we fit a second-order polynomial from 3.37 to 3.715 μm, excluding the portion corresponding to the H_2O_2 absorption ($\sim$ 3.4–3.65 μm). For the trailing hemisphere observations, we use a third-order polynomial, which better matches the continuum shape. We inspect all fits by eye and, if necessary to achieve a satisfactory continuum fit, make small adjustments to these parameters. We then remove the calculated continuum from each spectrum and integrate the residual absorption to calculate the equivalent width (i.e. the width of a 100% absorption of the same integrated area). We map the resulting band areas using the slit positions and widths obtained as in Section 5.2. Our 2016 data show generally stronger absorptions than do our 2018 data, with maximum band areas ~25% larger than those observed in 2018. This is perhaps unsurprising given that H_2O_2 concentrations on Europa reflect a dynamic equilibrium between constant formation and decay (Hand and Carlson, 2011) that may be influenced by the temporal variability of the radiation environment or of the local surface temperature. Thus, as we are concerned primarily with geographic correlations, we map the 2016 and 2018 slits separately.

Figure 5.1 shows a single mapped slit from our 2016 observations. This slit position crosses both the most spectrally icy location on the surface at ~30° N and 90° W on the leading hemisphere (Brown and Hand, 2013) and the comparatively warm and ice-poor chaos region Tara Regio, making it ideal for testing the hypothesis that Europa's H_2O_2 prefers cold, icy terrain. Puzzlingly, contrary to this hypothesis, the 3.5 μm H_2O_2 absorptions are strongest in exactly the warmest and least icy portion of the slit, nearly perfectly corresponding to the bounds of Tara Regio (mapped approximately from Doggett et al. (2009)). Tara Regio is located at low latitudes, where daytime temperatures approach ~130 K (Spencer et al., 1999), and visible and infrared spectra suggest that it is likely salty in composition (Fischer et al., 2015; Fischer et al., 2017; Trumbo et al., 2019). Yet, its 3.5 μm H_2O_2 band area reaches more than twice that of the most spectrally icy region. Figure 5.1 shows spectra representative of both locations.

The apparent preference of H_2O_2 for low-latitude chaos terrain persists across all of the mapped 2016 slits (Figure 5.2a). Like the N/S slit of Figure 5.1, the leading-

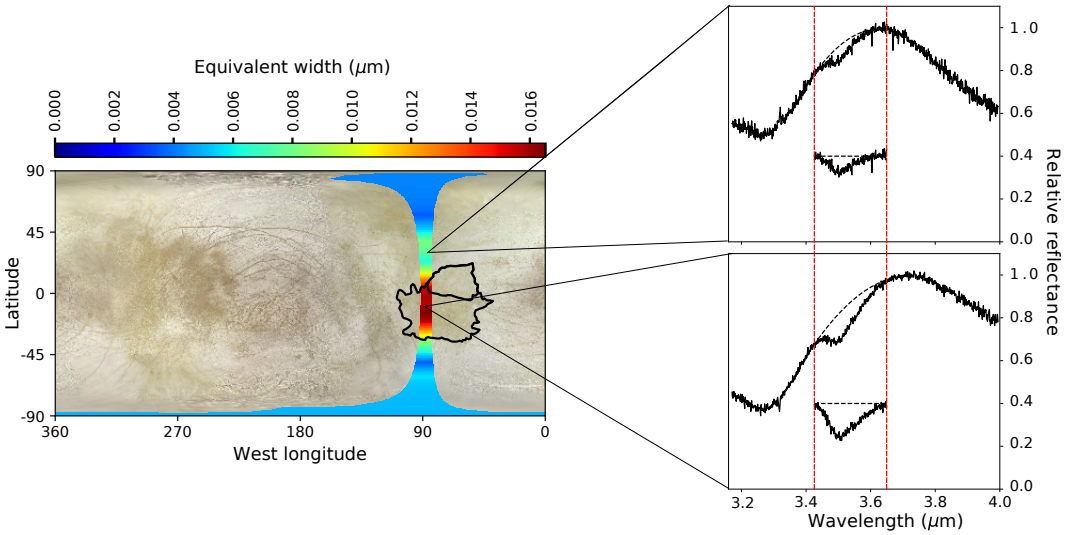

Figure 5.1: A single N/S slit from our 2016 observations, which falls on the leading hemisphere and crosses both the most spectrally icy location on the surface (~ 30° N, 90° W, Brown and Hand, 2013) and the salty, low-latitude chaos region Tara Regio. Contrary to the hypothesis that Europa's H_2O_2 should follow the cold, icy terrain of the upper latitudes, the 3.5 μm band appears anti-correlated with both temperature and ice availability. Instead, the strongest absorptions fall nearly perfectly within the outlined bounds of Tara Regio, with band areas more than twice that of the aforementioned ice-rich region. We show representative spectra from both locations to the right of the map, where the dashed red lines outline the H_2O_2 band. Second-order polynomial continua are indicated by the dashed black curves. We also include the continuum-removed absorptions to ease comparison of the band strengths, although the differences are readily apparent in the spectra themselves. Both spectra are normalized to their individual peaks in the 3.6–3.7 μm region.

hemisphere E/W slit positions also show strong absorptions across Tara Regio. In addition, they demonstrate a marked difference between low-latitude chaos and low-latitude plains terrain, displaying enhanced absorption across the other large-scale chaos regions of the leading/anti-Jovian hemisphere (also mapped approximately from Doggett et al. (2009)), but much weaker band strengths across the ridged plains immediately east of Tara Regio (~30° W). In fact, even the resolution elements that include the narrow space between Tara Regio (~85° W) and eastern Powys Regio (~125° W) appear to exhibit somewhat weakened absorptions on average. The trailing/sub-Jovian regions, by comparison, show only very weak 3.5 μm bands, consistent with the full-disk data of Hand and Brown (2013). However, what little H_2O_2 is present still seems correlated with chaos, as suggested by the slight enhancement near the outlined western-most portion of Annwn Regio (~0° N, 360°

W). We note, however, that accurately quantifying such weak absorptions in this region is difficult, especially given the substantially different continuum shape of spectra from the low-latitudes of the trailing/sub-Jovian hemisphere.

While the 2016 map certainly suggests that Europa's H_2O_2 favors chaos terrain, it is also potentially consistent with a simple preference for low latitudes combined with the known hemispherical trend observed previously in full-disk spectra (Hand and Brown, 2013). In addition, the E/W slits, though approximately constant in latitude, still each cover a range of surface temperatures reflecting the early morning through late afternoon, which may impart unknown diurnal effects onto the longitudinal patterns we observe. To account for these caveats, our 2018 map (Figure 5.2b) is composed of only N/S slit positions. This orientation more concretely differentiates between a preference for low latitudes and a specific correlation with the chaos regions, which are asymmetric about the equator. N/S slits also have the advantage of capturing the latitudes within a given slit position at similar times of the local day, thus minimizing diurnal complications to the observed H_2O_2 pattern within a slit.

Our 2018 dataset confirms the trends suggested by the 2016 map—Europa's H_2O_2 prefers warm, low-latitude, ice-poor chaos terrain to the comparatively cold and ice-rich regions of the upper latitudes. The 2018 N/S slit positions expand our coverage of the large-scale chaos regions of the leading/anti-Jovian hemisphere, and all individual slit positions consistently show the largest 3.5 μm absorptions within the outlined chaos terrain. In most cases, the observed band areas increase sharply near the largescale chaos boundaries, reaching values up to three times as large as those immediately above or below the chaos terrain. In all cases, especially those of Tara Regio and eastern Powys Regio, this requires asymmetric displacement south of the equator, which is inconsistent with a simple preference for low latitudes. In fact, the complete 2018 map indicates that most of Europa's H_2O_2 falls between ~40° S and 20° N, in a latitudinal pattern that possesses similar N/S asymmetries to those of the overall pattern of leading/anti-Jovian chaos terrain. This observed distribution requires dominating influences on Europa's H_2O_2 other than temperature or water ice abundance.

5.4 Discussion

Outside of ice availability and surface temperature, perhaps the most obvious potential factor governing the geographic distribution of H_2O_2 on Europa is the local

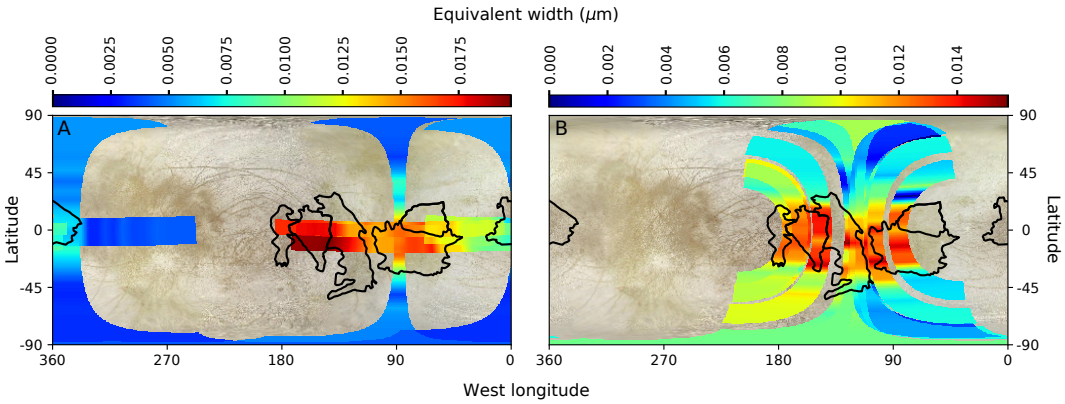

Figure 5.2: All mapped slits from our 2016 (A) and 2018 (B) observations, which demonstrate the spatial distribution of Europa's 3.5 μm H_2O_2 absorption. The deepest absorptions map to low latitudes of the leading and anti-Jovian hemispheres and appear correlated with the geologically young chaos regions (outlined in black). The trailing/sub-Jovian slits, in comparison, display very weak absorptions, consistent with prior full-disk spectra (Hand and Brown, 2013).

radiation environment. Though the entirety of Europa's surface is irradiated by energetic particles, the energy flux and particle composition is geographically nonuniform (Paranicas et al., 2001; Paranicas et al., 2009; Dalton et al., 2013; Nordheim et al., 2018). In fact, the observed H_2O_2 enhancement at low latitudes on the leading hemisphere bears some resemblance to the leading hemisphere "lens" pattern of bombardment by very high-energy ($\gtrsim$ 20 MeV) electrons, which move against the co-rotation direction of Jupiter's magnetic field (Paranicas et al., 2009; Nordheim et al., 2018). This lens centers on the leading hemisphere apex, weakens toward the mid latitudes, and tapers toward the sub- and anti-Jovian points. However, laboratory irradiation experiments have yielded more efficient H_2O_2 production and higher H_2O_2 concentrations using energetic protons and ions (Loeffler et al., 2006) than they have using electrons (Hand and Carlson, 2011). This is due to the higher linear energy transfer (LET) of ions (Loeffler et al., 2006; Hand and Carlson, 2011), which reflects a higher density of resulting excitations and ionizations in the ice. Although H_2O_2 production by 20+ MeV electrons has never been directly studied in the lab, the LET of electrons at these energies is still more than an order of magnitude less than that of the majority of energetic protons and ions striking the surface (Hand and Carlson, 2011). In contrast to the leading hemisphere electrons, energetic protons and ions bombard Europa much more uniformly (Paranicas, 2002; Paranicas et al., 2009) and potentially even favor the high latitudes (Dalton et al., 2013). Indeed, the combined bombardment patterns of energetic ions and $\lesssim$20 MeV electrons, which

primarily impact the trailing hemisphere (Paranicas et al., 2001), result in a relative sheltering of the leading-hemisphere equator in terms of total flux (Paranicas et al., 2009; Dalton et al., 2013). Thus, while the leading hemisphere electron lens may help produce the H_2O_2 at low latitudes, it is unlikely to be the sole explanation. Indeed, because the lens is expected to be symmetric across the equator, it certainly cannot account for the apparent correlation of H_2O_2 with chaos terrain.

The geographic association of H_2O_2 with chaos terrain instead may imply that compositional differences across the surface are a dominating factor in controlling H_2O_2 abundance. Chaos regions are geologically young and extensively disrupted areas of the surface interpreted to reflect recent interaction with subsurface material (e.g Collins and Nimmo, 2009; Schmidt et al., 2011). In fact, leading-hemisphere chaos regions have previously been shown to be compositionally distinct from their surroundings (Fischer et al., 2015; Fischer et al., 2017; Trumbo et al., 2019), likely reflecting the contributions of endogenous material rich in chloride salts. To our knowledge, the effects of salty ice or frozen brines on the radiolytic formation of H_2O_2 have not been studied, leaving us with no reason to expect H_2O_2 enhancements due to salt. However, the addition of electron-accepting contaminants, such as O_2 and CO_2, to the ice has been shown to enhance H_2O_2 yields (Moore and Hudson, 2000). In these cases, the CO_2 and O_2 molecules slow the destruction of newly formed H_2O_2 by scavenging destructive electrons created during the continued irradiation of the ice. In fact, it has been noted that very limited NIMS data of portions of the leading hemisphere show a correlation between Europa's surface CO_2 and its H_2O_2 (Carlson, 2001; Carlson et al., 2009), although the spectra and corresponding maps were never published. Critically, these data cover portions of Tara Regio and Powys Regio, and demonstrate a clear enhancement of CO_2 in these chaos regions relative to the intervening plains (R. W. Carlson personal communication). Our NIRSPEC datasets map the same regions at the large scale. If we extrapolate the NIMS correlations, then the presence of CO_2 at low latitudes and in chaos terrain may help explain our observed H_2O_2 distribution. Perhaps more excitingly, if CO_2 is truly a dominant factor in controlling the H_2O_2 distribution on Europa, then the widespread coverage of our H_2O_2 data may hint at a broad association of Europa's CO_2 with its geologically young chaos terrain, and therefore with an interior carbon source. However, as no comprehensive map of Europa's CO_2 was ever made, and as the corresponding spectra were never published, more complete investigations of the distribution and abundance of Europa's CO_2 are certainly needed to address this hypothesis.

While we suggest that the observed H_2O_2 distribution may reflect that of Europa's CO_2, it is worth addressing some caveats to this hypothesis. One potential complication is the apparent lack of significant H_2O_2 on the trailing hemisphere, which contains extensive chaos terrain (Doggett et al., 2009) and potential spectral evidence for CO_2 (Hansen and McCord, 2008), although the spectra are poor quality. While water ice abundance does not appear to play a significant role in the latitudinal distribution of H_2O_2 on the leading and anti-Jovian hemispheres, it is possible that the more dramatic contrast in ice-fraction between the leading and trailing hemispheres accounts for their observed differences in H_2O_2 abundance. The widespread sulfur radiolysis experienced on the trailing hemisphere may also contribute to these differences. SO_2, a minor product of the radiolytic sulfur cycle on the trailing hemisphere (Carlson et al., 2002), reacts efficiently with H_2O_2 in water ice at temperatures relevant to Europa, rapidly producing sulfate (Loeffler and Hudson, 2013). Thus, while the composition of the leading hemisphere may enhance local H_2O_2 concentrations, the composition of the trailing hemisphere may act to deplete them.

Lastly, we would like to acknowledge the possibility that the 3.5 μm H_2O_2 band areas may not directly reflect relative H_2O_2 abundances, because they may also include the effects of geographically varying grain sizes. With only a single absorption band, it is impossible to disentangle the two effects. However, laboratory data suggest that H_2O_2 on Europa likely exists as isolated trimers ($H_2O_2 \cdot 2H_2O$) within the surface ice (Loeffler and Baragiola, 2005). It has been suggested that the ice grain size on Europa increases with latitude (Carlson et al., 2009; Cassidy et al., 2013), which should produce the opposite latitudinal trend in band area from what we observe. Thus, we feel that the 3.5 μm band of H_2O_2 likely represents a good proxy for its abundance.

5.5 Conclusions

Using ground-based L-band spectroscopy, we have mapped Europa's 3.5 μm H_2O_2 absorption across its surface. Although laboratory data would seem to suggest that Europa's H_2O_2 should be most abundant at the cold, icy high latitudes of the leading hemisphere, we find the strongest absorptions at low latitudes, preferentially within geologically young chaos terrain. We suggest that this distribution may largely reflect efficient electron scavenging by CO_2 within the chaos regions, which can enhance H_2O_2 concentrations. This hypothesis would benefit from continued mapping of Europa's H_2O_2 and CO_2 and from further laboratory experiments involving ion and electron irradiation of ice mixtures potentially reflective of the composition of

leading-hemisphere chaos terrain.

References

Brown, M. E. and K. P. Hand (2013). "Salts and Radiation Products on the Surface of Europa". *The Astronomical Journal* 145.4, p. 110.

Carlson, R. W. (2001). "Spatial Distribution of Carbon Dioxide, Hydrogen Peroxide, and Sulfuric Acid on Europa". *Bulletin of the American Astronomical Society*. Vol. 33, p. 1125.

Carlson, R. W. et al. (1999). "Hydrogen Peroxide on the Surface of Europa". *Science* 283.5410, pp. 2062–2064.

Carlson, R. W. et al. (2002). "Sulfuric Acid Production on Europa: The Radiolysis of Sulfur in Water Ice". *Icarus* 157.2, pp. 456–463.

Carlson, R. W. et al. (2009). "Europa". Ed. by R. T. Pappalardo, W. B. McKinnon, and K. Khurana. Tucson, AZ: The University of Arizona Press. Chap. Europa's Surface Composition, pp. 283–328.

Cassidy, T. A. et al. (2013). "Magnetospheric ion sputtering and water ice grain size at Europa". *Planetary and Space Science* 77. Surfaces, atmospheres and magnetospheres of the outer planets and their satellites and ring systems: Part VIII, pp. 64–73.

Chyba, C. F. (2000). "Energy for microbial life on Europa". *Nature* 403.6768, pp. 381–382.

Collins, G. and F. Nimmo (2009). "Europa". Ed. by R. T. Pappalardo, W. B. McKinnon, and K. Khurana. Tucson, AZ: The University of Arizona Press. Chap. Chaotic Terrain on Europa, pp. 259–282.

Cooper, P. D., R. E. Johnson, and T. I. Quickenden (2003). "Hydrogen peroxide dimers and the production of O2 in icy satellite surfaces". *Icarus* 166.2, pp. 444–446.

Dalton, J. B. et al. (2013). "Exogenic controls on sulfuric acid hydrate production at the surface of Europa". *Planetary and Space Science* 77, pp. 45–63.

Doggett, T. et al. (2009). "Europa". Ed. by R. T. Pappalardo, W. B. McKinnon, and K. Khurana. Tucson, AZ: University of Arizona Press. Chap. Geologic Stratigraphy and Evolution of Europa's surface, pp. 137–160.

Fischer, P. D., M. E. Brown, and K. P. Hand (2015). "Spatially Resolved Spectroscopy of Europa: The Distinct Spectrum of Large-Scale Chaos". *The Astronomical Journal* 150.5, p. 164.

Fischer, P. D. et al. (2017). "Spatially-resolved spectroscopy of Europa's large-scale compositional units at 3-4 microns with Keck NIRSPEC". *The Astronomical Journal* 153.1, p. 13.

Hand, K. P. and M. E. Brown (2013). "Keck II Observations of Hemispherical Differences in H_2O_2 on Europa". *The Astrophysical Journal* 766.2, p. L21.

Hand, K. P. and R. W. Carlson (2011). "H_2O_2 production by high-energy electrons on icy satellites as a function of surface temperature and electron flux". *Icarus* 215.1, pp. 226–233.

Hand, K. P. et al. (2009). "Europa". Ed. by R. T. Pappalardo, W. B. McKinnon, and K. Khurana. Tucson, AZ: The University of Arizona Press. Chap. Astrobiology and the Potential for Life on Europa, pp. 589–630.

Hansen, G. B. and T. B. McCord (2008). "Widespread CO2 and other non-ice compounds on the anti-Jovian and trailing sides of Europa from Galileo/NIMS observations". *Geophysical Research Letters* 35.1.

Johnson, R. E. and T. I. Quickenden (1997). "Photolysis and radiolysis of water ice on outer solar system bodies". *Journal of Geophysical Research: Planets* 102.E5, pp. 10985–10996.

Johnson, R. E. et al. (2003). "The Production of Oxidants in Europa's Surface". *Astrobiology* 3.4, pp. 823–850.

Loeffler, M. J. and R. A. Baragiola (2005). "The state of hydrogen peroxide on Europa". *Geophysical Research Letters* 32.17, p. L17202.

Loeffler, M. J. and R. L. Hudson (2013). "Low-temperature thermal reactions between SO_2 and H_2O_2 and their relevance to the jovian icy satellites". *Icarus* 224.1, pp. 257–259.

Loeffler, M.J. et al. (2006). "Synthesis of hydrogen peroxide in water ice by ion irradiation". *Icarus* 180.1, pp. 265–273.

Lord, S. D. (1992). *NASA Technical Memorandum 103957*. Ames Research Center, Moffett Field, CA.

Moore, M. H. and R. L. Hudson (2000). "IR Detection of H_2O_2 at 80 K in Ion-Irradiated Laboratory Ices Relevant to Europa". *Icarus* 145.1, pp. 282–288.

Nordheim, T. A., K. P. Hand, and C. Paranicas (2018). "Preservation of potential biosignatures in the shallow subsurface of Europa". *Nature Astronomy* 2.8, p. 673.

Paranicas, C. (2002). "The ion environment near Europa and its role in surface energetics". *Geophysical Research Letters* 29.5.

Paranicas, C., R. W. Carlson, and R. E. Johnson (2001). "Electron bombardment of Europa". *Geophysical Research Letters* 28.4, pp. 673–676.

Paranicas, C. et al. (2009). "Europa". Ed. by R. T. Pappalardo, W. B. McKinnon, and K. Khurana. Tucson, AZ: The University of Arizona Press. Chap. Europa's Radiation Environment and its Effects on the Surface, pp. 529–544.

Robitaille, T. P., E. J. Tollerud, P. Greenfield, et al. (2013). "Astropy Collaboration". *Astronomy and Astrophysics* 558.A33, p. 9.

Schmidt, B. E. et al. (2011). "Active formation of 'chaos terrain' over shallow subsurface water on Europa". *Nature* 479.7374, p. 502.

Spencer, J. R. et al. (1999). "Temperatures on Europa from Galileo photopolarimeter-radiomer: nighttime thermal anomalies". *Science* 284.5419, pp. 1514–1516.

Trumbo, S. K., M. E. Brown, and K. P. Hand (2019). "Sodium chloride on the surface of Europa". *Science Advances* 5.6. DOI: 10.1126/sciadv.aaw7123.

Walt, S. van der et al. (2014). "scikit-image: image processing in Python". *PeerJ* 2.e453.

Zheng, W., D. Jewitt, and R. I. Kaiser (Sept. 2006). "Temperature Dependence of the Formation of Hydrogen, Oxygen, and Hydrogen Peroxide in Electron-Irradiated Crystalline Water Ice". *The Astrophysical Journal* 648.1, pp. 753–761.

Chapter 6

ALMA THERMAL OBSERVATIONS OF A PROPOSED PLUME SOURCE REGION ON EUROPA

Trumbo, S. K., M. E. Brown, and B. J. Butler (2017). "ALMA Thermal Observations of a Proposed Plume Source Region on Europa". *The Astronomical Journal* 154.4, p. 148. DOI: 10.3847/1538-3881/aa8769.

ABSTRACT

We present a daytime thermal image of Europa taken with the Atacama Large Millimeter Array. The imaged region includes the area northwest of Pwyll Crater, which is associated with a nighttime thermal excess seen by the Galileo Photopolarimeter Radiometer and with two potential plume detections. We develop a global thermal model of Europa and simulate both the daytime and nighttime thermal emission to determine if the nighttime thermal anomaly is caused by excess endogenic heat flow, as might be expected from a plume source region. We find that the nighttime and daytime brightness temperatures near Pwyll Crater cannot be matched by including excess heat flow at that location. Rather, we can successfully model both measurements by increasing the local thermal inertia of the surface.

6.1 Introduction

Europa may be one of the most habitable worlds in the Solar System. Beneath a relatively thin ice shell, it hosts a liquid water ocean in contact with a rocky core (Anderson et al., 1998; Kivelson et al., 2000). Europa's young surface age, surface geology, and salty surface composition point to a history of geologic activity that may have facilitated contact between the ocean and the surface environments (e.g. Bierhaus et al., 2009; Kattenhorn and Hurford, 2009; McCord et al., 1999; Fischer et al., 2015). If such activity continued today, then direct study of the oceanic composition may be possible, but the question of modern geologic activity remains. Recent observations using the Hubble Space Telescope (HST) have hinted at the possibility of active water vapor plumes at Europa (Roth et al., 2014b; Roth et al., 2014a; Sparks et al., 2016; Sparks et al., 2017). However, the detections have been sporadic and tenuous, making confirming the existence of plumes difficult.

It is possible that sites of recent or ongoing geologic activity would cause persistent spatially localized thermal anomalies, similar to the so-called "tiger stripes" of Enceladus (Spencer et al., 2006). Therefore, high-resolution thermal data may present another, perhaps more robust, way of identifying active regions in the case of Europa.

Sparks et al. (2016) and Sparks et al. (2017) detected potential off-limb absorption near the crater Pwyll in HST images of Europa as it transited Jupiter. This location is coincident with a nighttime thermal excess in brightness temperatures measured by the Galileo Photopolarimeter-Radiometer (PPR) (Spencer et al., 1999; Moore et al., 2009). If the thermal excess were caused by increased subsurface heat flow, this association could corroborate the interpretation that the off-limb features are due to subsurface geologic activity and the venting of plume material. However, endogenic heating is not the only potential cause of thermal anomalies; they can also be due to localized variations in surface properties, such as albedo or thermal inertia. In the case of nighttime thermal anomalies, like the one in question, thermal inertia becomes particularly important. Indeed, Spencer et al. (1999) cite thermal inertia as a potential explanation for the nighttime brightness temperatures near Pwyll.

Anomalies caused by variations in thermal inertia and in endogenic heat flow should have diurnal temperature curves that behave differently over the course of a Europa day, making distinguishing between these explanations possible with temperature measurements at more than one time of day. The published Galileo PPR maps include only a single nighttime observation of the region surrounding Pwyll Crater

(Spencer et al., 1999). We present a complementary thermal observation obtained using the Atacama Large Millimeter Array (ALMA), which captures the region of interest during the daytime. Using a thermal model, we fit both the ALMA and Galileo PPR observations and evaluate whether the anomaly is best explained by variation in the thermal inertia or whether it is truly indicative of an endogenic hot spot.

6.2 ALMA Observations and Data Reduction

The observations described herein were undertaken with the 12-m array of the Atacama Large Millimeter Array (ALMA). This synthesis array is a collection of radio antennas, each 12 m in diameter, spread out on the Altiplano in the high northern Chilean Andes. Each of the pairs of antennas acts as a two-element interferometer, and the combination of all of these individual interferometers allows for the reconstruction of the full sky brightness distribution, in both dimensions.

ALMA is tunable in 7 discrete frequency bands, from ~ 90 to ~ 950 GHz. The observation described in this paper was taken in Band 6, near 230 GHz, in the "continuum" (or "TDM") mode, with the standard frequency tuning. For band 6, this yields four spectral windows in the frequency ranges: 224–226 GHz; 226–228 GHz; 240–242 GHz; and 242–244 GHz. In the final data analysis, we averaged over the entire frequency range in both bands, and we use 233 GHz as the effective frequency in our modeling.

We observed Europa with ALMA on November 27 of 2015 from 10:00 to 10:40 UTC. At the center time of the observation, the sub-Earth longitude was 319.5° and the sub-Earth latitude was -1.54°, capturing Pwyll Crater in the afternoon at ~ 60° past local noon. ALMA had 50 available antennas in its C36-7 configuration, with a maximum useable antenna spacing of ~ 5 km.

Fully calibrated visibility data were provided by ALMA. We performed several iterations of self-calibration (Taylor et al., 1999) on the visibility data to create a deconvolved Europa image with the 0.05" effective resolution of the interferometer. Figure 6.1 shows this image with a pixel sampling of 10 times the full spatial resolution. With this resolution, and given Europa's projected diameter of 0.77" on the sky, we obtained ~15 resolution elements across the disk.

6.3 Thermal Modeling

We develop a global thermal diffusion model for Europa, similar to those developed in the past for several solar system bodies (e.g Spencer et al., 1989; Spencer, 1990; Hayne and Aharonson, 2015). The model begins with calculations of solar insolation across the surface, where the solar flux absorbed at each point on the disk is given by

$$F_{abs} = (1 - A)\mu \frac{F_{solar}}{r^2}. \tag{6.1}$$

Here, μ is the cosine of the solar incidence angle with respect to the local surface normal, F_{solar} is the solar constant at 1 AU, r is the solar distance in AU, and A is the hemispherical albedo at that point.

In the absence of anomalous endogenic heating and in the limit of very low thermal inertia, the surface temperatures are the result of instantaneous radiative equilibrium with the absorbed flux. However, real bodies will have a finite thermal inertia,

$$I = \sqrt{\rho c_p K}, \tag{6.2}$$

where ρ is the density, c_p is the specific heat capacity, and K is the thermal conductivity, resulting in a diurnal thermal wave with depth. Temperature as a function of time, t, and depth, z, is then given by the one-dimensional heat equation

$$\rho c_p \frac{\partial T}{\partial t} = \frac{\partial}{\partial z}\left(K \frac{\partial T}{\partial z}\right). \tag{6.3}$$

The model achieves a numerical solution to this equation by computing finite differences across depth elements. We assume a global heat flux of 20 mW/m^2 (Mitri and Showman, 2005; Barr and Showman, 2009) as a lower boundary condition and an outgoing surface flux of $\epsilon\sigma T^4$ as an upper boundary condition, where ϵ and σ are the bolometric emissivity and Stefan-Boltzmann constant, respectively. We simulate a total of 5 diurnal skin depths, where the skin depth is given by

$$d = \sqrt{\frac{KP}{\pi \rho c_p}} \tag{6.4}$$

and P is the rotational period of Europa. We define the thickness of the top layer to be $d/30$, with the thickness of each subsequent layer increasing by a factor of 1.2.

We run the model using a time step no greater than 1/500 of a Europa day and allow it to equilibrate until the maximum difference in surface temperature across 5 Europa days at any point on the disk is less than 1% (usually 10 - 15 Europa days). Further equilibration results in differences $\ll$1 K everywhere on the disk. The product is a temperature map of the surface of Europa, which can be output at any point in time throughout the Europa day.

We use this simple thermal model combined with an approximated high-resolution albedo map of the surface to simulate the ALMA and Galileo observations and establish a baseline against which to assess thermal anomalies. Since no published high-resolution albedo map of the surface exists, we construct a high-resolution map by using discrete Voyager normal albedos as tie-points to the USGS Voyager/Galileo greyscale basemap of Europa (at 2 pixel/degree resolution) (USGS, 2002). We take the normal albedo points of McEwen (1986) in the Voyager green, blue, violet, and ultraviolet filters, weight them by the width of each filter and the magnitude of the solar flux at the relevant wavelengths, and then add them to get approximate wavelength-integrated normal albedos. We then find the greyscale value of each corresponding point in the USGS basemap and use the resulting linear correlation to get an approximate wavelength-integrated normal albedo for each point in the USGS map. The greyscale values and approximate normal albedos correlate linearly with an R^2 of .92 and a standard deviation of .03, which we take as the statistical error in our albedos. As the phase integral of Europa is 1.01 (Grundy et al., 2007), we take these normal albedos as approximate hemispherical albedos and use them in model calculations of solar flux absorbed across the surface of Europa.

In modeling the observations, we take the thermal inertia and emissivity as free parameters and treat the entire disk as homogenous in these properties. We assume a snow-like constant regolith density of 500 kg/m^3 (Spencer et al., 1999) and a c_p of 900 $J/(K \cdot kg)$, which is appropriate for water ice near 100 K (Feistel and Wagner, 2006). After equilibration, we halt the simulation at the time specified by the sub-solar longitude of the observation. We then convert surface temperatures into flux units via Planck's Law and project the model output based on the viewing geometry of the observation, such that the central point on the disk corresponds to the sub-observer coordinates.

When modeling the ALMA observation, we apply a Gaussian filter with full widths at half maximum (FWHMs) corresponding to those of the elliptical ALMA beam to smooth the output to match ALMA resolution. When modeling the Galileo PPR

observation, we apply a Gaussian filter consistent with a 140-km linear resolution, within the 80–200-km resolution of the PPR observations (Spencer et al., 1999). Finally, we convert the smoothed images into brightness temperature, again using Planck's Law, and compare them to the actual observations. The nighttime PPR observation of Pwyll was taken in the open filter position (sensitive from 0.35 to $\sim$ 100 μm), but these brightness temperatures generally agreed to $<$ 1 K with those taken in the 27.5 μm filter (Spencer et al., 1999). Thus, in modeling the PPR observation, we output brightness temperatures for a wavelength of 27.5 μm (Spencer et al., 1999). In modeling the ALMA observation, we calculate brightness temperatures at a wavelength of 1.3 mm (233 GHz). We treat the emissivities of the surface at the ALMA and PPR wavelengths as equal. This assumption is reasonable in the case of water ice under laboratory conditions, as the optical constants are similar at both wavelengths (Warren and Brandt, 2008). However, the relevant emissivities for Europa-like conditions and compositions are not known.

It should be noted that, for emissivities less than 1, the resulting brightness temperatures at these two wavelengths will be significantly different. While the ALMA wavelength is nearly in the Rayleigh-Jeans limit, the Galileo PPR was sensitive to Europa's $\sim$ 30 μm blackbody peak. In both cases, Planck's law can be used to find the brightness temperature in terms of the physical temperature

$$T_b = \frac{h\nu}{k}\left(ln\left[1 + \frac{e^{h\nu/kT} - 1}{\epsilon}\right]\right)^{-1}, \tag{6.5}$$

where ν is the frequency, h is Planck's constant, k is Boltzmann's constant, and ϵ is the emissivity. This equation gives different results for the two wavelength regimes. For instance, an emissivity of 0.8 and a physical temperature of 125 K, produce a brightness temperature of 119 K at 27.5 μm and a brightness temperature of 101 K at 1.3 mm. It should also be noted that the two observations were taken at very different solar distances. During the PPR observation, Jupiter was near perihelion (at 4.96 AU). However, it was near aphelion (at 5.4 AU) in 2015 when the ALMA image was taken. We account for this effect in our model.

Some caveats do apply to our very simple model, however. First, we do not include the effects of surface roughness. Rough topography has the tendency to enhance surface temperatures, with the largest effects appearing at the limbs. However, Europa is thought to be relatively smooth compared to other solar system bodies (e.g. Spencer, 1987; Domingue and Verbiscer, 1997). We tested a roughness model

with rms slopes up to 20°, using a similar implementation of surface roughness to Hayne and Aharonson (2015), and found that the effects did not significantly affect our results.

Second, our model assumes that the thermal emission imaged in the ALMA and Galileo observations originates from the topmost model layer. For the Galileo PPR observations, which were sensitive to the $\sim 30\ \mu m$ blackbody peak of Europa, this is a valid assumption. However, ALMA senses slightly deeper into the surface at a wavelength of 1.3 mm. Thus, model ALMA brightness temperatures for a given ϵ and I are slightly warmer than they would be if this effect were included. In testing a variation of our simple model, which included sensing beneath the surface with an e-folding of 1 cm, we found that much of this brightness temperature variation was captured by a slight change in the model emissivity, ϵ.

Finally, our model assumes that all of the absorbed solar flux is captured in the topmost layer. This is the standard assumption in many thermal models (e.g. Spencer et al., 1989; Spencer, 1990; Hayne and Aharonson, 2015), and is valid for solar system bodies with low bolometric albedos. However, it is possible that sunlight is able to penetrate to significant depths beneath a high albedo surface, such as that of much of Europa (e.g Brown and Matson, 1987; Urquhart and Jakosky, 1996). As this effect can create a heat reservoir at depth, it can be difficult to distinguish from a change in thermal inertia (Urquhart and Jakosky, 1996). We found this to be true in testing a version of our model that also included sunlight propagation with an e-folding of 2 cm, and this effect did not improve our fits to the data.

For this analysis, we are primarily interested in relative local variation in the thermal parameters near Pwyll Crater, rather than in accurately determining the true global values. Thus, we choose to present the simplest model, with the knowledge that some of the caveats discussed here may manifest as changes in our model parameters.

6.4 Fits to ALMA and Galileo PPR Observations

In order to obtain simultaneous best-fit parameters to both the ALMA and Galileo PPR data, we run our model for each observation over a wide grid of thermal inertias and emissivities and minimize the sum of the squares of the residuals for the region covered by both datasets. By fitting both observations at once, we find that an emissivity of 0.8 and a thermal inertia of 95 $J/(m^2 \cdot K \cdot s^{1/2})$ provide the best result for the overlapping region. This thermal inertia is slightly higher than the value of 70 $J/(m^s \cdot K \cdot s^{1/2})$ reported by Spencer et al. (1999) for the

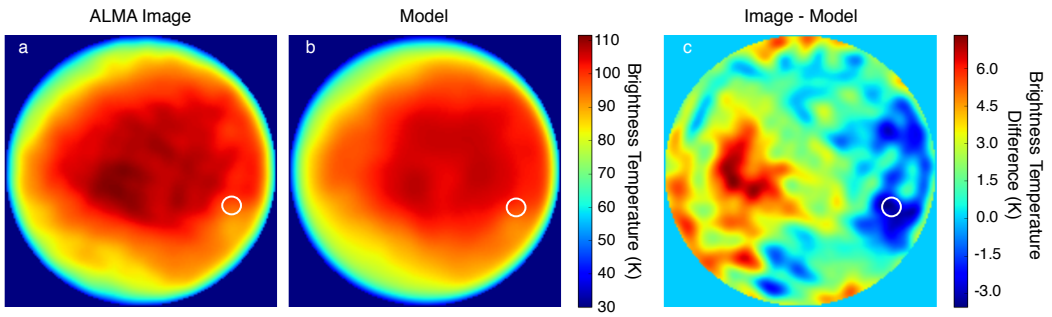

Figure 6.1: Model fit to the ALMA data. (a) shows the ALMA image in brightness temperature at $\lambda = 1.3$ mm. (b) shows our model image using the best-fit parameters to both the ALMA and PPR data. (c) shows the residuals between the model and the data, where positive values indicate locations where the data are warmer than the model. The location of the potential plume source region and Galileo thermal anomaly is circled in white, where the size of the circle corresponds to the size of our ALMA resolution element.

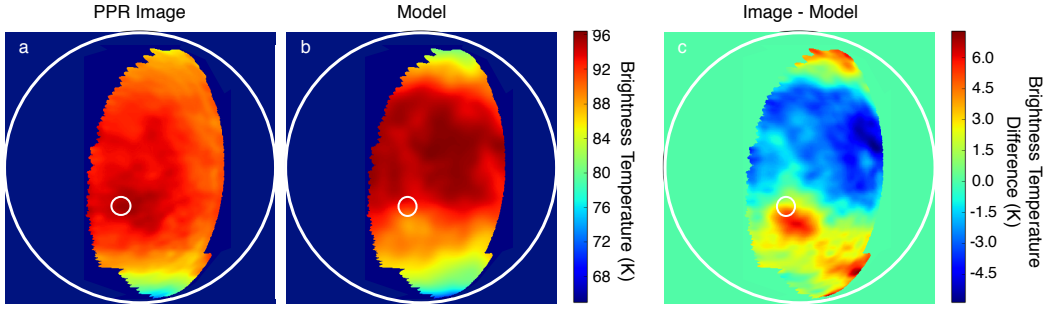

Figure 6.2: Model fit to the PPR data. (a) shows the PPR image in brightness temperature at $\lambda = 27.5\ \mu m$. (b) shows our model image using the best-fit parameters to both the ALMA and PPR data. (c) illustrates the residuals between the model and the data, where positive values indicate locations where the data are warmer than the model. The location of the potential plume source region and Galileo thermal anomaly is circled in white, where the size of the circle corresponds to the size of our ALMA resolution element.

equatorial latitudes, but is within the range of 30–140 $J/(m^s \cdot K \cdot s^{1/2})$ calculated by Rathbun et al. (2010). Our ALMA observation, best-fit model ALMA image, and the corresponding residuals are shown in Figure 6.1, where the approximate location of the Galileo thermal anomaly and potential plume source region is circled. While the homogenous thermal model is able to reproduce the large-scale structure of the ALMA image well, there are significant localized discrepancies, which are not necessarily surprising given the inhomogeneous nature of Europa's surface. This observation includes much of the dark trailing hemisphere of Europa, which is compositionally diverse (Carlson et al., 2009). Therefore, we do not expect the surface to be well-represented by a single thermal inertia or emissivity. However, it is interesting that the area associated with the Galileo nighttime thermal excess is actually colder in the ALMA data than the model predicts. For the Galileo PPR observation, shown in Figure 6.2 alongside the best-fit model image and the resulting residuals, the same location is indeed anomalously warm, as noted by Spencer et al. (1999) and Sparks et al. (2017). In fact, the entire Pwyll Crater region, not just the potential plume source location slightly northwest of the crater, shows up as anomalously hot at night and cold during the day. This pattern is suggestive of a variation in the local thermal inertia. If the thermal anomaly were instead due to an endogenic hot spot with an excess subsurface heat flux, one would expect the area to have elevated brightness temperatures throughout the diurnal cycle.

To investigate whether the ALMA and PPR brightness temperatures are best explained by an endogenic hot spot or a thermal inertia anomaly, we model the location of the anomaly under both scenarios over the course of a diurnal cycle and attempt to fit both data points. We simulate an area 156 km in radius (corresponding to our ALMA resolution in this region) centered on 276° W and 16.8° S, which is coincident with the Galileo thermal anomaly in the potential plume source region (Sparks et al., 2016; Sparks et al., 2017). We model the case of an endogenic thermal anomaly by raising the geothermal heat flux beneath the lowest layer of our simulation (5 diurnal skin depths $\approx$ 0.75 m at our best-fit parameters). We define the best fits by minimizing the sum of the squares of the differences between the models and the two data points. The results of these fits are shown in Figure 6.3, where the ALMA data point is taken to be 95.6 K, the ALMA brightness temperature at 276° W and 16.8° S, and the PPR data point is 95.1 K, the brightness temperature given by averaging the measured flux over an area 156 km in radius centered on the same location.

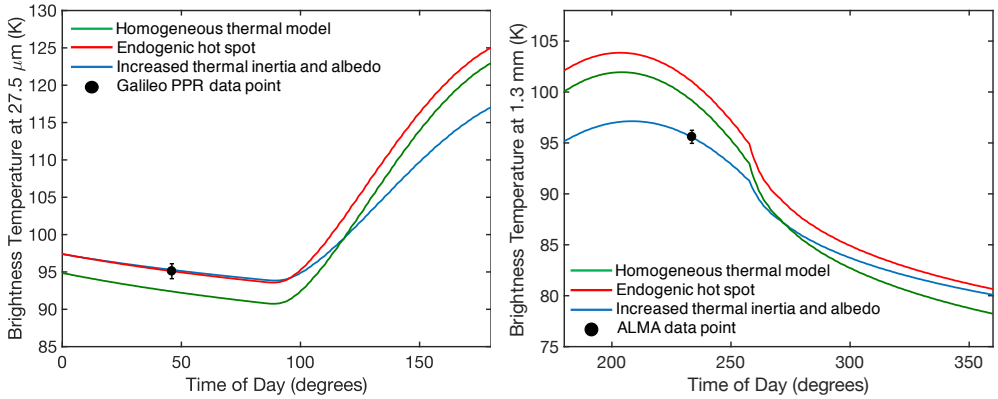

Figure 6.3: Model fits to the ALMA and PPR data points. Here, 180° indicates local noon and 0° is local midnight. Both points are fit well by raising the thermal inertia and adjusting the albedo by ~ 5%. Invoking an endogenic hotspot to explain the Galileo nighttime thermal anomaly, however, results in a daytime brightness temperature much higher than that measured by ALMA. The homogenous thermal model obtained by simultaneously fitting the Galileo and ALMA observations fails to fit the anomalous region during either the night or the day. The steep drop in brightness temperature at ~ 260° coincides with Europa being eclipsed by Jupiter. Also, note the differences in the y-axes. The Galileo point is fit with brightness temperatures at 27.5 μm, while the ALMA point is fit with brightness temperatures at 1.3 mm. The noise levels of the PPR observations are stated to be < 1 K (Spencer et al., 1999), and a 1 K error bar is shown here. The statistical error on the ALMA measurement is +/- 0.6 K.

Overall, we find that the ALMA and Galileo measurements are best explained by invoking a thermal inertia anomaly, and that the anomalous region cannot be solely attributed to endogenic heating. We successfully match both measurements by increasing the thermal inertia by 47% from 95 to 140 $J/(m^2 \cdot K \cdot s^{1/2})$ and increasing the albedo of the region by 5% from 0.56 to 0.59, which is within our albedo uncertainties. However, we are unable to successfully fit both brightness temperatures with a subsurface hot spot. Reproducing the Galileo nighttime brightness temperature requires raising the subsurface heat flux from 0.02 W/m^2 to 0.66 W/m^2, which produces a daytime brightness temperature much higher than we observed with ALMA (Figure 6.3).

Similarly, a combination of subsurface heating and a thermal inertia anomaly cannot explain the two measurements. As endogenic heating increases both day and night temperatures, fitting one of the two data points in this manner always overestimates the brightness temperature of the other. We can only invoke endogenic heating in matching the data if we also significantly raise the local albedo. A local heat flux of

$1.6\,W/m^2$ can account for both the ALMA and Galileo PPR brightness temperatures, but only when combined with a local albedo increase of 23% from 0.56 to 0.69, a 4σ deviation from our albedo model. Discrepancies of this magnitude would only result from systematic biases, rather than occur in isolation at one location. Systematic albedo biases would affect the entire albedo map and be largely absorbed by changes in the best-fit parameters. Thus, we argue that the simplest and most likely explanation for the Galileo nighttime thermal anomaly near Pwyll Crater is a moderate increase in the local thermal inertia.

Spatially localized thermal inertia variations can result from a number of causes, including compositional differences and changes in the average grain size of the surface material. An elevated thermal inertia near Pwyll Crater and the anomaly in question, as originally noted by Spencer et al. (1999), may result from higher average regolith particle sizes in the ejecta blanket. This possibility seems particularly plausible as the anomalous temperatures are not just constrained to the relatively small potential plume source area (Sparks et al., 2017), but are observed across the entirety of the Pwyll region (Figures 6.1 and 6.2). Spencer et al. (1999) also suggest the possibility that impact-exposed water ice may allow for deeper sunlight penetration, which, as discussed in Section 6.3, can mimic the effects of increased thermal inertia.

One final potential explanation warrants mentioning. We cannot rule out the possibility that the region associated with the thermal anomaly was anomalously warm due to endogenic heat at the time of the Galileo observation in 1998, but has since cooled. For instance, if a hot spot were not actively heated, but rather were caused by a singular upwelling of liquid water or warm ice at or near the surface, then detectable heat signatures need not necessarily last the 17 years between the Galileo and ALMA observations (Abramov and Spencer, 2008). However, our ALMA observation was taken in 2015, prior to the 2016 potential plume detection of Sparks et al. (2017). Thus, if the hot spot had dissipated by the time of our observation, then the same anomaly cannot be linked to that of Sparks et al. (2017).

6.5 Conclusions

Using ALMA, we obtained a daytime thermal measurement of the Galileo PPR nighttime thermal excess (Spencer et al., 1999) near Pwyll Crater, which is associated with two potential plume detections (Sparks et al., 2016; Sparks et al., 2017). If the thermal excess were due to an endogenic hot spot, then it could support the idea that

the region northwest of Pwyll exhibits modern geologic activity. Using a global one-dimensional thermal diffusion model, we fit both the ALMA and PPR observations. However, while the location in question does appear hot relative to our model at night, it appears colder in our ALMA daytime image than the model predicts. We suggest that this pattern is indicative of a locally elevated thermal inertia. To investigate whether we can simultaneously explain both temperature measurements with endogenic heating or need to invoke a thermal inertia anomaly, we model the potential plume source location over the entire course of a Europa day under both scenarios and attempt to fit the two measured brightness temperatures. While we can explain the Galileo nighttime brightness temperature with an endogenic heat source, this situation results in a daytime brightness temperature that is too hot. However, we successfully fit both observations by raising the local thermal inertia by 47% and adjusting the albedo by an amount within our uncertainties. We therefore conclude that the nighttime Galileo thermal anomaly is most likely explained by a variation in the local surface thermal inertia, which may result from its proximity to the crater Pwyll.

References

Abramov, O. and J. R. Spencer (2008). "Numerical modeling of endogenic thermal anomalies on Europa". *Icarus* 195.1, pp. 378–385.

Anderson, J. D. et al. (1998). "Europa's differentiated internal structure: Inferences from four Galileo encounters". *Science* 281.5385, pp. 2019–2022.

Barr, A. C. and A. P. Showman (2009). "Europa". Ed. by R. T. Pappalardo, W. B. McKinnon, and K. Khurana. Tucson, AZ: The University of Arizona Press. Chap. Heat Transfer in Europa's Icy Shell, pp. 405–430.

Bierhaus, E. B., K. Zahnle, and C. R. Chapman (2009). "Europa". Ed. by R. T. Pappalardo, W. B. McKinnon, and K. Khurana. Tucson, AZ: The University of Arizona Press. Chap. Europa's Crater Distributions and Surface Ages, pp. 161–180.

Brown, R. H. and D. L. Matson (1987). "Thermal effects of insolation propagation into the regoliths of airless bodies". *Icarus* 72.1, pp. 84–94.

Carlson, R. W. et al. (2009). "Europa". Ed. by R. T. Pappalardo, W. B. McKinnon, and K. Khurana. Tucson, AZ: The University of Arizona Press. Chap. Europa's Surface Composition, pp. 283–328.

Domingue, D. and A. Verbiscer (1997). "Re-analysis of the solar phase curves of the icy Galilean satellites". *Icarus* 128.1, pp. 49–74.

Feistel, R. and W. Wagner (2006). "A new equation of state for H_2O ice Ih". *Journal of Physical and Chemical Reference Data* 35.2, pp. 1021–1047.

Fischer, P. D., M. E. Brown, and K. P. Hand (2015). "Spatially Resolved Spectroscopy of Europa: The Distinct Spectrum of Large-Scale Chaos". *The Astronomical Journal* 150.5, p. 164.

Grundy, W. M. et al. (2007). "New Horizons mapping of Europa and Ganymede". *Science* 318.5848, pp. 234–237.

Hayne, P. O. and O. Aharonson (2015). "Thermal stability of ice on Ceres with rough topography". *Journal of Geophysical Research: Planets* 120.9, pp. 1567–1584.

Kattenhorn, S. A. and T. Hurford (2009). "Europa". Ed. by R. T. Pappalardo, W. B. McKinnon, and K. Khurana. Tucson, AZ: The University of Arizona Press. Chap. Tectonics of Europa, pp. 199–236.

Kivelson, M. G. et al. (2000). "Galileo magnetometer measurements: A stronger case for a subsurface ocean at Europa". *Science* 289.5483, pp. 1340–1343.

McCord, T. B. et al. (1999). "Hydrated salt minerals on Europa's surface from the Galileo near-infrared mapping spectrometer (NIMS) investigation". *Journal of Geophysical Research: Planets* 104.E5, pp. 11827–11851.

McEwen, A. S. (1986). "Exogenic and endogenic albedo and color patterns on Europa". *Journal of Geophysical Research: Solid Earth* 91.B8, pp. 8077–8097.

Mitri, G. and A. P. Showman (2005). "Convective-conductive transitions and sensitivity of a convecting ice shell to perturbations in heat flux and tidal-heating rate: Implications for Europa". *Icarus* 177.2, pp. 447–460.

Moore, J. M. et al. (2009). "Europa". Ed. by R. T. Pappalardo, W. B. McKinnon, and K. Khurana. Tucson, AZ: The University of Arizona Press. Chap. Surface Properties, Regolith, and Landscape Degradation, pp. 329–349.

Rathbun, J. A., N. J. Rodriguez, and J. R. Spencer (2010). "Galileo PPR Observations of Europa: Hotspot Detection Limits and Surface Thermal Properties". *Icarus* 210.2, pp. 763–769.

Roth, L. et al. (Oct. 2014a). "Orbital apocenter is not a sufficient condition for HST/STIS detection of Europa's water vapor aurora". *PNAS* 111.48, E5123–E5132.

Roth, L. et al. (Jan. 2014b). "Transient water vapor at Europa's south pole". *Science* 343.6167, pp. 171–174.

Sparks, W. B. et al. (2016). "Probing for evidence of plumes on Europa with HST/STIS". *The Astrophysical Journal* 829.2, p. 121.

Sparks, W. B. et al. (2017). "Active Cryovolcanism on Europa?" *The Astrophysical Journal* 839.2, p. L18.

Spencer, J. R. (1987). “Surfaces of Europa, Ganymede, and Calllisto: an investigation using Voyager IRIS thermal infrared spectra”. PhD thesis. Tuscon, AZ: University of Arizona.

Spencer, J. R. (1990). “A rough-surface thermophysical model for airless planets”. *Icarus* 83.1, pp. 27–38.

Spencer, J. R., L. A. Lebofsky, and M. V. Sykes (1989). “Systematic biases in radiometric diameter determination”. *Icarus* 78.2, pp. 337–354.

Spencer, J. R. et al. (1999). “Temperatures on Europa from Galileo photopolarimeter-radiomer: nighttime thermal anomalies”. *Science* 284.5419, pp. 1514–1516.

Spencer, J. R. et al. (2006). “Cassini encounters Enceladus: Background and the discovery of a south polar hot spot”. *Science* 311.5766, pp. 1401–1405.

Taylor, G. B., C. L. Carilli, and R. A. Perley (1999). “Synthesis Imaging in Radio Astronomy II”. *Synthesis Imaging in Radio Astronomy II*. Vol. 180.

Urquhart, M. L. and B. M. Jakosky (1996). “Constraints on the solid-state greenhouse effect on the icy Galilean satellites”. *Journal of Geophysical Research: Planets* 101.E9, pp. 21169–21176.

USGS (2002). *Controlled photomosaic map of Europa, Je 15M CMN: U.S. Geological Survey Investigations Series I-2757*. (Visited on).

Warren, S. G. and R. E. Brandt (2008). “Optical constants of ice from the ultraviolet to the microwave: A revised compilation”. *Journal of Geophysical Research: Atmospheres* 113.D14.

Chapter 7

ALMA THERMAL OBSERVATIONS OF EUROPA

Trumbo, S. K., M. E. Brown, and K. P. Hand (2018). "ALMA Thermal Observations of Europa". *The Astronomical Journal* 156.4, p. 161. DOI: 10.3847/1538-3881/aada87.

ABSTRACT

We present four daytime thermal images of Europa taken with the Atacama Large Millimeter Array. Together, these images comprise the first spatially resolved thermal dataset with complete coverage of Europa's surface. The resulting brightness temperatures correspond to a frequency of 233 GHz (1.3 mm) and a typical linear resolution of roughly 200 km. At this resolution, the images capture spatially localized thermal variations on the scale of geologic and compositional units. We use a global thermal model of Europa to simulate the ALMA observations in order to investigate the thermal structure visible in the data. Comparisons between the data and model images suggest that the large-scale daytime thermal structure on Europa largely results from bolometric albedo variations across the surface. Using bolometric albedos extrapolated from *Voyager* measurements, a homogenous model reproduces these patterns well, but localized discrepancies exist. These discrepancies can be largely explained by spatial inhomogeneity of the surface thermal properties. Thus, we use the four ALMA images to create maps of the surface thermal inertia and emissivity at our ALMA wavelength. From these maps, we identify a region of either particularly high thermal inertia or low emissivity near 90 degrees West and 23 degrees North, which appears anomalously cold in two of our images.

7.1 Introduction

Europa's icy surface is marked by fractured, ridged, and chaotic terrain suggestive of a history of geologic activity (e.g. Kattenhorn and Hurford, 2009; Prockter and Patterson, 2009; Collins and Nimmo, 2009). Spectroscopic studies have revealed multiple compositions that reflect the influences of both endogenous geologic processes (e.g. McCord et al., 1998; Fischer et al., 2015) and exogenous radiolytic processing by Jovian magnetospheric particles (e.g. Carlson et al., 1999; Carlson et al., 2002), but the balance of these influences in shaping surface properties is not well understood. Surface temperature measurements can provide an additional window onto both types of processes. Such measurements present perhaps the best means for identifying regions of active geologic activity. Indeed, active hotspots persist at both the "tiger stripes" of Enceladus (Spencer et al., 2006) and the volcanoes of Io (Pearl and Sinton, 1982; Spencer et al., 1990). In addition, *Cassini* thermal observations of Saturn's moons Mimas and Tethys have shown that temperature measurements can reveal details on the effects of magnetospheric particle bombardment on surface texture (Howett et al., 2011; Howett et al., 2012). Finally, thermal data can provide insight on diurnal sublimation cycles, impact gardening by micrometeorites, and sputtering from particle impacts, which also affect the surface compositions and morphologies and, thus, the surface thermophysical properties.

To date, the only spatially resolved thermal data of Europa were collected by the *Galileo* Photopolarimeter-Radiometer (PPR). These data provided the first brightness temperature maps of the surface and included both daytime and nighttime measurements (Spencer et al., 1999). Modeling efforts using the PPR data have found thermal inertia values between 30 – 140 $J/(m^2 \cdot K \cdot s^{1/2})$, consistent with a particulate, uncompacted regolith texture unlike that of solid water-ice (Spencer et al., 1999; Rathbun et al., 2010). However, the *Galileo* PPR only obtained limited coverage of the surface. Furthermore, from the end of the *Galileo* mission until very recently, subsequent brightness temperature measurements of similar quality and spatial resolution have been impossible to achieve. Recently, however, the Atacama Large Millimeter Array (ALMA) has made the collection of spatially resolved, high-quality thermal datasets possible.

Here, we present four ALMA thermal images that together cover the entire surface of Europa at a frequency of 233 GHz (1.3 mm) with a typical linear resolution of ~200 km. Using a global thermal model of Europa, we fit the observations and investigate the nature of thermal structure visible across the surface.

Table 7.1: ALMA observations of Europa's thermal (λ = 1.3 mm) emission.

Date (UT)	Time (Start/End)	Sub-Earth Longitude Range	Sub-Earth Latitude	Elliptical Beam Resolutions (Milliarcseconds)
2015 Nov 17	14:36/14:50	44.9–45.9	-1.44	57/42
2015 Nov 25	11:25/11:41	121.5–122.6	-1.52	59/53
2015 Nov 26	08:22/08:38	210–211.1	-1.52	77/52
2015 Nov 27	10:00/10:40	318.1–320.9	-1.54	54/53

7.2 ALMA Observations and Data Reduction

The observations of Europa were taken with the main array of the Atacama Large Millimeter Array (ALMA), which is composed of up to 50 12-meter diameter antennas spread across the Altiplano in the high northern Chilean Andes. Every pair of antennas acts as a two-element interferometer, and together these individual interferometers allow for the reconstruction of the the full sky brightness in both dimensions (Thompson et al., 2001).

ALMA can operate in 7 frequency windows, from ~90 to ~950 GHz. The observations presented here were taken in Band 6, near 230 GHz, in the "continuum" (or "TDM") mode, with the standard frequency tuning. This results in four spectral windows with frequencies: 223–225 GHz, 225–227 GHz, 239–241 GHz, and 241–243 GHz. In the data reduction, we average over the entire frequency range, and use 233 GHz as the observation frequency in our thermal modeling.

We observed Europa with ALMA on November 17, 25, 26, and 27 of 2015. For these observations, there were between 38 and 43 antennas, in the C36-7 configuration. This configuration has a maximum antenna spacing of ~5 km, giving a resolution on the sky of ~50 milliarcseconds, and a minimum antenna spacing of ~250 m, giving a largest theoretical recoverable scale of ~0.65 arcseconds. Details of observation times, geometries, and resolutions are given in Table 7.1.

All of these observations are in dual-linear polarization; in the end we combine these into a measurement of Stokes I. While we expect polarized emission from the surface, it is relatively weak, and we did not measure the cross-polarized signals.

Each observation was about 20 minutes in duration, including all calibration overheads, which resulted in roughly 8 minutes on Europa. The point-like calibrator J1058+0133 was used as the absolute flux density scale calibrator for all four observations — it is part of a grid of calibrators which are regularly monitored against the

main flux density scale calibrators for ALMA (Butler, 2012). The nearby calibrator J1108+0811 was used to calibrate the phase of the atmosphere and antennas as a function of time.

Initial calibration of the data was provided by the ALMA observatory and completed in the CASA reduction package (McMullin et al., 2007) via the ALMA pipeline (Muders et al., 2014). We exported the provided visibilities from CASA and continued the data reduction in the AIPS reduction package (Bridle and Greisen, 1994). We self-calibrated (Cornwell and Fomalont, 1999) the data in three iterations down to a time interval of 8 seconds (possible because Europa is such a bright target), using an initial limb-darkened model and imaging more deeply in each iteration (Butler and Bastian, 1999). The initial model in each iteration is parameterized to account for limb darkening and includes the diameter (taken to be known from the observing geometry), the total flux density, and and the limb-darkening parameter, where both the flux density and the limb-darkening parameter are taken from actual fits to the visibilities at each step using the AIPS task OMFIT.

Inspection of the resulting images from the four days of observation indicated that there was an apparent offset in the overall brightness of the November 17 data compared to the other days — the November 17 data was less bright by ∼10%. Examination of the derived flux densities for J1108+0811 confirmed this offset. To determine the cause of the offset, we searched the ALMA grid calibrator monitoring catalog for flux densities derived for J1058+0133 (our flux density scale calibrator) over the period of time relevant to our observations and compared them to the flux densities used in the ALMA data reduction pipeline. We found that, while the cataloged flux densities at our frequency show the source decreasing in brightness from 3.42 ± 0.07 Jy on November 17 to 3.02 ± 0.10 Jy on November 25, this decrease was not properly reflected in the values used in the data reduction pipeline (3.37 Jy for November 17 and 3.33 Jy for November 25-27). We therefore made corrections to the flux density scale of the visibilities (and hence the brightness temperatures in the images) by accounting for the flux density differences between the measurements of J1058+0133 from November 17 and November 25 and the values used in the pipeline data reduction. The resultant correction factors are 1.015 for November 17 and 0.907 for the remaining three dates.

The final images are shown in Figure 7.1. They were produced using a robust parameter of 0, which is a good compromise between resolution and signal-to-noise. Pixel sizes are roughly a factor of 10 smaller than the actual resolution to

minimize deconvolution errors. At the time of our observations, Europa's projected diameter was $\sim 0.77''$ on the sky, resulting in $\sim$15 resolution elements across the disk. We note that this diameter is larger than the theoretical largest recoverable scale noted above. However, as the structure of the visibilities (and the sky brightness itself) is well-known for circular sources, and, as we use fits of the visibilities and an initial model incorporating the fitted zero-spacing flux density as the first step in all of our imaging, the overall brightness level is well-constrained (Butler and Bastian, 1999).

7.3 Thermal Modeling

We use a global thermal model of Europa, similar to those used for other Solar System bodies (e.g. Spencer et al., 1989; Spencer, 1990; Hayne and Aharonson, 2015), to simulate the ALMA observations. The model begins by calculating the absorbed solar flux at each point on the surface according to the local bolometric albedo. The resulting heat is then conducted through the near-surface layers, where the temperatures as a function of depth and time are controlled by the thermal inertia. The model numerically solves for these temperatures using a small global heat flux of 20 mW/m^2 (Mitri and Showman, 2005; Barr and Showman, 2009) as a lower boundary condition and grey body radiation to space as an upper boundary condition. The end result is a radiative flux map of the surface that can be output for the geometries and times of the ALMA observations, smoothed to the ALMA resolution, and converted to brightness temperature. A complete description of the model can be found in Trumbo et al. (2017).

The primary difference in our modeling approach from those taken in the past for Europa (e.g. Spencer et al., 1999; Rathbun et al., 2010) is that we do not fit for bolometric albedo, but rather use an albedo map constructed from discrete *Voyager* measurements. We take the normal albedos for distinct locations on the surface from McEwen (1986) across the green, blue, violet, and ultraviolet Voyager filters. We then weight the values in each filter by the solar flux in the corresponding wavelength range and average the values. As the phase integral of Europa is 1.01 (Grundy et al., 2007), we take these averages as approximate bolometric albedos at each location. Finally, we take these as tie-points to the greyscale *Voyager*/*Galileo* global mosaic of Europa (USGS, 2002). We fit a line to the relationship between the pixel values in the image at the Voyager albedo locations and the approximate bolometric albedo tie-points, and use this relationship to produce a high-resolution albedo map from the mosaic. The pixel values and albedo tie-points correlate with

an R^2 of 0.92 and a standard deviation in albedo of 0.03. We use the resulting map in our thermal modeling and treat the surface thermal inertia and emissivity at our ALMA wavelength as free parameters, assuming a fixed bolometric emissivity of 0.9 (Spencer, 1987).

Bolometric emissivities less than one will increase the physical temperatures of the surface by inhibiting radiative heat loss. However, as ALMA observes brightness temperatures at 233 GHz (1.3 mm), rather than physical temperatures, a decrease in emissivity at ALMA wavelengths actually tends to decrease the observed brightness temperatures everywhere on the disk for the same reason. Variations in thermal inertia, on the other hand, affect temperatures differently depending on the time of day. An increase in thermal inertia will flatten the diurnal temperature curve by reducing the contrast between nighttime and midday temperatures. In contrast, a decrease in thermal inertia will steepen the diurnal temperature curve, lowering nighttime temperatures and increasing them at midday.

When fitting the data using our simple thermal model, however, the deduced thermal inertia and emissivity may also include minor contributions from physical processes not included in the model. In particular, our model does not include sunlight penetration with depth in the regolith, thermal emission from depth in the regolith, or surface roughness. As described in Trumbo et al. (2017), our model assumes that the solar flux is absorbed in the topmost model layer, which is a standard assumption for several thermal models (e.g. Spencer et al., 1989; Spencer, 1990; Hayne and Aharonson, 2015) and particularly valid for low-albedo surfaces. However, sunlight may penetrate deeper into a relatively high-albedo particulate surface like that of Europa (Brown and Matson, 1987; Urquhart and Jakosky, 1996), resulting in heat at depth in the regolith. In practice, this effect is difficult to distinguish from that of thermal inertia (Urquhart and Jakosky, 1996), thus we include only thermal inertia in our model.

Our model also assumes that the thermal emission detected by ALMA originates in the topmost model layer. At a frequency of 233 GHz (1.3 mm), however, ALMA is likely sensing slightly deeper into the surface. Thus, modeled brightness temperatures for a fixed emissivity and thermal inertia are slightly higher than they would be if this effect were included. We find that the inclusion of sunlight absorption at depth (at an e-folding of 2 cm) and thermal emission from depth (with an e-folding of 1 cm) results in slight changes to the model thermal inertia and emissivity, respectively, but has little effect on our conclusions from the data.

Similarly, the inclusion of surface roughness appears to have little effect on our results. Surface roughness tends to increase surface temperatures, particularly at the limbs. However, using a similar implementation of surface roughness to Hayne and Aharonson (2015), we find that rms slopes up to 20° have relatively minor effects on our model fits to the data.

In our analysis, we aim to explain the nature of the large-scale thermal structure of Europa and search for any potential systematic variation of thermal properties across the surface, rather than precisely determine the true values of the individual surface thermal properties. Thus, we use our simplest model and note that our model parameters may reflect the influences of the above effects.

7.4 Fits to ALMA Observations

We begin our analysis by attempting to determine a global best-fit emissivity and thermal inertia. We simulate the four ALMA observations over a grid of thermal inertias and emissivities and find the single best-fit values to these data by minimizing the square of the residuals between model and data images. This initial fitting produces a global best-fit emissivity of 0.75 and a best-fit thermal inertia of 95 $J/(m^2 \cdot K \cdot s^{1/2})$. This thermal inertia is higher than the value of 70 $J/(m^2 \cdot K \cdot s^{1/2})$ found by Spencer et al. (1999) for the equatorial regions, but lies within the range of 30 – 140 $J/(m^2 \cdot K \cdot s^{1/2})$ mapped by Rathbun et al. (2010).

Data images are shown in Figure 7.1 alongside model images produced using these global best-fit parameters. The globally homogenous model, where only albedo varies spatially across the surface, reproduces the large-scale thermal structure of the data well. This suggests that the majority of the visible daytime thermal structure on Europa is governed primarily by local albedo variations, rather than variations in internal heating, thermal inertia, or emissivity. However, when we difference the model and data images, localized discrepancies between the data and model do become apparent. Figure 7.2 shows the residuals between each data-model image pair from Figure 7.1, where positive temperatures indicate regions where the data are hotter than the model predicts. Such discrepancies are not necessarily surprising given the inhomogeneous nature of Europa's surface, and we do not expect the entire surface, with its varying compositions and morphologies, to be well-represented by a single thermal inertia or emissivity.

In principle, discrepancies may be due to a number of possible causes. Localized differences in the thermal inertia, emissivity, or albedo from the values used in our

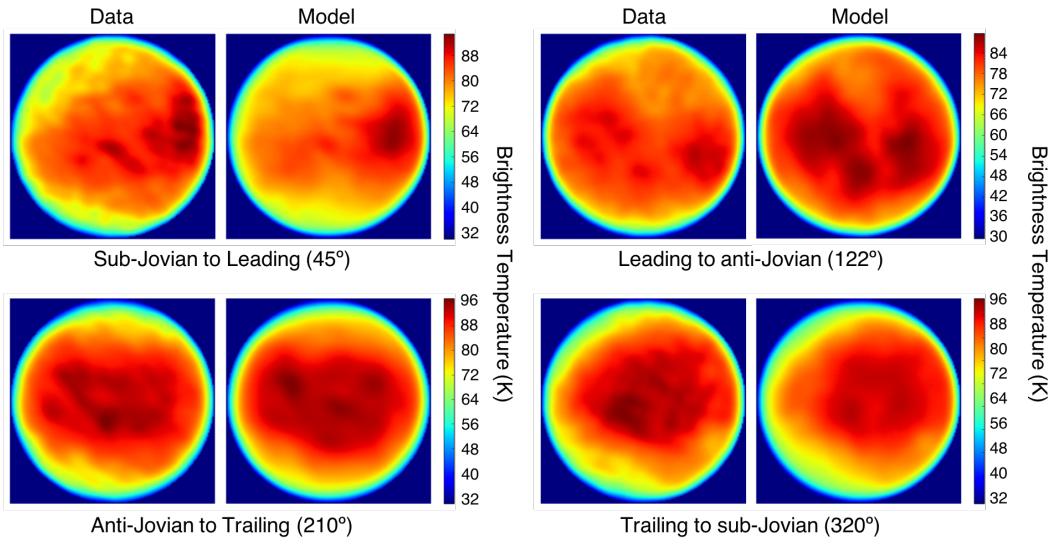

Figure 7.1: Comparison of ALMA images with model images produced using a globally homogenous thermal model and our best-fit emissivity of 0.75 and thermal inertia of 95 $J/(m^2 \cdot K \cdot s^{1/2})$. Large-scale thermal structure is well-reproduced and many corresponding features are identifiable in each data-model pair.

model will result in residuals on the spatial scale of the geographic variability in these properties. Other possible contributing factors include spatial variation in the transparency of the surface to sunlight or thermal emission, which may manifest as apparent thermal inertia or emissivity discrepancies in our modeling. As we lack observations of the same regions at multiple times of day over most of the surface, we cannot conclusively distinguish between these potential causes everywhere. For instance, most of the positive temperature anomalies in the sub-Jovian to leading hemisphere image of Figure 7.2 can be equivalently explained by a decrease in albedo of ~8–20% or an elevated subsurface heat flux of $\sim 1.2 - 2\ W/m^2$ (consistent with liquid water a few hundred meters below the surface). However, as we provide the model with spatially varying albedos derived from concrete measurements and because other objects in the Solar System exhibit significant localized differences in thermal inertia (e.g. Howett et al., 2010; Howett et al., 2011; Howett et al., 2012; Hayne et al., 2017; Putzig et al., 2005), we experiment with the idea that the residuals may be caused by thermal inertia variations.

We fix the emissivity at the global best-fit value of 0.75 and fit the data by letting the thermal inertia vary at each point. Points near the limbs of each observation are foreshortened, convolved with the cold sky, and more sensitive to surface roughness, positioning uncertainty, and other effects that are unimportant away from the limb.

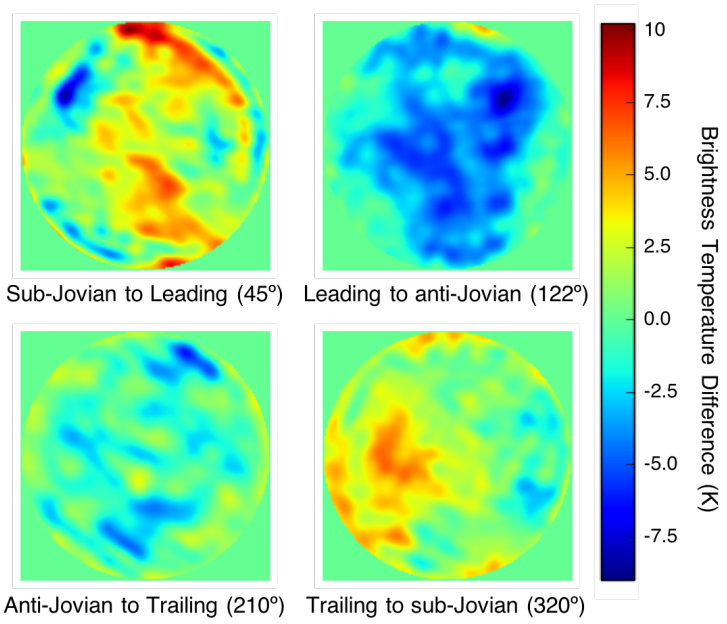

Figure 7.2: Residuals between the data and model images produced with our best-fit parameters, where positive temperatures indicate places where the data are hotter than the model predicts. Discrepancies may result from local variations in the surface thermal properties.

In addition, these locations are experiencing times of day near where diurnal curves for varying thermal inertias (at a given emissivity) intersect. The combination of this effect with the magnified uncertainties near the limbs can result in widely varying best-fit thermal inertias that are discontinuous with those of surrounding areas. Thus, we only fit data within 57° of the central point of each observation, which we find minimizes this effect without compromising our longitudinal coverage. In fitting regions that appear in two overlapping images, we use both times of day in the fitting. This produces a map of thermal inertia of the surface (Figure 7.3), assuming a globally homogenous emissivity and our bolometric albedo map constructed from *Voyager* measurements.

Under the assumption that all of the residuals between the ALMA data and the global best-fit model can be attributed to thermal inertia variations, typical thermal inertias on Europa range between 40 and 300 $J/(m^2 \cdot K \cdot s^{1/2})$, with the lowest average values on the sub-Jovian hemisphere and the highest average values between the leading and anti-Jovian hemispheres. However, it is important to note that some patterns interpreted to be thermal inertia in this map may, in reality, be due to patterns in emissivity or albedo. In fact, this method does not completely eliminate residuals

in all regions of overlap between the images, and minor discrepancies (primarily $\leq$ 3 K) remain, implying some underlying differences in emissivity or albedo from those values used.

We extrapolate our albedos from relatively few *Voyager* measurements, and this extrapolation may not work equally well for all locations on the surface. As mentioned above, the scatter between our best-fit albedo model and the measured albedo tie-points is +/-0.03, which results in adjustments to the best-fit local thermal inertia between 10–60% for most locations on the surface. However, we do not see any obvious correlation between residuals, derived thermal inertias, and albedo. Furthermore, this map does produce a locally elevated thermal inertia surrounding the crater Pwyll, which is consistent with nighttime PPR data of the same region (Spencer et al., 1999; Trumbo et al., 2017) and the tendency of crater ejecta to exhibit elevated thermal inertia elsewhere in the Solar System (e.g. Mellon et al., 2000; Hayne et al., 2017).

However, we can take a complementary approach and assume that the residuals of Figure 7.2 are instead due to variations in the surface emissivity at our ALMA wavelength of 1.3 mm. Fixing the thermal inertia at our global best-fit value of 95 $J/(m^2 \cdot K \cdot s^{1/2})$ and letting the emissivity vary at each point produces a similar map of emissivity at 1.3 mm (Figure 7.3) that alternatively fits the data with residuals of comparable magnitude in areas of overlap. Thus, the residuals of Figure 7.2 likely represent a combination of thermal inertia and emissivity variations. Indeed, we find both the fitted thermal inertia and emissivity ranges to be physically plausible. All derived thermal inertias are less than that of solid water ice, and the low end of our fitted thermal inertia range is consistent with thermal inertias derived for the Saturnian satellites (Howett et al., 2010). Similarly, the depressed millimeter emissivities we derive are consistent with those derived for Kuiper Belt and trans-Neptunian objects (Brown and Butler, 2017; Lellouch et al., 2017).

The most striking feature of both maps is the localized region of either highly elevated thermal inertia or low emissivity (deep blue in Figure 7.3) near 90° W and 23° N, which coincides with the coldest spot in both the sub-Jovian to leading hemisphere and leading to anti-Jovian hemisphere images in Figure 7.2. The fact that we see this anomaly twice in two different images and at two different times of day strongly suggests that it corresponds to a region that is truly distinct in its thermal properties. While the maps suggest that the anomaly could either be explained by an elevated thermal inertia or a low emissivity, the morning temperature measurement

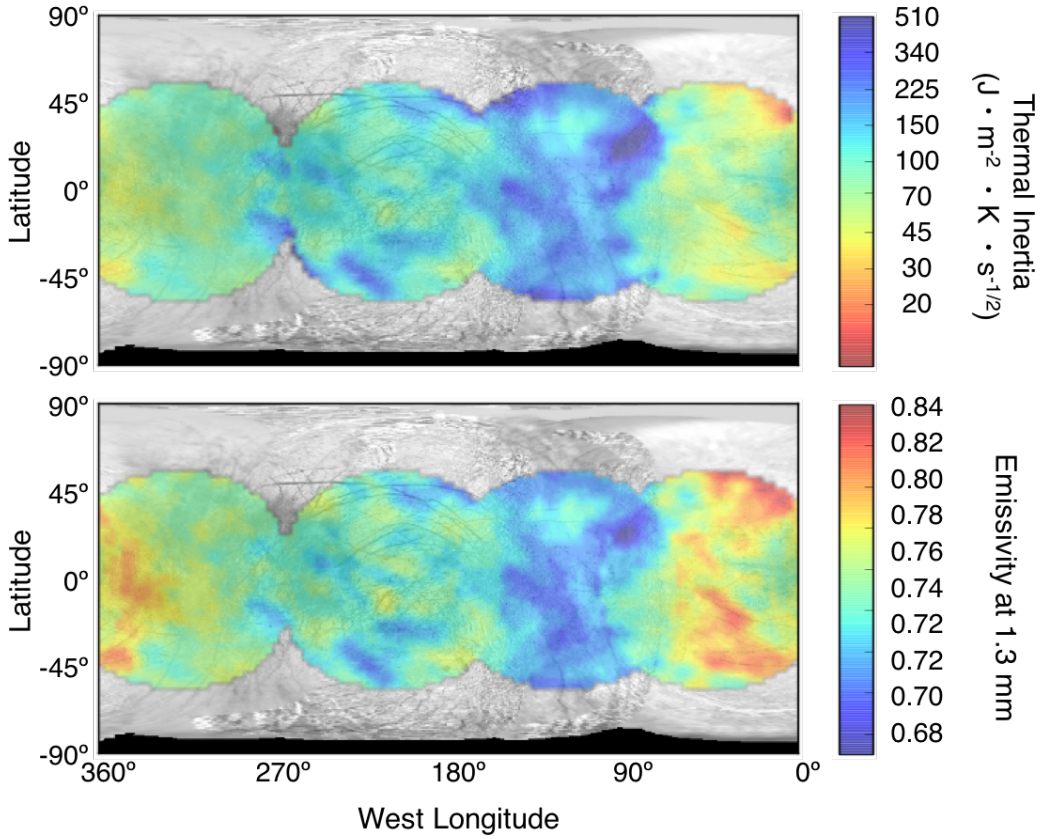

Figure 7.3: Top: Thermal inertia map created by assuming a fixed emissivity of 0.75 (our global best-fit value) and allowing thermal inertia to vary at each point across the surface. Note the elevated thermal inertia near Pwyll crater (271° W and 25° S) and the anomalously high thermal inertia at 90° W and 23° N, the location of the recurring cold spot in our ALMA data. Bottom: Millimeter emissivity map created assuming a fixed thermal inertia of 95 $J/(m^2 \cdot K \cdot s^{1/2})$ (our global best-fit value) and allowing emissivity to vary spatially across the surface. The background basemap is from USGS Map-a-Planet: https://www.mapaplanet.org/explorer/europa.html.

at this location is too cold to be fit satisfactorily by thermal inertia alone, and both measurements are best fit by a moderate thermal inertia of 80 $J/(m^2 \cdot K \cdot s^{1/2})$ and a low emissivity of 0.66. A locally high thermal inertia may indicate a region of larger average particle size or of greater transparency to sunlight. A locally depressed emissivity may also be related to particle size (and therefore subsurface scattering properties) or may indicate a compositional difference resulting in a distinct spectral emissivity or more transparent surface at the ALMA wavelength (e.g. Lellouch et al., 2016; Lellouch et al., 2017).

This region coincides with the location of highest water ice abundance mapped by Brown and Hand (2013) and the location suggested to have the most crystalline water ice by Ligier et al. (2016). However, it does not correspond to any particular geologic unit (Leonard et al., 2017) or any unusual visible morphological or albedo features (USGS, 2002). The anomaly is located within a region of relatively low-resolution imaging and was not covered by the published *Galileo* PPR data, so it is possible that a corresponding morphological, geologic, or thermal feature was simply not seen by *Galileo*. For instance, one might imagine that recent resurfacing, perhaps via melt-through or diapirism, both of which are proposed explanations for nearby Murias Chaos at 84°W and 22°N (Figueredo et al., 2002; Fagents, 2003), could have resulted in a region of recently extruded material with corresponding morphological expressions and different thermal properties than the surrounding regolith. It is also interesting to note that the anomaly is almost directly antipodal to Pwyll, the largest fresh crater on Europa at 271°W and 25°S. Antipodal focusing of impact ejecta has been suggested as a potential explanation for a high thermal inertia deposit and corresponding geologic features on the Moon that are approximately antipodal to Tycho crater (Bandfield et al., 2017; Hayne et al., 2017). However, Tycho was likely the result of a more powerful impact, and is roughly three times larger than Pwyll in diameter. Unfortunately, without new, high-resolution imaging, the potential association of this feature with unique geology will likely remain an open question.

Curiously, with the exception of Pwyll crater, our analysis has not identified any clear correlations between the potential thermal inertia values and geologic or compositional units. Although, this is not necessarily surprising, if one draws analogy to the Moon, where thermal inertia reliably follows impacts, but not major geologic units (Hayne et al., 2017). Furthermore, unlike Mimas and Tethys (Howett et al., 2011; Howett et al., 2012), and despite its location within Jupiter's magnetosphere,

Europa also appears to carry no obvious thermal inertia signature of high-energy electron bombardment. On Mimas and Tethys, the thermal inertia anomalies are associated with the leading hemisphere bombardment of electrons with energies ≥ 1 MeV (the energy needed for movement against the co-rotation direction of Saturn's magnetosphere) (Howett et al., 2011; Howett et al., 2012). It is possible that Europa lacks such a signature because the energy threshold for movement against co-rotation is much higher in Jupiter's magnetosphere (~25 MeV) (Paranicas et al., 2007; Paranicas et al., 2009), so electrons with energies > 1 MeV bombard both the leading and trailing hemispheres of Europa.

Ideally, we would include *Galileo* PPR data in this analysis. However, while our modeling approach reproduces the ALMA images quite well, it does not produce the same quality fits to the *Galileo* daytime data. When we try to incorporate the *Galileo* daytime data into our analysis, we find that the *Galileo* and ALMA data seem to prefer drastically different thermal properties, even in areas of overlap, such that the inclusion of the *Galileo* PPR data leaves residuals that appear systematic. In fact, when we attempt to model the *Galileo* PPR data alone, as we have done with the ALMA dataset, we still obtain systematic residuals, which are only eliminated if we allow albedo and thermal inertia to vary simultaneously. This approach, however, requires bolometric albedo patterns over much of the surface that show little correspondence with the *Voyager*/*Galileo* mosaic or our ALMA images. We suspect this may be the result of unexplained systematics in the PPR data, rather than real properties of Europa's surface. As we are unable to explain why the daytime PPR data is inconsistent with the ALMA daytime data in areas of overlap, we opt to forego using any PPR data and instead focus on our self-consistent ALMA dataset. Despite this, our analysis does reproduce the high thermal inertia near Pwyll crater that was derived using both ALMA data and *Galileo* PPR nighttime data (Trumbo et al., 2017; Rathbun and Spencer, 2017). If we apply the same minor albedo adjustment near Pwyll as Trumbo et al. (2017), which is within our albedo errors, we arrive at a similar thermal inertia using only the ALMA data.

7.5 Conclusions

We obtained four ALMA thermal observations of Europa, which together cover the entire surface and reveal significant thermal structure. Using a globally homogenous, one-dimensional thermal model and a bolometric albedo map constructed from *Voyager* measurements, we are able to reproduce much of this structure well, indicating that it is primarily a product of bolometric albedo variation across the

surface and the passive absorption and re-emission of sunlight. However, despite the similarity of the data and model images, there are localized disagreements, which may indicate variability in the surface thermophysical properties. We examine the possibility that these discrepancies can be explained by local thermal inertia variations and construct a corresponding thermal inertia map, assuming a globally homogenous millimeter emissivity. The map suggests typical values of the surface thermal inertia ranging from 40 to 300 $J/(m^2 \cdot K \cdot s^{1/2})$, with the lowest thermal inertias on the sub-Jovian hemisphere and the highest between the leading and anti-Jovian hemispheres. We also construct a complementary map of emissivity at our ALMA wavelength (1.3 mm), assuming a globally homogenous thermal inertia, which suggests emissivities of 0.67 – 0.84. We find little correlation of thermal properites with geology or composition and few noteworthy anomalies, with the exception of an elevated thermal inertia surrounding Pwyll crater and a region of low emissivity or extremely elevated thermal inertia near 90°W and 23°N on the leading hemisphere, in a region of relatively low-quality *Galileo* imaging. This leading hemisphere location corresponds to the region spectroscopically determined to be the iciest (and potentially most crystalline) on the surface. However, it does not coincide with any unique geologic or morphological features, nor was it it covered by the *Galileo* PPR. Thus, while we suggest that the area is distinct in its thermal properties, we can only speculate as to its origins. Future ALMA observations will provide measurements of each location on the surface at other times of day, which will allow for better constraint on the surface thermal properties and, thus, their potential influences.

References

Bandfield, J. L. et al. (2017). “Distal ejecta from lunar impacts: Extensive regions of rocky deposits.” *Icarus* 283, pp. 282–299.

Barr, A. C. and A. P. Showman (2009). “Europa”. Ed. by R. T. Pappalardo, W. B. McKinnon, and K. Khurana. Tucson, AZ: The University of Arizona Press. Chap. Heat Transfer in Europa’s Icy Shell, pp. 405–430.

Bridle, A. H. and E. W. Greisen (1994). “The NRAO AIPS project–a summary”.

Brown, M. E. and B. J. Butler (2017). “The density of mid-sized Kuiper Belt objects from ALMA thermal observations”. *The Astronomical Journal* 154.1, p. 19.

Brown, M. E. and K. P. Hand (2013). “Salts and Radiation Products on the Surface of Europa”. *The Astronomical Journal* 145.4, p. 110.

Brown, R. H. and D. L. Matson (1987). “Thermal effects of insolation propagation into the regoliths of airless bodies”. *Icarus* 72.1, pp. 84–94.

Butler, B. J. (Nov. 2012). “Flux Density Models for Solar System Bodies in CASA”. *ALMA Memo 594*.

Butler, B. J. and T. S. Bastian (1999). “Solar System Objects”. *Synthesis Imaging in Radio Astronomy II*. Ed. by G. B. Taylor, C. L. Carilli, and R. A. Perley. Vol. 180. Astronomical Society of the Pacific Conference Series, pp. 625–656.

Carlson, R. W., R. E. Johnson, and M. S. Anderson (1999). “Sulfuric Acid on Europa and the Radiolytic Sulfur Cycle”. *Science* 286.5437, pp. 97–99.

Carlson, R. W. et al. (2002). “Sulfuric Acid Production on Europa: The Radiolysis of Sulfur in Water Ice”. *Icarus* 157.2, pp. 456–463.

Collins, G. and F. Nimmo (2009). “Europa”. Ed. by R. T. Pappalardo, W. B. McKinnon, and K. Khurana. Tucson, AZ: The University of Arizona Press. Chap. Chaotic Terrain on Europa, pp. 259–282.

Cornwell, T. and E. B. Fomalont (1999). “Self-Calibration”. *Synthesis Imaging in Radio Astronomy II*. Ed. by G. B. Taylor, C. L. Carilli, and R. A. Perley. Vol. 180. Astronomical Society of the Pacific Conference Series, pp. 187–199.

Fagents, S. A. (2003). “Considerations for effusive cryovolcanism on Europa: The post-Galileo perspective”. *Journal of Geophysical Research: Planets* 108.E12.

Figueredo, P. H. et al. (2002). “Geology and origin of Europa’s "Mitten" feature (Murias Chaos)”. *Journal of Geophysical Research: Planets* 107.E5.

Fischer, P. D., M. E. Brown, and K. P. Hand (2015). “Spatially Resolved Spectroscopy of Europa: The Distinct Spectrum of Large-Scale Chaos”. *The Astronomical Journal* 150.5, p. 164.

Grundy, W. M. et al. (2007). “New Horizons mapping of Europa and Ganymede”. *Science* 318.5848, pp. 234–237.

Hayne, P. O. et al. (2017). “Global regolith thermophysical properties of the Moon from the Diviner Lunar Radiometer Experiment”. *Journal of Geophysical Research: Planets* 122.12, pp. 2371–2400.

Hayne, P. O. and O. Aharonson (2015). “Thermal stability of ice on Ceres with rough topography”. *Journal of Geophysical Research: Planets* 120.9, pp. 1567–1584.

Howett, C. J. A. et al. (2010). “Thermal inertia and bolometric Bond albedo values for Mimas, Enceladus, Tethys, Dione, Rhea and Iapetus as derived from Cassini/CIRS measurements”. *Icarus* 206.2, pp. 573–593.

Howett, C. J. A. et al. (2011). “A high-amnplitude thermal inertia anomaly of probable magnetospheric origin on Saturn’s moon Mimas”. *Icarus* 216.1, pp. 221–226.

Howett, C. J. A. et al. (2012). “PacMan returns: An electron-generated thermal anomaly on Tethys”. *Icarus* 221.2, pp. 1084–1088.

Kattenhorn, S. A. and T. Hurford (2009). “Europa”. Ed. by R. T. Pappalardo, W. B. McKinnon, and K. Khurana. Tucson, AZ: The University of Arizona Press. Chap. Tectonics of Europa, pp. 199–236.

Lellouch, E. et al. (2016). “The long-wavelength thermal emission of the Pluto-Charon system from Herschel observations. Evidence for emissivity effects”. *Astronomy and Astrophysics* 588, A2.

Lellouch, E. et al. (2017). “The thermal emission of Centaurs and trans-Neptunian objects at millimeter wavelengths from ALMA observations”. *Astronomy and Astrophysics* 608, A45.

Leonard, E. J. et al. (2017). “Updating the global geologic map or Europa”. *LPSC*. Vol. 48, p. 2357.

Ligier, N et al. (2016). “VLT/SINFONI observations of Europa: New insights into the surface composition”. *The Astronomical Journal* 151.6, p. 163.

McCord, T. B. et al. (1998). “Non-water-ice constituents in the surface material of the icy Galilean satellites from the Galileo near-infrared mapping spectrometer investigation”. *Journal of Geophysical Research: Planets* 103.E4, pp. 8603–8626.

McEwen, A. S. (1986). “Exogenic and endogenic albedo and color patterns on Europa”. *Journal of Geophysical Research: Solid Earth* 91.B8, pp. 8077–8097.

McMullin, J. P. et al. (2007). “CASA architecture and applications”. *Astronomical data analysis software and systems XVI*. Vol. 376, p. 127.

Mellon, M. T. et al. (2000). “High-resolution thermal inertia mapping from the Mars global surveyor thermal emission spectrometer”. *Icarus* 148.2, pp. 437–455.

Mitri, G. and A. P. Showman (2005). “Convective-conductive transitions and sensitivity of a convecting ice shell to perturbations in heat flux and tidal-heating rate: Implications for Europa”. *Icarus* 177.2, pp. 447–460.

Muders, D. et al. (May 2014). “The ALMA Pipeline”. *Astronomical Data Analysis Software and Systems XXIII*. Ed. by N. Manset and P. Forshay, pp. 383–386.

Paranicas, C. et al. (2007). “Europa’s near-surface radiation environment”. *Geophysical Research Letters* 34.15.

Paranicas, C. et al. (2009). “Europa”. Ed. by R. T. Pappalardo, W. B. McKinnon, and K. Khurana. Tucson, AZ: The University of Arizona Press. Chap. Europa’s Radiation Environment and its Effects on the Surface, pp. 529–544.

Pearl, J. C. and W. M. Sinton (1982). “Hot Spots of Io”. *Satellites of Jupiter*. Ed. by D. Morrison, pp. 724–755.

Prockter, L. M. and G. W. Patterson (2009). “Europa”. Ed. by R. T. Pappalardo, W. B. McKinnon, and K. Khurana. Tucson, AZ: The University of Arizona Press. Chap. Morphology and Evolution of Europa’s Ridges and Bands, pp. 237–258.

Putzig, N. E. et al. (2005). "Global thermal inertia and surface properties of Mars from the MGS mapping mission". *Icarus* 173.2, pp. 325–341.

Rathbun, J. A., N. J. Rodriguez, and J. R. Spencer (2010). "Galileo PPR Observations of Europa: Hotspot Detection Limits and Surface Thermal Properties". *Icarus* 210.2, pp. 763–769.

Rathbun, J. A. and J. R. Spencer (2017). "A closer look at Galileo thermal data from a possible plume source north of Pwyll, Europa". *AGU Fall Meeting Abstracts*.

Spencer, J. R. (1987). "Surfaces of Europa, Ganymede, and Calllisto: an investigation using Voyager IRIS thermal infrared spectra". PhD thesis. Tuscon, AZ: University of Arizona.

Spencer, J. R. (1990). "A rough-surface thermophysical model for airless planets". *Icarus* 83.1, pp. 27–38.

Spencer, J. R., L. A. Lebofsky, and M. V. Sykes (1989). "Systematic biases in radiometric diameter determination". *Icarus* 78.2, pp. 337–354.

Spencer, J. R. et al. (1990). "Discovery of hotspots on Io using disk-resolved infrared imaging". *Nature* 348.6302, pp. 618–621.

Spencer, J. R. et al. (1999). "Temperatures on Europa from Galileo photopolarimeter-radiomer: nighttime thermal anomalies". *Science* 284.5419, pp. 1514–1516.

Spencer, J. R. et al. (2006). "Cassini encounters Enceladus: Background and the discovery of a south polar hot spot". *Science* 311.5766, pp. 1401–1405.

Thompson, A. R., J. M. Moran, and G. W. Swenson (2001). *Interferometry and Synthesis in Radio Astronomy, 2nd Edition*. New York, New York: Wiley-Interscience.

Trumbo, S. K., M. E. Brown, and B. J. Butler (2017). "ALMA Thermal Observations of a Proposed Plume Source Region on Europa". *The Astronomical Journal* 154.4, p. 148. DOI: 10.3847/1538-3881/aa8769.

Urquhart, M. L. and B. M. Jakosky (1996). "Constraints on the solid-state greenhouse effect on the icy Galilean satellites". *Journal of Geophysical Research: Planets* 101.E9, pp. 21169–21176.

USGS (2002). *Controlled photomosaic map of Europa, Je 15M CMN: U.S. Geological Survey Investigations Series I-2757*. (Visited on).